This is to certify that the

thesis entitled

STUDY OF THERMAL AND FIRE BEHAVIOR OF WOOD FIBER/THERMOPLASTIC COMPOSTIE MATERIALS

presented by

ADEDEJO BUKOLA OLADIPO

has been accepted towards fulfillment
of the requirements for

PhD degree in Mechanical Engineering

Major professor

Date 18. December, 1998.

STUDY OF THERMAL AND FIRE BEHAVIOR OF WOOD FIBER/THERMOPLASTIC COMPOSITE MATERIALS

By

Adedejo Bukola Oladipo

A DISSERTATION

Submitted to
Michigan State University
in partial fulfillment of the requirements
for the degree of

DOCTOR OF PHILOSOPHY

Department of Mechanical Engineering

1998

ABSTRACT

STUDY OF THERMAL AND FIRE BEHAVIOR OF WOOD FIBER/THERMOPLASTIC COMPOSITE MATERIALS

By

Adedejo Bukola Oladipo

The fire safety characteristics of wood fiber/thermoplastic composite materials were investigated in this study. Composites comprising wood fiber fillers and polymeric binders are known to offer many advantages such as good strength to weight ratio, ease of manufacture, low cost, and the possibility for recycling. In spite of these advantages however, the fire safety question of plastic-based materials is an important one since they can, under certain conditions, drip or run, under fire, thereby potentially spreading fire from one location to the other. It is important therefore to understand the fire behavior of such a composite if the advantages it offers are to be fully utilized. To this end, numerical and experimental studies of opposed flow flame spread over the composite were conducted with emphasis on the influences of gravity, material thermal property variations, and finite-rate chemistry on the rate of spread.

The thermal properties of the composite material, needed for opposed flame spread computations, were first determined using a combination of inverse heat conduction and non-linear parameter estimation procedures. The influences of wood fiber mass fraction

and temperature on the effective thermal properties of the composite were established. The means for predicting the effective properties from those of the individual constituents were also examined and the results showed that the composite is close to being isotropic. The experimental and numerical methods used to determine the thermal properties of the composite were also adapted for the investigation of various proprietary automobile sound blanket materials to assess their effectiveness as thermal barriers separating the engine compartment from the passenger cabin.

The results of opposed flame spread study over the composite suggests that, for opposed flow velocities lower than about 245 cm/s, finite rate chemistry will dominate the spread process when the oxygen mass fraction is 70% or less. Above this limit, heat transfer from the flame to the unburned fuel ahead seems to be the dominant factor. Also, the composite was observed to exhibit wood-like fire behavior when the wood fiber mass fraction is 40% or more.

To the memory of my father, Oladesu Oladipo,
and my dearest friend, Gbenga Faloba.

ACKNOWLEDGMENTS

I wish to express my profound gratitude to my advisor, Dr. Indrek Wichman, for his guidance and support in the course of this work. He not only provided quality advising at every stage of the project but also demonstrated a genuine concern in my professional development and welfare. His efforts at securing funds to provide me with adequate research assistantship throughout my doctoral study as well as sponsorship to professional meetings are highly appreciated.

I also want to thank Dr. James Beck, Dr. Craig Somerton, and Dr. Susan Selke for serving on my dissertation committee and for providing useful advice from time to time. I gained a lot from Dr. Beck's ever inquisitive comments and from his mastery of the art of conducting quality experimental studies.

Special thanks go to the organizations that supported this work. They include the United States Department of Agriculture, General Motors Corporation, and Michigan State University (under the All University Research Initiative Grant program).

The greatest contributors to my success in life are, of course, the members of my family. My mother, Mobolaji Oladipo, who has sacrificed so much to ensure that all her children succeed in life to the best of their God-given ability; my brother, Dr. Wale Oladipo, for being the pillar all by himself for the entire family; and my other siblings. My special gratitude to my wife, Toyin Oladipo, for her unwavering support and love that enable me to put in my best in everything I do. My gratitude also to my daughters, Titi and Seun, who are my *precious jewels* and my greatest source of joy each and everyday.

There are several other individuals who contributed in one way or the other to make this work a success. Patrick Gayle helped to generate an AutoCad drawing of the flame spread experimental set-up while Brian Makie, Lisa Oravecz, Heidi Westlake, and Dr. Anjan Ray (now of IIT Delhi, India) all provided helpful suggestions and assistance at various times. I will also like to thank Roy Bailiff, for his numerous technical assistance, and Gloria Elliot, for her interest and questions during my presentation which made my dissertation defense very lively. Nancy Chism is also remembered for her numerous administrative assistance and for her friendly disposition as the graduate secretary.

Above all, I give all Glory and Honor to God Almighty for His mercy and grace over me and for confirming, once again, that those who trust in Him shall not be in want.

TABLE OF CONTENTS

LIST OF TABLES

LIST OF FIGURES

NOMENCLATURE

A	Pre-exponential factor for gasification process
C	Heat capacity (J/kg K)
D	Damköhler number
E	Activation energy for gasification process
g	Gravity (m/s^2)
h	Convective heat transfer coefficient (W/m^2 K)
L	Thickness (cm)
m	Solid gasification mass flux
p	Pressure (N/m^2) or material property (designation stated in text)
Pe	Peclet number
q	Heat flux (W/m^2)
R	Universal gas constant (J/kmol K)
t	Time (s)
t^+	Dimensionless time
T	Temperature (°C)
T_i	Theoretical value of temperature at time t_i (°C)
u	Velocity (cm/s)
V	Volume fraction of wood fiber in the composite
Y_i	Value of measured temperature at time t_i (°C)
Y_O	Oxygen mass fraction

Greek

α	$\alpha = \lambda/\rho C$, thermal diffusivity (m^2/s)
β	$\beta = E/RT$, dimensionless activation energy
ϕ	Fraction of wood fiber (on mass basis) in the composite
φ	$\varphi = \lambda\rho C$, thermal responsivity (J^2/m^4K^2s)
κ	Multiplicative flame spread factor (dimensionless)
λ	Thermal conductivity (W/m K)
θ	Sample inclination angle (degrees)
ρ	Density (kg/m^3)

Subscripts

c	Composite designation (except as otherwise stated in text)
ch	Pertaining to finite rate chemistry
d	Pertaining to dissociation
f	Flame condition or fiber designation (as stated in text)
g	Gas phase
m	Matrix designation
p	Pertaining to constant pressure
s	Solid phase
x	Axial direction
y	Vertical direction

v	Solid gasification condition
∞	Ambient condition (exception: κ_∞ represents the case of heat transfer model)

CHAPTER 1

INTRODUCTION

1.1 General

The purpose of this study is to investigate thermal and fire behavior of plastic-based composite materials with a view to understand their fire safety characteristics. The ultimate objective is to correlate such characteristics with the composition of the composite and with the physical and chemical environmental conditions in which fire over the materials may occur.

1.2 Background

Composite materials comprising wood fibers and thermoplastic binders have great potentials for industrial and domestic applications. They are known to offer advantages such as good strength to weight ratio, ease of manufacture, low cost, and the possibility for recycling [1,2]. Such composites are presently used for exterior construction purposes, industrial flooring, and even in automobiles where they are used as substrates for interior door panels, roof headliners, and other components [3].

In the work of Selke [2] and Pattanakul et al. [4], it was shown that the mechanical properties of recycled high density polyethylene (HDPE), obtained from ground and processed post-consumer milk bottles, are not significantly different from those obtained from "virgin", newly-manufactured pellets. For wood fiber/HDPE composites therefore, it does not matter, from the point of view of mechanical properties, whether the HDPE is

a recycled one or fresh from the manufacturing plant. This is an added advantage because two potentially "waste streams" of wood and HDPE can be utilized to make the new material, since the wood fibers can be products of mechanical or chemical pulping of leftovers from wood lumber processing themselves.

In spite of these advantages however, the fire safety question of plastic-based materials is an important one. Under certain conditions, the composites can ignite and burn thereby compromising the structural integrity of a part and potentially spread fire from one location to the other. Furthermore, the question must be asked as to which of the constituents' thermal behavior does the composite material most resemble. Is it that of the thermoplastic binder, which can drip or run or that of wood which does not melt under fire and hence does not lose its mechanical strength? At what composition does the transition from plastic-like to wood-like behavior occur? What component composition produces properties that are indicative of best thermal and fire safety characteristics?

While research efforts are continually directed at developing new plastic-based composites to satisfy various needs, unfortunately their fire-safety properties are not as easily determined as are their strength properties, such as torsion, stiffness, etc. The need to establish such thermal and fire properties becomes even more significant when it is recalled that the temperature of a material, dictated by its response to heat flux inputs, can dramatically alter its mechanical properties.

1.3 Scope of Study

To satisfy research needs identified above, the burning characteristics of composite materials, comprising aspen wood fibers and high density polyethylene (HDPE) matrix,

were established through studies of flame spread over the materials. The studies were conducted under conditions of buoyancy-induced opposed flow with emphasis on the influences of finite rate chemistry, gravity, and material property variations on the rate of spread. Detailed considerations were also given to such scientific factors as thermal decomposition and ignition of the solid material.

A review of the relevant existing literature is presented in chapter 2 with particular emphasis on flame spread research.

It is obvious that thermal and fire behavior of the composite will be dictated, to a very large extent, by its thermal properties. Evidence of this fact is given by the prominent appearance of the thermal property ratio in flame spread rate formulas over solid fuels. For instance, DeRis [5] showed that the rate of flame spread over thermally thick and thermally thin fuels are respectively given by Equations 1.1 and 1.2 below:

$$u_f = u_g \frac{\lambda_{gy}\rho_g C_{pg}}{\lambda_{sy}\rho_s C_s}\left[\frac{T_f - T_v}{T_v - T_\infty}\right]^2 \tag{1.1}$$

$$u_f = \sqrt{2}\,\frac{\alpha_s}{L_s}\,\frac{\lambda_s}{\lambda_g}\left(\frac{\lambda_g\rho_g C_{pg}}{\lambda_s\rho_s C_s}\right)^{1/2}\left[\frac{T_f - T_v}{T_v - T_\infty}\right] \tag{1.2}$$

These equations reveal the dependence of the flame spread rate, u_f, on the ratio of thermal responsivity ($\lambda\rho C$) between the gas and the solid. The direction y is perpendicular to that of flame spread while T_f, T_v, and T_∞ represent the temperature of the flame, the gasifying solid, and the ambient, respectively. It can be seen from these relations that accurate knowledge of the thermal conductivity, λ, and the volumetric heat

capacity, ρC, of the solid material and their variations, if any, with temperature is needed before a thorough analysis and correlation of flame spread over the material can be undertaken. For this reason, the determination of these properties for the composite materials and the correlation of same with compositions and temperature are considered as a prelude to the flame spread studies and are reported in chapter 3. The experimental and numerical procedures employed for this purpose involve the consideration of layers of different materials placed face-to-face to form a layered block and the analysis of the thermal response (to heat flux) of each layer in turn.

Owing to the similarity in physical configurations and heat flow pattern, the same procedures of chapter 3 are adapted and used for establishing similar properties for some layered automobile bulkhead fire barrier materials in chapter 4. These property results are then used to predict the role of each layer forming the barrier in the prevention of post-crash fire spread from the engine compartment to the passenger cabin. This aspect of the study is done to assert the reliability of the procedures and also to satisfy a research commitment to a funding client (General Motors Corporation).

With the relevant thermal properties and their variations with temperature and composite composition established, experimental study and modeling of opposed flow flame spread over the composite materials follow in chapter 5. Models are developed to account for the influences of gravity, finite rate chemistry, and solid thermal property variations on the rate of flame spread.

The conclusions from this study and some recommendations for future research are listed in chapter 6. In Appendix A that follows, the possible decomposition mechanisms

for the composite material are examined using cellulose as a representative material. Three different kinetic schemes are considered from which conclusions about the nature of the gasification temperature are made.

In attempting to understand the behavior of wood fiber/HDPE composites, one other factor that must be considered is wood hygroscopicity through which it loses or gains moisture, even when in use, depending on the local environmental conditions. This can significantly influence the mechanical and thermal properties of the wood and hence those of the resulting wood-polymer composites. Also, to ensure that the results of this study will be readily applicable, or easily adapted, to various wood fiber-polymer composites, it is necessary to establish any dependence of the properties on wood-type.

Wood species are generally classified into two groups, hardwoods and softwoods. Although moisture variation affects the properties of different wood species within the same group roughly in the same manner, the effects on species of opposing groups are significantly different [6]. An important wood property relevant for studying these effects is the fiber saturation point, which corresponds to approximately 30% moisture content for softwoods and about 20% for hardwoods [7].

To establish the influences of moisture absorption and desorption in detail, therefore, the mechanical properties of the wood fiber-HDPE composites, with the fibers specially moistened to various degrees prior to composite manufacture, are studied in Appendix B. The variation with wood-type is established by examining composite materials that are based on aspen and pine wood fibers, representing hardwood and softwood, respectively.

CHAPTER 2

LITERATURE SURVEY

2.1 General

A review of the existing literature on the research problem, with emphasis on the flame spread aspect, is presented in this chapter. Although some of the other aspects are major research areas by themselves, for which a substantial body of literature materials exists, only the minimum review, as is necessary to enhance understanding of the discussion in these *auxiliary* areas, can be presented in order to keep the dissertation brief and concise.

2.2 Wood Fiber/Thermoplastic Composites

In attempts to make wood fiber/recycled HDPE composites more attractive for use in various applications, many studies have been conducted to develop means for improving their mechanical properties and for establishing health hazards associated with their manufacture. Since wood fiber is polar and hydrophilic while HDPE is non-polar and hydrophobic, the quality of the interfacial adhesion between the two is always questionable [8]. Poor bonding will have adverse affects on the mechanical properties of the resulting composite. Also, recycled milk bottles are known to sometimes give off unbearable noxious odors when heated during processing. There is the possibility that these odors come from burning milk residues or from the release of rancid odors absorbed by the plastic itself. It was suggested in [9] that the major chemical component in these odors is butyric acid, resulting from lipolysis of milk fat. The relevant question then is,

"to what extent will the presence of the acid in the HDPE milk bottles influence the mechanical properties of the resulting wood/HDPE composites?"

Selke et al. [8] conducted studies in which some additives were added to recycled HDPE matrix (from milk bottles) in order to examine their effectiveness in improving the interfacial bonding. They examined five different additives and found that maleic anhydride modified polypropylene and ionomer modified polyethylene had potential as suitable additives to the HDPE matrix. They reported that significant enhancement in the tensile properties of the composites was obtained with both additives.

Haraguchi [10] later examined the effectiveness of surface sulfonation of the HDPE matrix as a means of enhancing the mechanical properties of aspen wood fiber/HDPE composite materials. He reported that sulfonation produced no significant improvement in the mechanical properties of the composite. However, he observed that the addition of maleic anhydride modified polypropylene as a coupling agent significantly increased the tensile properties in agreement with the findings in reference 8.

On the subject of odor absorption in the plastic, Hernandez et al. [11] conducted experimental studies to measure the retention rate of butyric acid in post-consumer milk bottles and the associated effects on the mechanical properties of the plastic. Their results showed that the HDPE can retain as much butyric acid as 3.2% of its own weight. They also found that the retention does not have a significant impact on the tensile strength of the plastic, but does affect the impact strength and the elongation data. They concluded that even though the level of butyric acid in the recycled HDPE milk bottles may not be detrimental to its physical properties, odors caused by the milk residues may be a

problem. They thus advised that, for recycling purposes, contamination should be avoided by rinsing milk residuals off the container as soon as possible.

2.3 Flame Spread over Solid Fuels

Earlier systematic studies of flame and fire spread originated along two initially separate lines of research interests. The first focused on the small-scale flame spread problem over propellants while the second involved studies of large-scale fire spread. To understand the proper meaning of the term *flame spread*, it should be noted that burning of a solid material can be classified into two general cases, normal burning which is perpendicular to the surface and tangential burning or spread along the surface. If the former is small compared to the latter, we have a *flame spread problem* for which the normal burning calculation will be of lesser significance than the spread calculation [12]. The simplest form of flame spread is the case where the assumption of a non-regressing surface applies. Under such condition, the pyrolyzing surface contributes only a mass flux of volatiles to the gas. Thus, there are no complications such as flow separation at the regression front or blowoff of surface chaff, etc. This is the kind of flame spread that is considered in this study.

Flame spread can be further sub-divided into two major groups, namely opposed flow flame spread and wind aided flame spread. In the opposed flow type, which is the subject of this dissertation, the flow of the oxidizer gas is in the direction opposite to that of flame spread over the solid fuel. In contrast, the flame spreads in the direction of the oxidizer flow in the wind aided type.

Considerable attention have been focused on the opposed flow flame spread problem in the literature. Most of the early work in the field is discussed in the review article by Friedman [13]. In the article, the rate of flame spread was shown to depend on many factors including sample angle of inclination, material composition, gas-phase pressure and oxygen concentration, and dilution of the gas flow by inerts. The distinction between thick and thin fuels was also recognized with experimental results on both types presented and discussed. However, no explicit distinction between opposed flow and wind aided flame spread was made even though experimental results that typify both were presented. The article also included suggested physical processes which its author believed should be given priority in modeling efforts. These were identified as leading edge flame aerodynamics, the diffusion processes, and fuel volatilization chemistry.

Contrary to these suggestions, the theoretical study by Tarifa and Torralbo [14] focused on the detailed heat-transfer processes in the burning solid. The gas phase was treated as merely providing boundary condition for the solid-phase problem. The authors further assumed that the *vertical* gas-phase flame provides an exponential heat flux onto the fuel ahead of it and a polynomial heat flux onto the pyrolyzing region behind it. By solving the two-dimensional solid-phase conduction equation, using the assumption of an exponentially decreasing temperature in the direction perpendicular to that of flame spread, they were able to develop a formula for the spread rate by calculating the rate of fuel heat-up to the *ignition temperature*, T_v. Although, their approach yielded some physically plausible results for flame spread over liquid fuel, it has not yet proved to be the most fruitful method for flame spread research.

Next came the doctoral thesis work of deRis [15] which employs a combination of sound physical reasoning and rigorous theory to develop basic understanding of the flame spread mechanism. Employing the Oseen flow approximation, deRis analytically solved two-dimensional conservation equations by neglecting gravitational effects, thus avoiding buoyancy complications, and by postulating a vaporizing solid at a constant temperature T_v. This enables him to ignore complex melting and pyrolyzing processes as well. He correctly poses the flame structure near the leading edge for the first time but was able to neglect the ensuing triple-flame by assuming that gas-phase ignition temperature is lower than the vaporization temperature. His work leads to analytical expressions for the rate of flame spread over thick and thin fuels as given in Equations 1.1 and 1.2 of chapter 1.

The experimental work of McAlevy and Magee [16] appeared at about the same time as deRis' work. These workers approached the flame spread problem from the propellant side, taking a considerably more physical point of view than deRis. They (erroneously) postulated that flame spread is an intrinsic combustion quantity, not realizing that the rate of spread depends on flow velocity. They also did not recognize the fact that the spread rate depends on sample thickness, having examined samples that were 7.62 cm (length) by 0.95 cm (width) by 0.32 cm (thickness) in dimensions. The thickness (0.32 cm) is small compared to the critical value (which will be shown later in chapter 5 to be about 0.58 cm) above which the samples can be considered thermally thick. Unfortunately, it cannot be taken as thermally thin either.

McAlevy and Magee postulated a flame spread rate formula given by the ratio of the heat-up distance ahead of the flame to the ignition time. By assuming power law

dependencies for both terms, they came up with the expression $u_f \propto \left(pY_O^{\,a}\right)^b$, showing the dependence of the spread rate on pressure, p and oxygen mass fraction, Y_O. They then obtained values for the constants a and b by fitting correlation curves through their experimental data for various materials.

Several researchers questioned the adequacy and reliability of deRis' flame spread theory due to the form of his analytical expressions for flame spread rates (Equations 1.1 and 1.2). One reservation that some workers had concerning his work is the fact that his flame spread expression for thick fuels implies that the spread rate, u_f rises continuously with opposed flow velocity, u_g and will be zero if there is no forced flow. This was viewed as being contradictory to some laboratory results which have shown that flame spread over thick fuels can occur in an environment of quiescent air. Later in his review article, Wichman [12] explained that even if the oxidizer was initially quiescent the hot flame zone would induce an opposed flow (under normal gravity) due to buoyancy forces so that u_g will be non-zero. Also, the fact that deRis' thick fuel flame-spread formula predicts that u_f is independent of the solid-phase conductivity in the direction of spread was considered to be a sore point.

As a result of these reservations, several studies appeared which were directed at establishing the precise mechanisms for flame spread as well as the influences of various factors on which the rate of spread was thought to depend. The interests led to more systematic studies concerning the influences of the opposed flow field, gravity, solid-phase thermal property variation, and finite rate chemistry on the rate of spread.

Among such studies are the work by Sirignano [17,18]. As stated in his initial review [17], Sirignano considered deRis work to be "afflicted" by two negative factors namely the independence of u_f on stream-wise conductivity and the use of constant vaporization temperature. He was of the opinion that the T_v hypothesis was faulty although Wichman and Williams [19] later justified it in their re-examination of the flame spread problem. Sirignano contended that T_v will depend on the specific heats, kinetic constants, temperature, and some other variables and that it will be difficult to measure. He instead assumed a surface gasification process: $\dot{m} = AY_O \exp[-E / R(T - T_\infty)]$ where A is the pre-exponential factor and E is the activation energy. He then eliminated gas-phase chemical reactions altogether and proposed the above oxidation mechanism as a means for heat generation by a surface flame.

While some of his assertions are valid, Sirignano's computed results however, produced flames that were unusually short and did not resemble those of many workers including the laboratory flames of McAlevy et al. and those of deRis [15,16,20,21]. This was probably due to the improper form of the oxidation formula used in his study. In reference 7, it was suggested that it would have been more reasonable to have $\dot{m} \propto (\partial Y_O / \partial y)$ instead of $\dot{m} \propto Y_O$. It was pointed out that in the latter case, there would be no mass flux to the surface and hence no surface heat generation when $Y_O = 0$ even though the diffusive flux of oxidizer toward the surface may be enormous.

Some of the other theoretical works of this time include the study by Ohki and Tsuge [22] and that of Fernandez-Pello and Williams [23,24]. The latter sought to develop flame spread theory that include detail consideration of the gas-phase chemistry

and the solid fuel degradation premised on the insights gained from earlier experiments by Fernandez-Pello [23]. They based most of their hypothesis and assumptions on the results of those experiments. Unfortunately, the experimental results were in turn called into question later by subsequent theories and other experimental findings. For a detailed discussion of their model and several others developed afterwards, the interested reader may consult reference 7.

2.3.1 Influences of Material Property Variation

Many studies have been directed towards establishing the influences of material thermal property variations on the flame spread rate. As can be seen in deRis flame spread formulas, [5], the influences of the thermal properties of the solid appears through ratio of thermal responsivity ($\lambda_g \rho_g C_{p_g} / \lambda_s \rho_s C_s$) between the gas and the solid. Partly owing to the interest in understanding which components (transverse or streamwise) of these thermal properties are important, attempts have been made by many workers to determine the medium (gas-phase or solid-phase) through which heat transfer from the flame to the unburnt solid material ahead occurs.

In the work of Fernandez-Pello and Williams [24], the bulk of the heat transfer ahead of the flame front was considered to occur through the solid phase. Correctly recognizing that this hypothesis will be true only when the solid-to-gas Peclet number ratio is small ($Pe_s / Pe_g << 1$), the authors also backed this assertion up with earlier experimental results [23]. Wichman et al. [25] later suggested that the Peclet number ratio condition may be valid only in cases involving low oxygen mass fraction in the oxidizer

gas. Further experimental evidence contradicting the small Peclet number ratio hypothesis was provided by Ito and Kashiwagi [26] who suggested that even for air the solid phase does not dominate the upstream heat transfer from the flame.

Among the studies that were directed at establishing the dependence of the flame spread rate on the solid thermal conductivity is the study by Feng and Sirignano [27]. Their results showed that the spread rate decreases as solid thermal conductivity in the direction of spread increases, a direct opposite to their original intuition. Based on these results, the authors reasoned that most of the heat transfer ahead of the reaction zone must be occurring via heat conduction in the gas.

In the analytical work of Wichman and Williams [19,28], the thermal conductivities of the solid were directionally "tagged." The streamwise conductivity vanished from the flame spread formula leading to the somewhat surprising result $u_f \propto 1/\lambda_{sy}$, where y indicates the transverse direction (perpendicular to direction of flame spread). This result implies that only the transverse conductivity could alter the rate of flame spread.

Crescitelli et al. [29] conducted experimental studies to examine the influence of λ_s on u_f. Their method involved the mixing of metallic powder into polystyrene samples to increase λ_s while leaving T_v essentially unchanged. Their qualitative results sparked the interests in flame spread study over composite materials. Later, Di Blasi and Wichman [30] conducted a numerical study which showed that only the transverse component of λ_s had a significant effect on the rate of flame spread. A thousand fold increase in the longitudinal component (in the direction of spread) was shown to have essentially no

influence on u_f. These results confirmed the earlier *seemingly anomalous* predictions of Wichman and Williams [19,28].

For wood fiber/polymer composites, it is necessary to examine the influences of thermal responsivity ($\lambda\rho C$) as a variable, since differences in thermal properties [31] and decomposition pattern of the fiber filler and the polymer matrix can affect flame spread in significantly different ways. In the work of Zhang et al. [32], the effect of melting behavior of various thermoplastic materials on upward flame spread was studied using large-scale tests. They reported that, for some materials, melt pools, formed at the base of vertically oriented test samples, created pools of fire which in turn controls the growth of the fire and flame spread. For materials having higher glass transition temperatures however, no significant melting was observed, the materials remaining in the solid phase while undergoing gasification. The article noted that flame spread characteristics for these latter group of fuels were quite different from those of the former. As explained in chapter 1, wood belongs to the class of materials which does not melt when burning unlike the polyethylene matrix which can melt, drip or run under certain conditions.

2.3.2 Influences of Opposed Flow Field and Gravity

Many investigations have been conducted to examine the influences of the opposed flow velocity and gravity on the rate of flame spread [33-35]. As seen in Equation 1.1, the thick fuel flame spread formula of deRis produced $u_f \propto u_g$, indicating a monotonic rise of flame spread rate with opposed flow velocity. Experimental findings reported later showed that the dependence of u_f on u_g is more complex than this [20,36].

Lastrina et al. [20] conducted experiments in a forced opposed flow *blow-down* wind tunnel inside which they measured flame spread rates over polymethylmethacrylate (PMMA) over a wide range of opposed flow velocities and at different levels of opposed flow oxygen concentrations. They found that u_f increased with rise of u_g up to a certain critical value and decreased when u_g was increased beyond this value. From their data, they produced a correlation which showed that $u_f \propto u_g^{0.34} Y_O^2$ in the region of increasing flame spread rate. The results of the study by Ray [36] confirm the same qualitative trend.

For downward flame spread, part (or all) of the opposed flow is buoyancy-induced. If the opposed flow is fully buoyancy-induced, the opposed velocity (u_g) is a function of the streamwise gravity (g_x) which in turn depends on the angle of inclination of the test sample. Theoretically, $u_g \sim [\alpha_g g_x (T_c - T_\infty)/T_\infty]^{1/3}$ where $g_x = g\cos\theta$, θ is the angle of inclination as measured from the vertical direction, α_g is the thermal diffusivity of the gas, and T_c is a characteristic wall temperature based on the conditions of the flame such as oxygen mass fraction, dissociation, etc. A value of 1.3 was suggested as the constant of the proportionality in the work of deRis [5].

Since the flame spread formula for thick fuel implies that $u_f \sim u_g$, many studies have been conducted in which u_f is correlated with g_x in order to establish the influence of gravity on the spread rate [37-40]. Wichman and Saito [37] conducted experiments in which flame spread rates over thermally thick PMMA samples were measured for θ=0°, 7°, and 15°. The plot of their data showed that the dependence of u_f on g_x is stronger that the theoretical prediction of 1/3. It is possible that this result indicates influences of

other factors, other than u_g variation with inclination angle, that were not recognized earlier. This possibility is explored further in chapter 5.

In the study by Chen and Yang [38], the effect of inclination angle on flame spread over thermally thin solid fuels was investigated. The authors conducted a full numerical simulation of the problem for angles of inclination ranging from 0° to 40°. They presented results that showed that the flame spread rate was minimum at 0°, the vertical position, and increased with θ thereafter. In their configuration, the angle of inclination was measured from the horizontal so that the range of angles covered in their study is 50° to 90°, with 90° corresponding to the vertical direction. They compared their results with experimental findings of other workers [39,40] and reported good qualitative agreement.

2.3.3 Influences of Finite Rate Chemistry

The flame spread formulas derived by deRis were based on the analysis of heat transfer from the spreading flame to the unburnt material ahead, the chemistry rate considered infinite. As mentioned earlier, experimental studies by Lastrina [20] and by Ray [36] showed that u_f only increases with u_g up to a certain limit and decreases if u_g is increased further. It has been suggested that this decline in u_f is due to the influences of finite rate chemistry which dominates the spread process beyond some critical levels of opposed flow velocity [36]. Ray [36] identified two distinct regions from the u_f - u_g plot for any given value of oxygen mass fraction Y_O. The first is represented by $du_f / du_g > 0$ and corresponds to the range of u_g where the dominant physical mechanism for flame

spread is heat transfer from the flame to the solid. For the other, $du_f / du_g < 0$ and finite rate chemistry dominates the spread process in this region.

Several articles addressing the issue of finite rate chemistry effects on flame spread have been published. Frey and T'ien [41] numerically studied flame spread over thin fuels with finite rate chemistry considerations included in the simulation. They found out that there is indeed quenching of the flame at the tip and confirmed that chemistry factors must be included in order to accurately represent the physical process in this zone. Their results also confirmed that the constant gasification temperature hypothesis is good when pyrolysis zone is larger than few thermal lengths which is true in most cases.

In the analytical work of Wichman [42], the physical and chemical conditions at the flame tip were subjected to a thorough investigation in order to establish the influences of finite rate chemistry on the spread rate. The author assumed that a small semicircular premixed flame arc *anchors* the trailing diffusion flame as it propagates into a small locally uniform mixture of fuel and oxidizer sustained by the strength of mass diffusion near the fuel surface. Although this assumption was later pointed out to be incorrect [12], the article nevertheless contains insights and useful formulas that significantly advance the details of the underlying physics governing chemistry-dominated flame spread.

There are a few published articles in which the finite rate chemistry problem was addressed more from a graphical point of view. For instance, the studies reported in [36,43,44] all included correlations of the finite rate chemistry factor, κ (defined as the ratio of the experimental value of u_f to the theoretical value calculated using Equation 1.1) with Damköhler number, D based on experimental data. The exception is

the work by Rybanin [45] which involves analytical derivations and produces a mathematical expression for $\kappa(D)$.

While these correlations are elegant and provide graphical insights into the physics of the problem, they are in fact cumbersome to use. Accurate knowledge or close approximations of the composite chemical properties are needed to compute D. It seems better to adopt the approach where various experimental data are used to separately *extract* the contributions of gravity, material property, and finite rate chemistry in a sequential manner. This is the approach that is taken in this study.

CHAPTER 3

INVESTIGATION OF THERMAL PROPERTIES

3.1 General

As seen in chapter 1, the ratio of thermal properties of the gas and the solid feature prominently in flame spread formulas. For the wood fiber/HDPE composite therefore, accurate knowledge of these properties is required for effective modeling of flame spread over the composite. To this end, the effects of fiber mass fraction and temperature on the effective thermal properties of the composites are investigated in this chapter. The measured properties and their correlation with composite composition and temperature will provide basis for the thermal property data needed for opposed flow flame spread modeling of chapter 5.

3.2 Theoretical Background

There are two ways in which unknown physical properties of any composite material can be determined. The first is to conduct experiments in which the properties of interest are determined directly. Depending on the quality of the experimental procedure, this method may yield the best results. However, this option can be expensive and time-consuming. The other option is to calculate the desired properties using theoretical expressions or correlation formulas and known values of the properties for the individual components making up the composite. This second option is more desirable since, for any given

composite composition, sufficiently accurate estimates of the desired properties can be calculated in a timely manner.

There are several theoretically-derived functions in the literature that relate the thermal properties of a composite material to those of its individual components. Most of these functions are based on composite materials consisting of two material components, the fiber fillers and the polymeric binders. The simplest function, used often to at least obtain an initial guess of the property p of a given composite, is the rule of mixtures

$$p_c = p_f V_f + p_m V_m \tag{3.1}$$

with subscripts c, f, and m referring to the composite, fiber and matrix, respectively, and V representing the volume fraction.

Among the more complicated predictive formulas are those based on the Eshelby's method [46] in which the fibers are treated as inclusions. Two models that can be used to derive the effective thermal properties of the composite following this method are the spherical inclusion model and the cylindrical inclusion model. As the names suggest, the fibers are considered as spherical particles in the former model whereas they are treated as cylinders in the latter. The expression for the thermal conductivity using the spherical inclusion model is [46]

$$\lambda_c = \lambda_m \left[1 + \frac{V_f}{(1-V_f)/3 + \lambda_m/(\lambda_f - \lambda_m)} \right]. \tag{3.2}$$

With the cylindrical model, the thermal conductivity in the longitudinal direction is given by Equation 3.1, with p replaced by λ, and in the transverse direction by [46]:

$$\lambda_c = \lambda_m \left[1 - \frac{V_f}{(1-V_f)/2 - \lambda_m/(\lambda_f - \lambda_m)} \right]. \tag{3.3}$$

In the work of Ziebland [47], Equation 3.1, the simple rule of mixtures, was also given as the expression for the thermal conductivity in the longitudinal direction while the crosswise component was given by

$$\lambda_c = \frac{\lambda_m \lambda_f}{\lambda_m V_f + \lambda_f V_m}. \tag{3.4}$$

Literature search at the time of this study did not yield any simple, equivalent closed-form expressions for predicting the overall specific heat of the composite. Usually, the simple rule of mixtures is used.

3.3 Composite Manufacture

Since this is the first time the composite material will be discussed in great detail, it is helpful to first describe the processes through which it is manufactured. It is likely that such a description will aid the understanding of the inner structure of the composite materials and the background behind some of the property trends that are observed.

The two components from which the composite is formed are aspen wood fibers and PAXON™ AD60-007 HDPE pellets. These components are fed at pre-determined mass flow rates, based on the desired wood fiber mass fraction in the composite, into a ZSK 30 Werner & Pfleiderer extruder having 28 mm co-rotating twin screws. The extruder is operated at a working temperature of 150 °C and a screw rpm of 100. This

™ Registered Trademark of PAXON Polymer Company

temperature ensures that while the polymer is fully melted (melting point is 120-135 °C) the wood fibers are not burned. Owing to the fluffy nature of the wood fibers, the components are fed into the extruder through separate ports to ensure uniform fiber distribution within the composite. Because of the hygroscopicity of the wood fibers, the K-TRON SODER feeder used to feed the wood fibers is calibrated each time it is used to ensure that the desired wood fiber mass fraction in the composite is accurately attained.

Following the extrusion procedure, the extrudate is compression-molded, to form a 15.24 cm by 15.24 cm by 1.27 cm slab, in a Carver Laboratory Press, Model M, 25 Ton. The press is operated at a temperature of 150 °C and an applied load of 25,000 pounds. After the compression, the formed slabs are left to cool and settle for a minimum period of 96 hours before being cut into various test samples.

3.4 Property Measurement Experimental Set-Up

Two identical test samples are cut from each composite slab for the thermal property test. All surfaces of the test samples are machined to leave them flat and smooth. The sample dimensions are 7.62 cm by 5.08 cm by 1.02 cm. A mica heater of the same length and width as the sample and 0.0876 cm thick is placed between the two identical samples, as shown in Figure 3.1, to supply the heat. The surface of the sample in contact with the heater (Figure 3.1, $x = a$) is denoted the front and the opposite one across the sample thickness ($x = b$) is denoted the back. With this arrangement, heat flow into the composite samples is in the positive and negative x direction and the surface area over which the heat is applied is 38.71 cm^2.

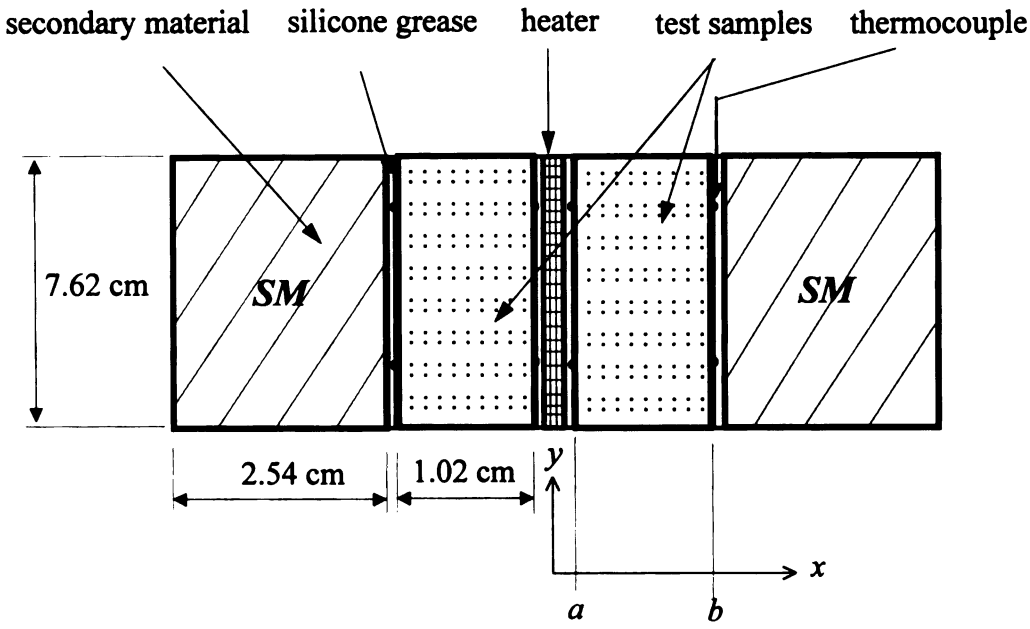

Figure 3.1: Sample arrangement for property measurement test

We see from chapter 2, that only the transverse component (perpendicular to flame spread direction) of thermal conductivity of the burning solid fuel has an influence on the rate of spread. For this reason, it is the transverse components of the effective thermal properties of the composite that are desired to be established in this section. As will be seen later in chapter 5, flame spread rates are measured over thermally thick composite samples that are 15.24 cm in length, 5.08 cm in width, and 1.02 cm thick. The flame is initiated across the width at one end and travels the whole length of the sample. Hence, the relevant transverse direction is perpendicular to the 15.24 cm by 5.08 cm surface and into the solid. For a one-dimensional analysis, therefore, the appropriate transverse properties will be those measured from the analysis of transient heat flow between two opposite surfaces across the sample thickness as in the set-up employed herein.

ext
ali
me
tra
con

sec
on
exp
the
cor
the
res

rec
the
thi
as s
in o

trans

Based on the orientation of the rotating screws and that of material flow inside the extruder, if the wood fibers are considered to be cylindrical in shape, their lengthwise alignment will be in the y direction of Figure 3.1. The thermal properties that will be measured from the test configuration shown in the figure will in this case be the transverse components. If the fibers are spherical, however, the thermal properties can be considered isotropic. This significance of this point will be clear after reading section 3.5.

A secondary material is placed in contact with the sample at the back surface. This secondary material can either be an insulation or a highly conducting material depending on the nature of the material whose thermal properties are being measured. If the expected thermal conductivity of the test material is low (less than about ten times that of the insulation material to be used, for instance) a better result will be obtained if a highly conducting material, e.g. an aluminum block, is used as the secondary material. Such is the case for the wood fiber/HDPE composites; the use of aluminum blocks gave better results as will be shown shortly.

Type E thermocouples, 0.008 cm in diameter, are attached to the test samples to record the temperature history. A total of six thermocouples is used per sample, four at the front surface, two at the back. To reduce the influence of imperfect thermal contact, a thin layer of Dow Corning 340 Silicone Grease is introduced between adjacent surfaces as shown in the figure. The whole assembly is then placed inside a well-controlled oven in order to conduct the tests at various levels of initial temperature.

The temperature response of the material layers of Figure 3.1 is governed by the transient, one dimensional, heat conduction equation

$$\frac{\partial}{\partial x}\left(\lambda \frac{\partial T}{\partial x}\right) = \rho C \frac{\partial T}{\partial t}, \tag{3.5}$$

applied to each individual layer in turn and coupled through the interface conditions

$$\lambda_s \left.\frac{\partial T_s}{\partial x}\right|_{L_s^-} = \lambda_{s+1} \left.\frac{\partial T_{s+1}}{\partial x}\right|_{L_s^+}, \quad T|_{L_s^-} = T|_{L_s^+} \tag{3.6}$$

for any two adjacent layers s and $s+1$. A variable heat flux boundary condition is applied at the front surface ($x = a$) and a zero heat flux or a temperature boundary condition is applied at the back surface ($x = b$), depending on whether the insulation or the aluminum block is used as the secondary material. The temperature distributions obtained from the inverse numerical solution of these equations are used with the experimentally measured values and the heating power to estimate the effective thermal properties λ and ρC of the composite. The procedure involves the minimization, with respect to the parameters λ and ρC, of the sum of squares function $\sum_{i=1}^{N}\left[\left(Y_i - T_i\right)^2\right]$, where N is the number of temperature data points taken.

This experimental set-up is well tested and has been used satisfactorily to measure the thermal properties of such materials as aluminum and carbon-carbon composites (Dowding et al. [48]), and thermosetting carbon/epoxy composites (Scott and Beck [49]), to mention just a few. The method has the advantage that both the thermal conductivity and the volumetric heat capacity of the test material are determined simultaneously from the same transient temperature measurements [50]. Further details of the property estimation procedure and of the general solution method for inverse heat conduction problems are available in the literature [51-53].

As mentioned earlier, there are two possibilities for the secondary material placed at the back surface of each test sample. It can either be an insulation or a highly conducting material. The choice must be made such that the experiment is well-designed. For the sequential parameter estimation procedure [51] employed herein, the use of the appropriate mathematical model and a well-designed experiment should result in the sequential parameter estimates having constant values in the latter part of the test after possible initial fluctuations. Also, the residuals (deviation of the calculated temperature values from the experimental ones, $Y_i - T_i$) should be small, relative to the temperature rise, ΔT attained during the test, and be random in nature.

Typical transient temperature profiles measured during tests conducted on the polyethylene matrix are shown in Figure 3.2. The profiles shown in Figure 3.2a are for the case where a block of aluminum was placed in contact with the sample back surface while those in Figure 3.2b are for the case of insulated test sample back surface. For the later case, the heat was turned off close to the end of the test (at $t = 210\ s$), see Figure 3.2b, since it has been reported in the literature that such procedure produces better results [52]. The test duration, t was chosen so that the dimensionless time, t^+ ($t^+ = \alpha t / l^2$, α is thermal diffusivity and l is sample thickness across which the heat flows) was approximately 3.0 and 0.7 for the two cases respectively. These values ensure that while there is ample time for the heat signal to penetrate the samples the heat transfer process does not become quasi steady.

The corresponding sequential estimates of the thermal conductivity λ and the volumetric heat capacity ρC are shown in Figures 3.3 (a) and (b).

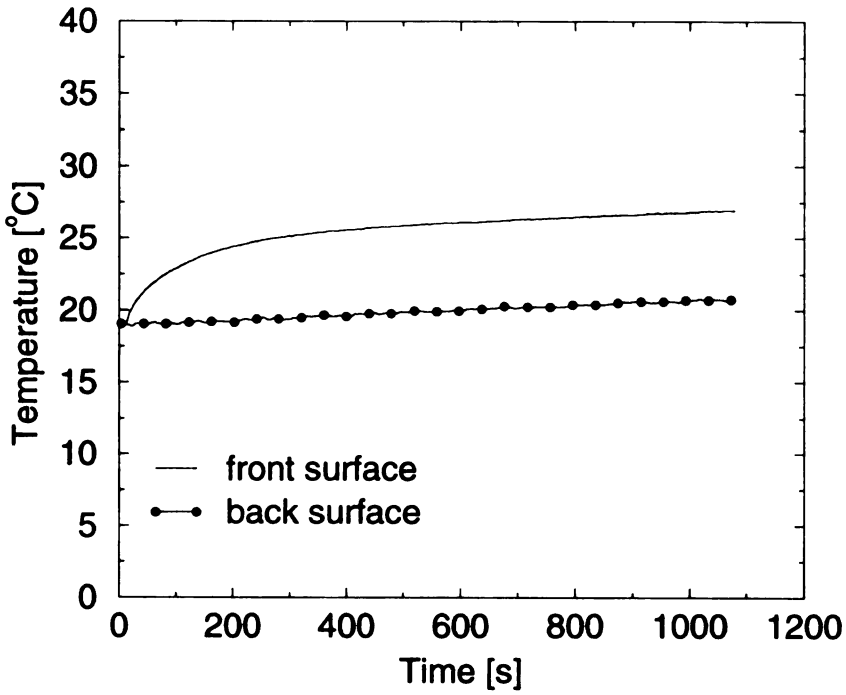

(a)

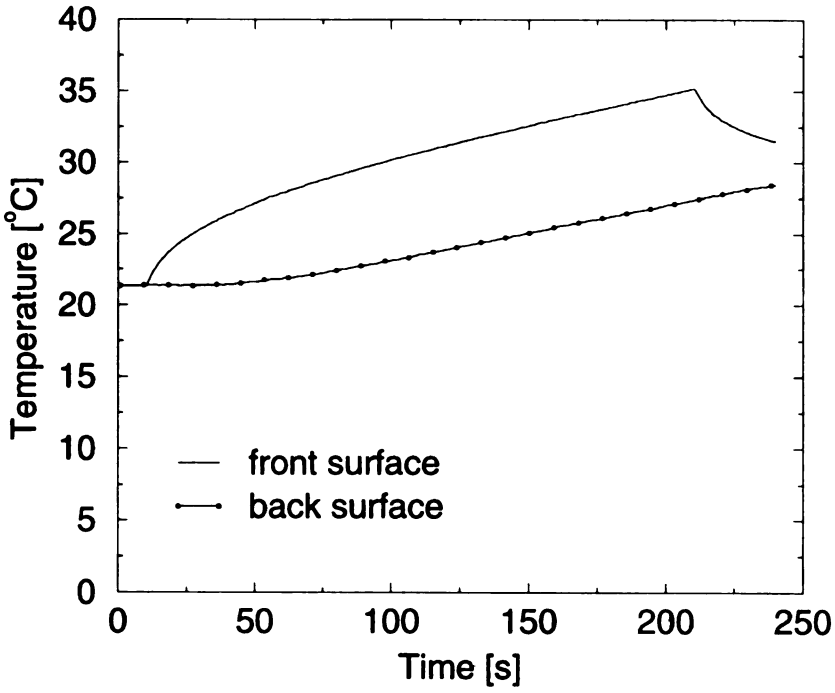

(b)

Figure 3.2: Transient temperature profiles; (a) aluminum block placed at back surface, (b) back surface of sample insulated

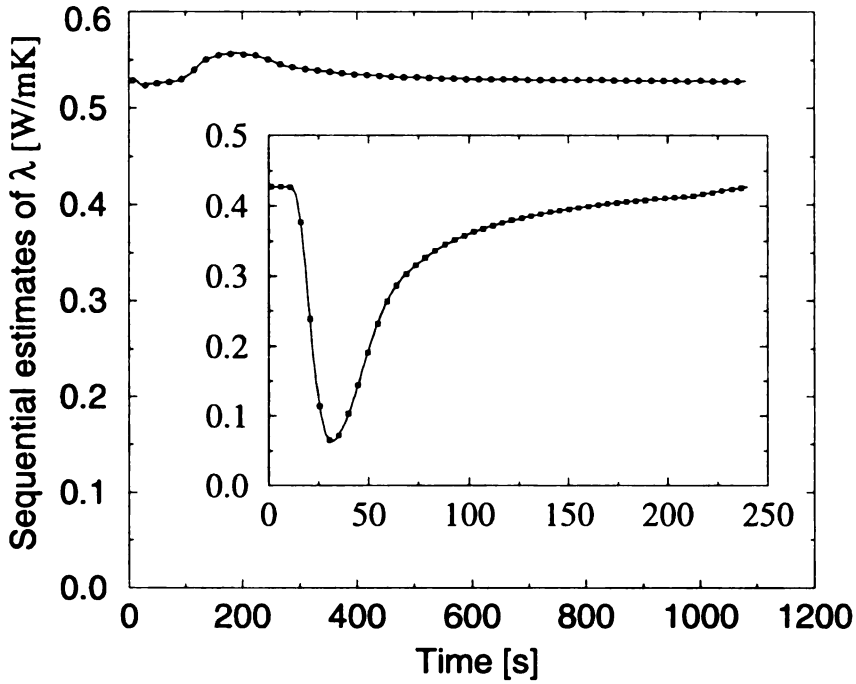

(a)

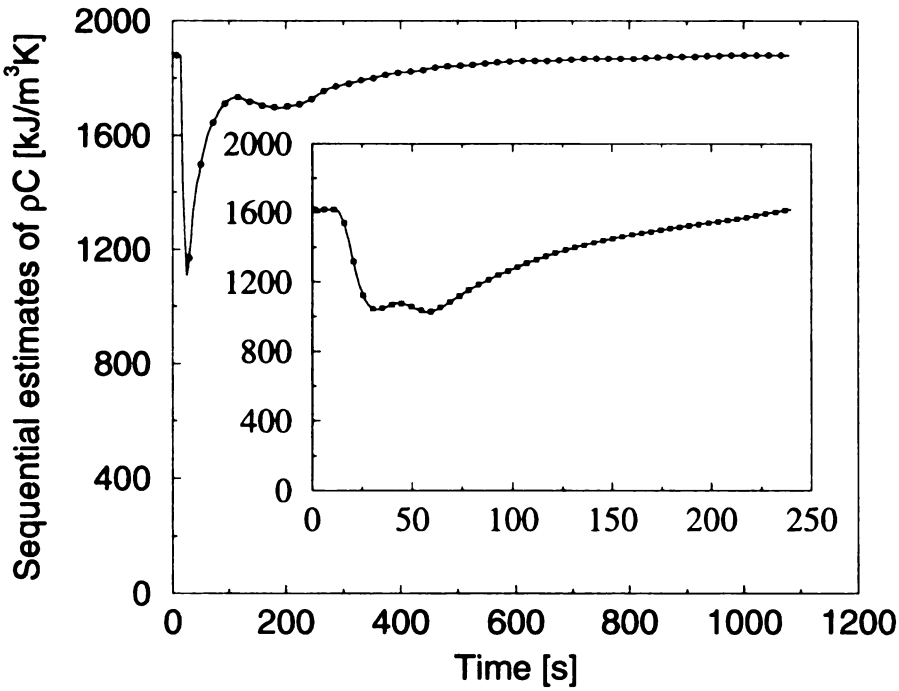

(b)

Figure 3.3: Sequential parameter estimates of λ (3.3a) and ρC (3.3b); inserts represent the case of insulated test sample back surface.

It can be seen that the experiment with aluminum block placed in contact with the test sample back surface is better, based on the requirement that the sequential parameter estimates should eventually have approximately constant values. The plot of the residuals, normalized by the temperature rise attained during the test, also supports the same conclusion. As shown in Figure 3.4, the residuals associated with the placement of aluminum blocks at the back of the test samples are not only significantly smaller, they are also more randomly distributed, in contrast to those associated with insulated back surface. Consequent upon these observations, all property tests were conducted with a block of aluminum, 7.62 cm by 7.62 cm by 2.54 cm, placed in contact with the back surface of each test sample.

3.5 Results and Discussion

The variation of the effective thermal conductivity of the composite with initial sample temperature, for various wood fiber mass fractions ϕ, is shown in Figure 3.5. With the temperature rise during a given test maintained at approximately 8 °C, the initial sample temperature at which the tests were conducted was limited to 60 °C in order to keep the sample temperature at any time from approaching the melting point of the material.

For the "pure" polymer, $\phi = 0$, the thermal conductivity decreases with rise of temperature at a rate that seems to decrease as temperature is increased. These results agree well with those available in the literature, where it has been noted that, for temperatures above the glass transition temperature (about -80 °C for polyethylene), the thermal conductivity decreases with increase of temperature [54].

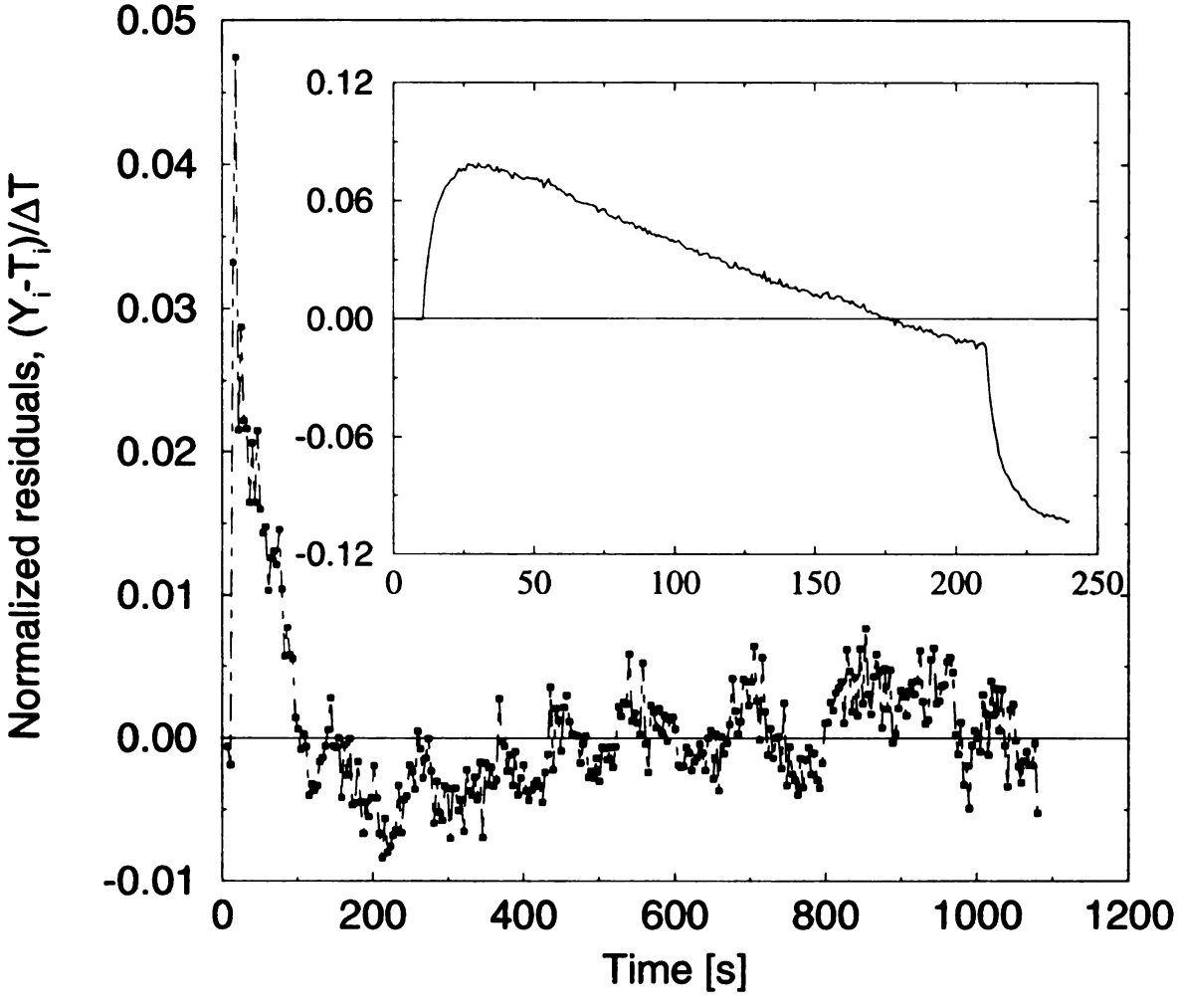

Figure 3.4: Plot of normalized residuals (insert is for insulated back surface)

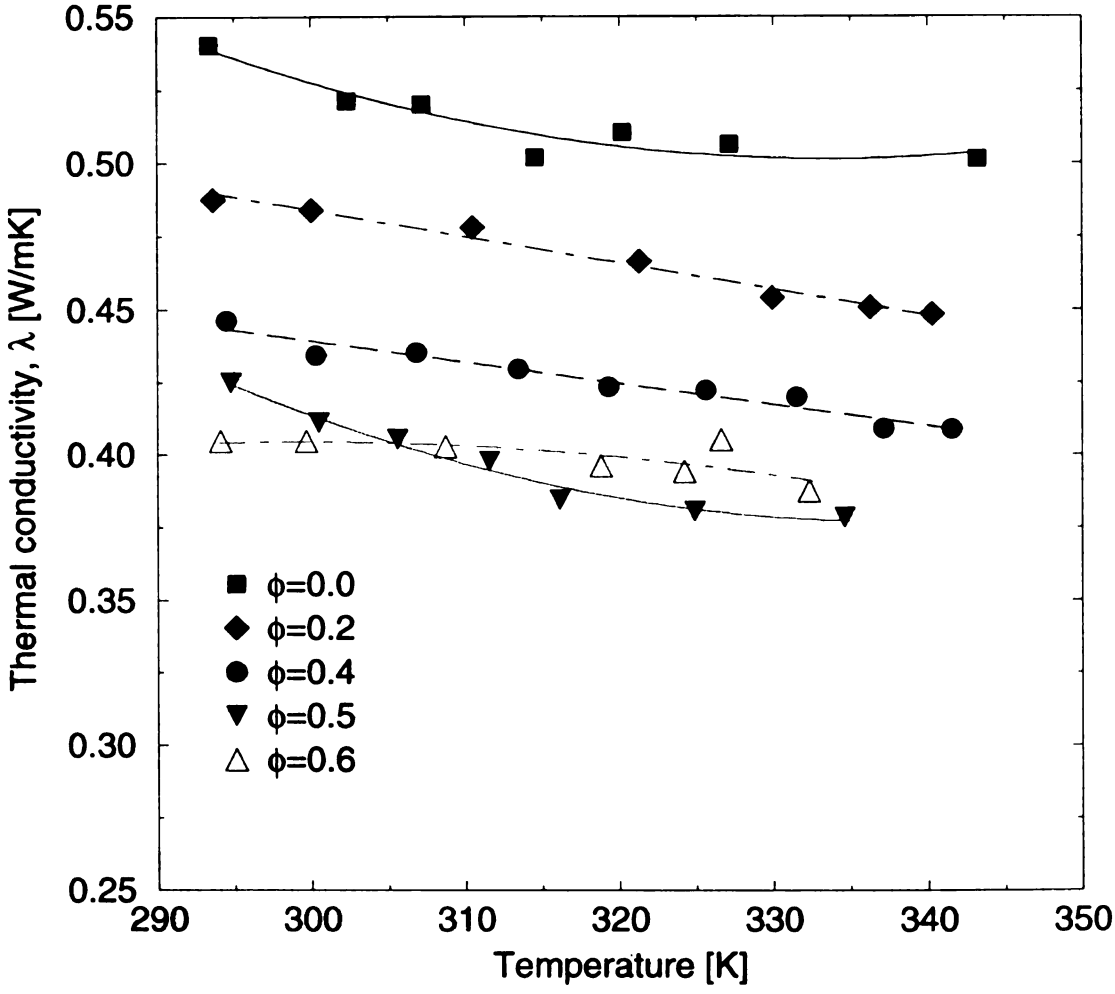

Figure 3.5: Variation of effective thermal conductivity with initial sample temperature

With the addition of the wood fibers reaching to a fiber mass fraction (ϕ) of 0.4, the effective thermal conductivity of the composite decreases, almost linearly, with rise of temperature. As the wood fiber content of the composite is increased to a high value ($\phi = 0.6$), its effective thermal conductivity becomes almost invariant with temperature.

The graph of the effective volumetric heat capacity, ρC, of the composite with temperature is shown in Figure 3.6. It can be seen that the wood fibers introduce some thermal stability to the polymer. Whereas the heat capacity for the polyethylene ($\phi = 0$) increases rapidly with temperature, the increase for the composites ($\phi > 0$) is gradual and linear in nature. It can also be seen from the figure that the effective heat capacity decreases with increase of wood fiber mass fraction in the intermediate and high fiber mass fraction range, especially at temperatures exceeding about 40 °C. At very low values of ϕ, however, the values of ρC are least and out of trend.

Attempts were made to identify the reasons for the seemingly anomalous behavior observed at $\phi = 0.2$. Physical observations of the composites and SEM pictures of their inner structures revealed the presence of air voids which generally decrease in occurrence as the wood fiber mass fraction is increased and becomes a rarity for $\phi \geq 0.3$. Therefore, one possibility is that the wood fibers act more like "defect sites", characterized by voids and gaps within the composite, until a critical fiber mass fraction (which appears to be 0.3) is exceeded, in similar manner to what occurs in fracture mechanics. The presence of these voids would lead to a significant decrease in the effective volumetric heat capacity of the composite owing to the low heat absorbing capacity of air compared to the wood

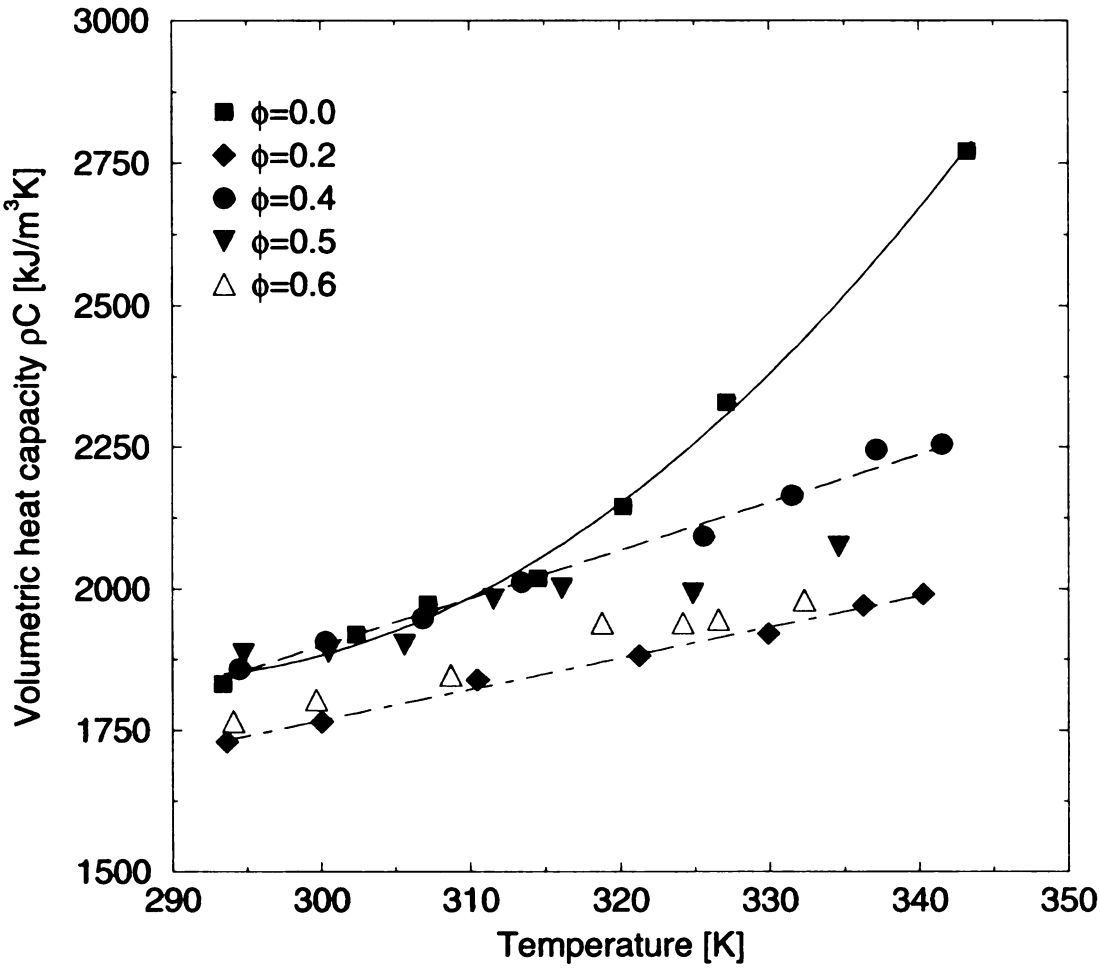

Figure 3.6: Plot of the effective heat capacity of the composite with temperature

fibers and the plastic. Interested readers seeking to view the SEM photographs may consult references 55 to 57.

The values of the thermal conductivity (λ) and the volumetric heat capacity (ρC) reported above were used to calculate values of the thermal diffusivity, α ($\alpha = \lambda/\rho C$) and the thermal responsivity, φ ($\varphi = \lambda\rho C$). These properties are important when dealing with heat conduction and flame spread problems, respectively.

The effective thermal diffusivity of the composite, shown in Figure 3.7, decreases linearly with rise of temperature for all values of the wood fiber mass fraction. However, the decrease is more gradual for the composites in contrast to the behavior exhibited by the polymer. Furthermore, the diffusivity of the composites does not change significantly with composition when the wood fiber mass fraction is 40% or more.

In contrast, the effective thermal responsivity of the composite increases slightly (and linearly, too) with temperature for $0.2 \leq \phi \leq 0.4$, but is insensitive to temperature variation when $\phi > 0.4$ (see Figure 3.8). For the HDPE ($\phi = 0$), the estimates rise rapidly with increase of temperature in a non-linear manner. These results again revealed that the wood fibers introduce thermal stability to the polymer.

These results have two significant implications for flame spread studies. The first is that an assumption of a constant material property, commonly made in many numerical studies, becomes reasonable in the temperature range $290\ K \leq T \leq 340\ K$. The problem is complicated enough already without having to include material properties that vary with temperature! The second is that, provided $\phi > 0.4$, the thermal behavior of the composite

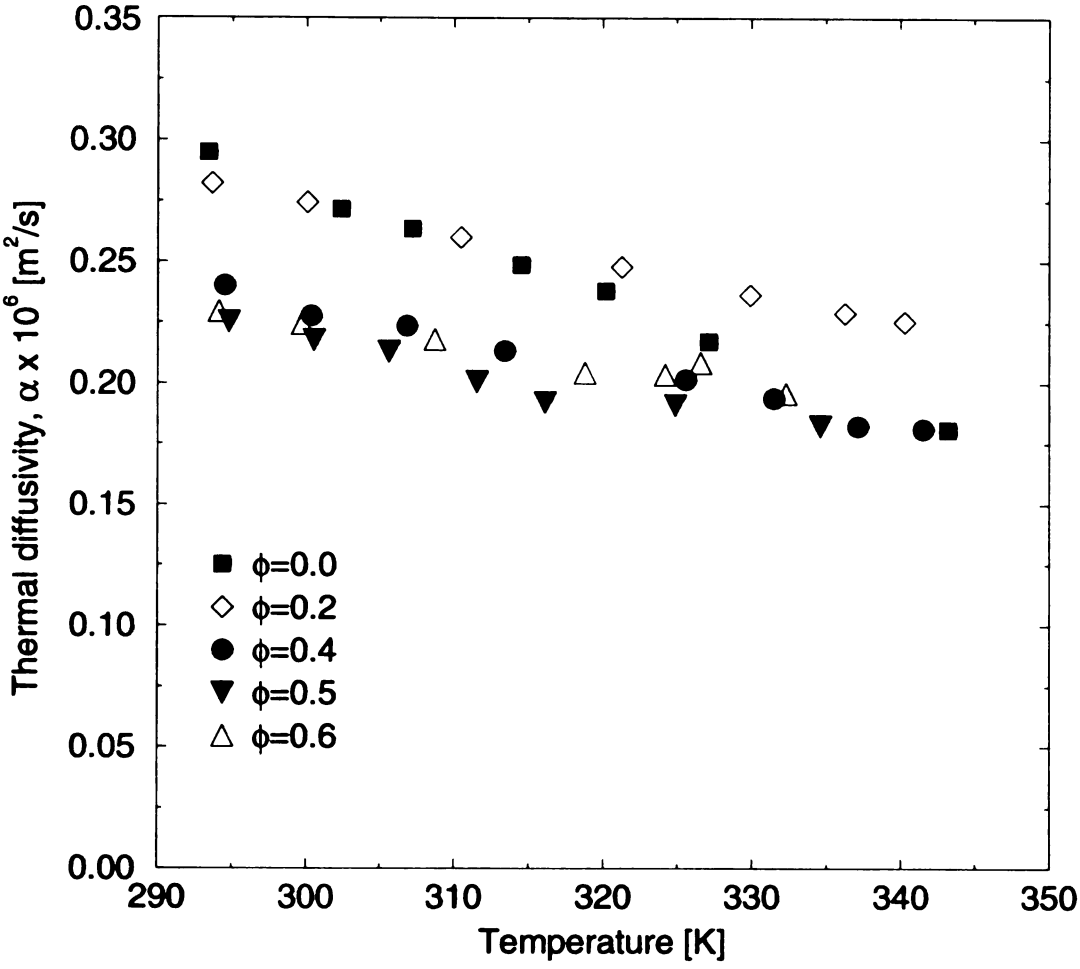

Figure 3.7: Variation of effective thermal diffusivity with sample temperature

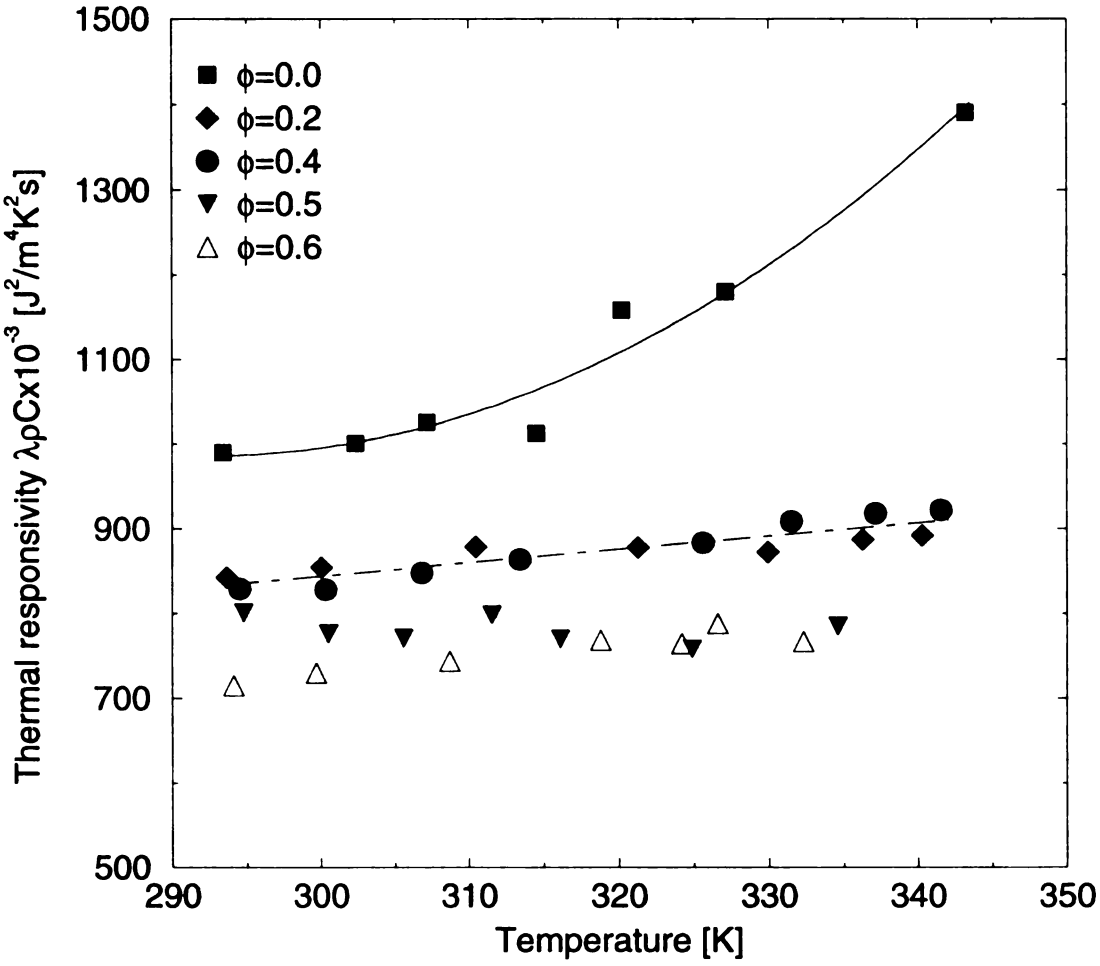

Figure 3.8: Plot of the effective thermal responsivity with temperature

will not change for the worse if the fiber mass fraction is increased. This means that if the composite with $\phi = 0.4$ does not burn without external support, e.g. background radiation of heat to the flame, for instance, one can conclude that it still will not burn without external support when ϕ is raised to 0.5 or 0.6. This point is crucial in the determination of composite composition that results in the best fire safety characteristics.

In the temperature range $290K \leq T \leq 350K$ covered in these tests, the composite thermal diffusivity and responsivity data, shown in Figures 3.7 and 3.8, can be correlated using a linear function $p_c = f + gT$, where T is the absolute temperature in kelvin. A quadratic fitting function of the form $p_c = f + gT + hT^2$ is found to be more appropriate for the data on polyethylene ($\phi = 0$). In this latter case, the constants f, g, and h have values 0.9578 m^2/s, –0.00226 $m^2/s.K$ and 0.0 (zero) respectively for thermal diffusivity correlation and 14602.2 $J^2/m^4.K^2.s$, –93.13 $J^2/m^4.K^3.s$ and 0.16 $J^2/m^4.K^4.s$ for thermal responsivity. For the data on the composites ($0 < \phi < 1$), the corresponding values of the constants are shown in Table 3.1. In using these correlations, the individual values of λ and ρC can be computed, if necessary, from values of α and φ calculated using the appropriate function and values of the constants.

In order to confirm whether the properties of the composite, p_c can be predicted with sufficient accuracy from those of the wood fibers, p_f and the polymer matrix, p_m using the simple rule of mixtures, $p_c = p_f V_f + p_m V_m$, the variation of the thermal conductivity of the composite at room temperature is plotted with wood fiber mass fraction in Figure 3.9. For comparison purposes, the predictions of some theoretical functions available in the literature, as given in Equations 3.1 to 3.4, are also plotted. For

the cylindrical inclusion model and the Ziebland model, the appropriate equations used for comparison purposes are Equations 3.3 and 3.4 which predict the transverse components of the effective thermal conductivity, the components that will be measured from the experimental setup of Figure 3.1 if the composite material is anisotropic and the wood fibers are considered to be cylindrical.

Assuming there are no air voids in the composite ($V_f + V_m = 1$, where V is volume fraction and subscripts f and m represent fiber and matrix, respectively), Oladipo et al. [31] showed that V_f is related to ϕ by

$$V_f = \frac{\rho_m}{\rho_f}\phi\left[1-\left(1-\frac{\rho_m}{\rho_f}\right)\phi\right]^{-1}, \tag{3.6}$$

with the matrix and the wood fiber densities ρ_m and ρ_f, having values 985 and 1144 kg/m^3, respectively. The density of the wood fibers was determined by plotting the experimental values for the composite with ϕ and then extrapolating the results to $\phi = 1$.

Table 3.1: Correlation constants for thermal diffusivity and thermal responsivity data

	Thermal Diffusivity $\alpha \times 10^6$ (m^2/s)		Thermal Responsivity $\lambda\rho C \times 10^{-3}$ (J^2/m^{4}K^{2}s)	
ϕ	f (m^2/s)	g (m^2/sK)	f (J^2/m^{4}K^{2}s)	g (J^2/m^{4}K^{3}s)
0.2	0.6438	−0.001233	588.02	0.89
0.4	0.6009	−0.001232	73.62	1.57
0.5	0.5478	−0.001102	775.00	0.00
0.6	0.4717	−0.000825	65.00	0.00

To calculate the values of λ for a given ϕ, Equation 3.6 is used to calculate V_f and the result is substituted in Equations 3.1 to 3.4.

As seen from Figure 3.9, the prediction of the spherical inclusion model (Equation 3.2) agrees excellently with the experimental results. This agreement means that the wood/HDPE composite can be considered to be roughly isotropic in terms of the effective thermal conductivity. The rule of mixtures (Equation 3.1) and the cylindrical inclusion model (Equation 3.3) produce results that are slightly higher than the experimental values, the predictions of the former being slightly superior to those of the latter. On the other hand, the Ziebland function under-estimated the thermal conductivity, having the largest margin of error of the four models. The agreement between the predictions of the spherical inclusion model and the experimental results is consistent with physical observation of the fibers which reveal the wood fibers to be mostly spherical particles uniformly distributed within the composite.

The values of λ at three different levels of temperature are shown in Figure 3.10, together with the equivalent predictions of the spherical inclusion model. The values of λ at $\phi = 1$ were obtained by extrapolating the experimental results obtained for $0 \leq \phi \leq 0.6$. It can be seen from the figure that the spherical inclusion model consistently produces results that agree very well with the experimental data.

The effective volumetric heat capacity of the composite exhibits a nonlinear relationship with ϕ except at temperatures exceeding about 55 °C, see Figure 3.11. The values of ρC shown in the figure for $\phi = 1.0$ were established from tests conducted on the wood fibers using Differential Scanning Calorimeter (DSC). The thermal property

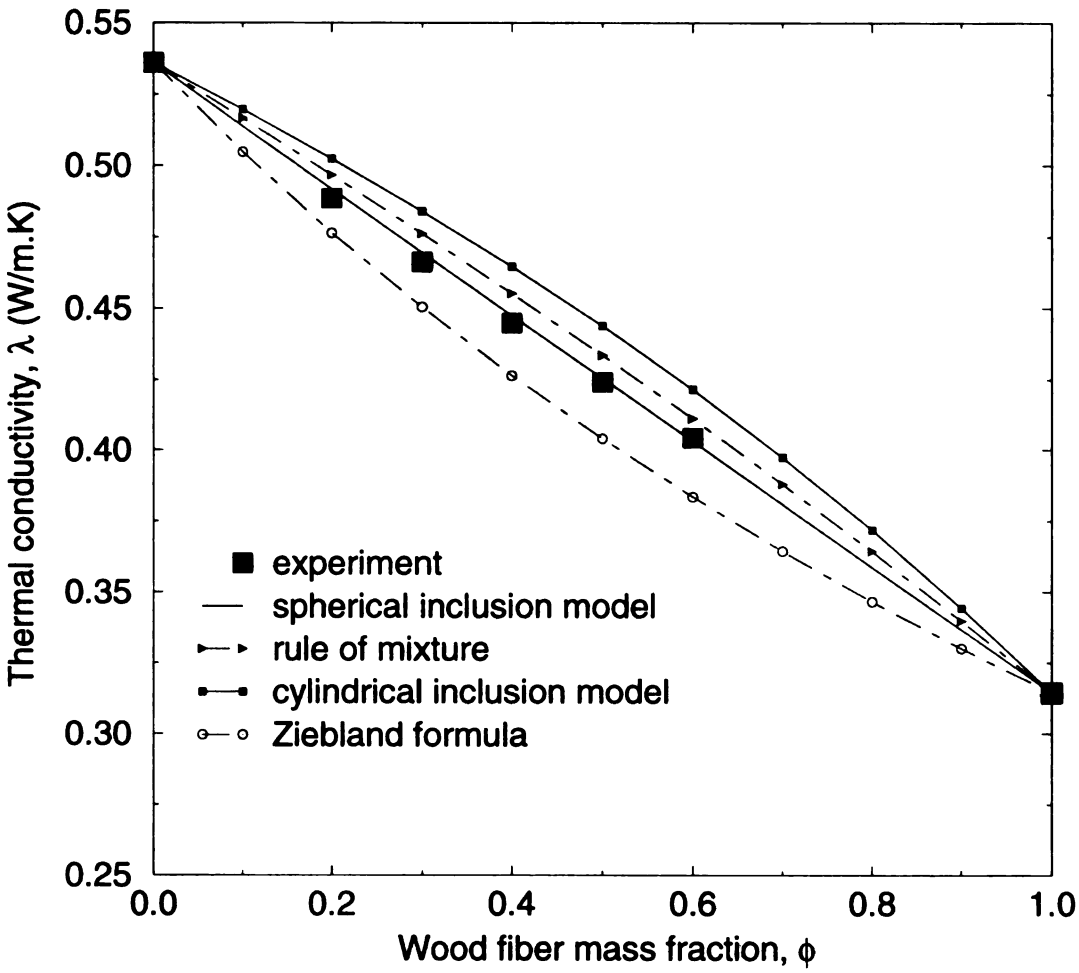

Figure 3.9: Comparison of various models for predicting λ

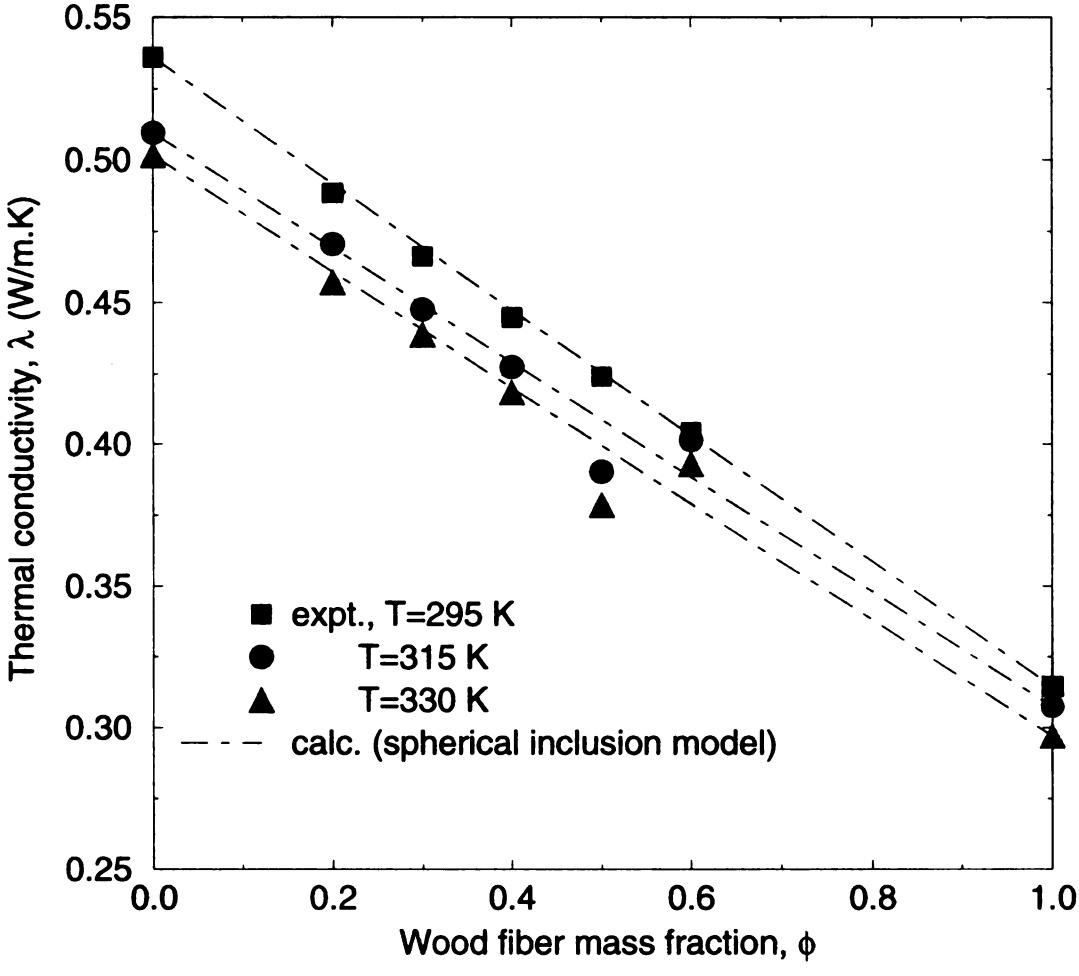

Figure 3.10: Plot of effective thermal conductivity of the composite with ϕ

experimental set-up described in this chapter cannot be used for this case since it is not possible to make samples of only wood fibers (some binder is needed to hold the wood fibers together). As mentioned earlier, what appear as anomalous behavior (demonstrated by low and out-of-trend values of ρC) at $\phi = 0.2$ may be due to the formation of voids resulting from the wood fibers acting as defect sites at low fiber volume fractions.

The effective volumetric heat capacity data are best correlated with ϕ in the form:

$$(\rho C)_c = (\rho C)_f \phi + (\rho C)_m (1-\phi) + d\phi(1-\phi), \qquad 0.3 \le \phi \le 1.0, \qquad (3.7)$$

where d is a constant. It can be seen that this is really an extension of the linear rule of mixtures (based on mass fraction instead of volume fraction) with a second order term in ϕ included via constant d. The value of d determines the shape of the property curve; $d < 0$ gives a concave appearance, $d = 0$, linear, and $d > 0$, convex. For the data shown in Figure 3.11, d has the values 567.3, 464.6 and 35.2 kJ/m^3.K for temperatures 295, 315 and 330 K, respectively. These values show that the prediction of ρC with the simple rule of mixtures will give accurate results only if $T \ge 330$ K.

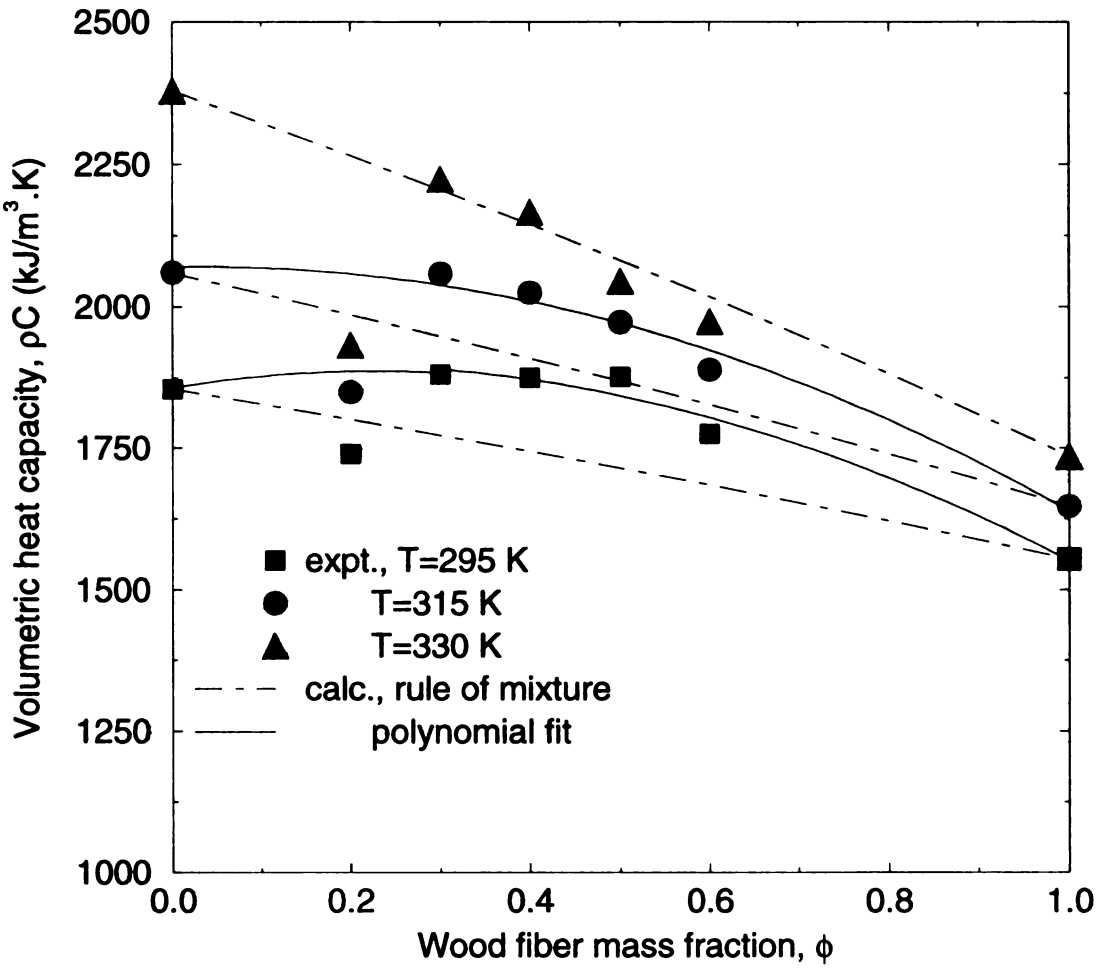

Figure 3.11: Plot of effective volumetric heat capacity with fiber mass fraction

3.6 Conclusions

In this chapter, the thermal properties of the composite, which will be needed later for flame spread modeling, were determined. The correlation functions that can be used for predicting the composite thermal properties, given the composition and temperature, were established. The accuracy to which the simple rule of mixtures can be used for estimating the effective thermal properties was also evaluated.

The results have shown that variations of the effective thermal properties of the composite with temperature diminish as the wood fiber mass fraction is increased. For composites containing 50% or more wood fibers by mass, the effective thermal responsivity is essentially invariant with temperature while the effective thermal diffusivity changes only slightly. It can be concluded that the composite containing 50% wood fibers and 50% polymer matrix will exhibit the best fire safety properties while still retaining the desired characteristics that originate in the polymer, e.g. ease of manufacture, toughness, etc.

The results have also shown that the spherical inclusion model produces the best predictions of the effective thermal conductivity with the implication that this property of the composite is close to being isotropic. In comparison, the rule of mixtures slightly over-predicts the effective thermal conductivity. For the effective specific heat, however, the rule of mixtures is inadequate for predictive purposes. A more complicated correlation function, such as a quadratic function, is needed. The results also suggest that the assumption of constant properties in numerical models for calculating the rate of flame spread over the composite will not lead to significant errors provided the wood fiber mass fraction is 40% or more and the initial temperature is between 290 and 340 K.

CHAPTER 4

APPLICATION TO THERMAL BARRIER MATERIALS SEPARATING AUTOMOBILE ENGINE AND PASSENGER COMPARTMENTS

4.1 General

In this chapter, the methods described in the preceding chapter are utilized to study the thermal effectiveness of several materials used in the automobile industry as part of the fire barrier layer separating the engine compartment from the passenger cabin. The materials, supplied by General Motors Research Department, include glass fiber bonded with phenol formaldehyde; rubber; MgO; Kaowool ceramic fiber; carpet material and a few others not identified by name. The objective of the study is to accurately determine the thermal conductivity, λ and the volumetric heat capacity, ρC of these materials and then use the information to conduct numerical simulations aimed at understanding the role of each material when used as part of the fire barrier layer. Although not directly related to the flame spread issues of this thesis, the results of this study are nevertheless included to demonstrate the versatility of the experimental methods adopted in chapter 3.

4.2 Physical Arrangement of Automobile Fire Barrier Layers

Typical arrangement of the fire barrier layers in the automobile assembly is shown in Figure 4.1. The bulkhead layer is the steel wall that separates the engine compartment from the passenger cabin. The dash and sound blankets are placed next to the bulkhead layer on the passenger and the engine side, respectively. It must be noted that the dash

Fig

and

mat

rubb

0.3

blan

4.3

In pur

therm

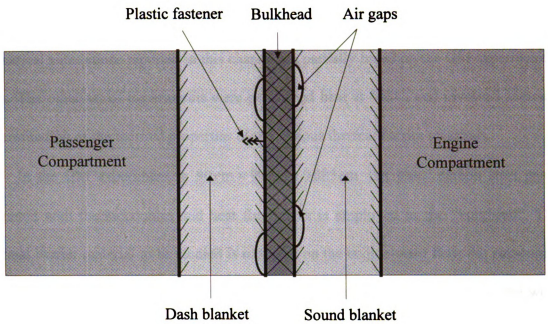

Figure 4.1: Bulkhead assembly separating engine and passenger compartments, including the dash blanket, the sound blanket, and the bulkhead. The blankets are attached by plastic fasteners, and air gaps may exist between the bulkhead and the blankets, leading to altered thermal insulation behavior. Note that the dash and sound blankets may each be multi-layered media.

and sound blanket can be layered materials themselves, consisting of several separate materials. The sound blanket for the Cadillac, for instance, consists of a 0.14 cm layer of rubber sandwiched between two layers of glass fiber mats whose thickness varies from 0.3 to 0.95 cm. The materials examined herein are typically used as part of the sound blanket, thus performing the dual roles of thermal insulation and engine noise attenuation.

4.3 Experiments

In pursuing the objective of understanding the effectiveness of the various materials as a thermal barrier, two sets of experiments were performed. The first set were performed at

General Motors (GM) Research Center by GM personnel and involved transient temperature measurements on a mock bulkhead and sound blanket assembly. Some of the numerical simulations reported in this chapter are partially based on the GM experimental data. The other set of experiments were performed here at MSU, and involved accurate determination of the thermal properties of the various thermal barrier materials.

In the GM experiment, a $90\,\text{cm} \times 90\,\text{cm} \times 0.085\,\text{cm}$ flat black carbon steel panel mounted with thermocouples and heat flux gages is employed as the "bulkhead". The thermal barrier material to be studied is mounted on the engine-ward face; the passenger-compartment side is left "bare". A flux of heat on the engine side impinges on the wall. The heat flux is supplied from several halogen lamps located at controlled distances from the bulkhead assembly. There are no fissures or gaps in this hypothetical bulkhead apparatus unlike the more realistic picture shown in Figure 4.1. A bulkhead with gaps would simulate a bulkhead that had been torn in a crash, for example. There is a provision for varying the bulkhead angle, relative to the heater, in order to simulate the realistic situation of a non-vertical bulkhead. The impinging heat flux is mostly one-dimensional in a relatively small $15\,\text{cm} \times 15\,\text{cm}$ area in the center of the plate. After establishing the desired emission from the lamps, the heat flux through the barrier and the temperature profiles are measured with gauges and thermocouples, respectively.

The experimental methods employed at MSU for determining the thermal properties of the materials are as described earlier in chapter 3. As explained in the chapter, the possibility of successfully estimating the two thermal properties, λ and ρC, can be predicted from the sensitivity coefficients with respect to the two parameters. For the

experiment to be well-designed and capable of producing accurate estimates of the material thermal properties, the magnitudes of the modified sensitivity coefficients, $\lambda \frac{\partial T}{\partial \lambda}$ and $(\rho C)\frac{\partial T}{\partial (\rho C)}$, must be significant relative to the temperature rise, ΔT, attained during the test and must not be auto-correlated. Another indication of a good estimation procedure is that the sequential estimate values of the parameters will be constant in the latter part of the test after possible initial fluctuations. Furthermore, the residuals $(Y_i - T_i)$ should be small, in comparison to the temperature rise and be random in nature. If these conditions do not hold, it may not be possible to estimate the two properties uniquely but only a ratio of the two. In such a case, it will be necessary to employ other methods for determining one of the properties.

The typical transient temperature profiles measured during the experimental tests are shown in Figure 4.2. The test duration was chosen so that the dimensionless time was approximately 4.0. Again, this value ensures that while there is ample time for the heat signal to penetrate the samples, the heat transfer process does not become quasi-steady.

Plots of sensitivity coefficients from tests conducted on glass fiber mat and glass fiber mat with facing polyester scrims are shown in Figure 4.3. It can be seen from these plots that the experiment is insensitive to the heat capacity of the materials. With ΔT approximately equal to 10 °C for both tests, the maximum value of $(\rho C)\frac{\partial T}{\partial (\rho C)}$ is only about 2% of the temperature rise which is very small indeed. On the other hand, the sensitivity coefficient with respect to the thermal conductivity reached as high as 25%.

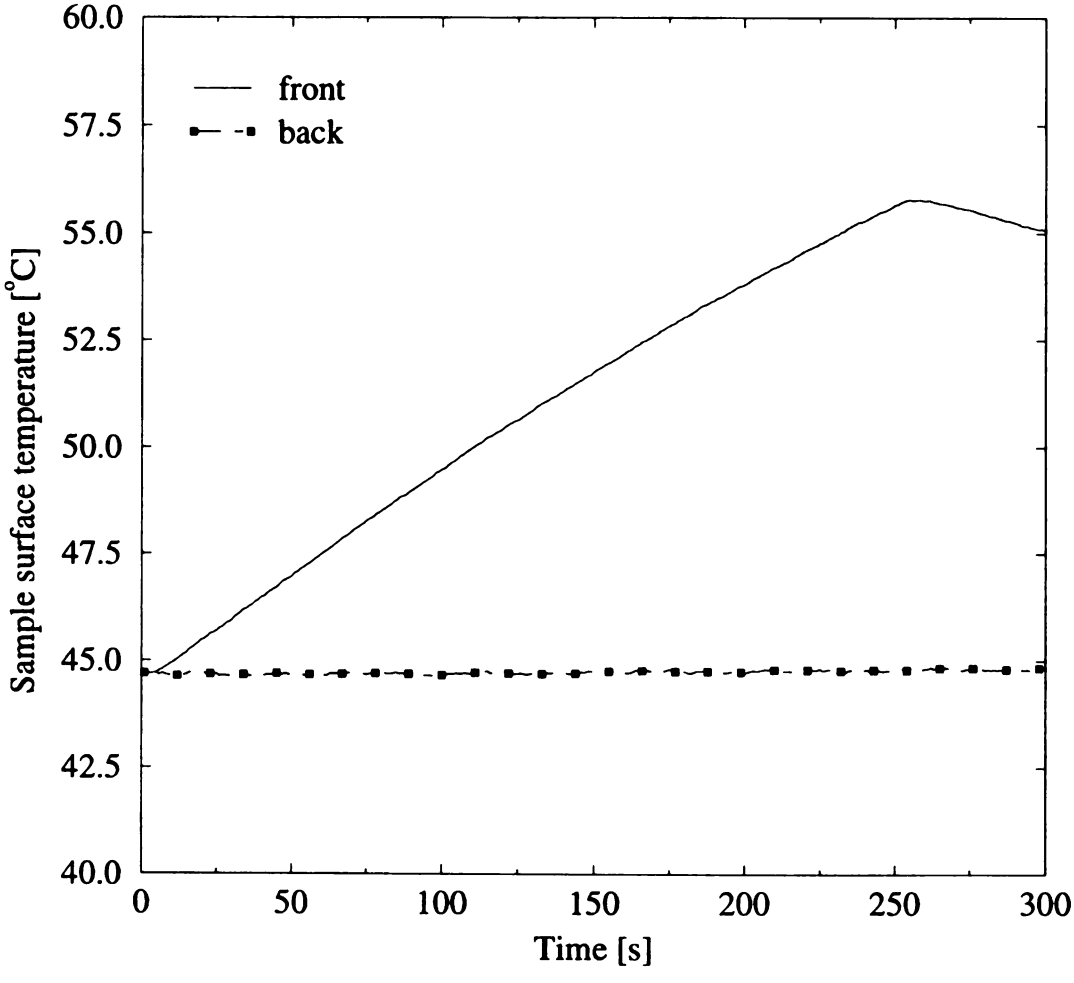

Figure 4.2: Transient temperature profile, $q_o'' = 250$ W / m^2

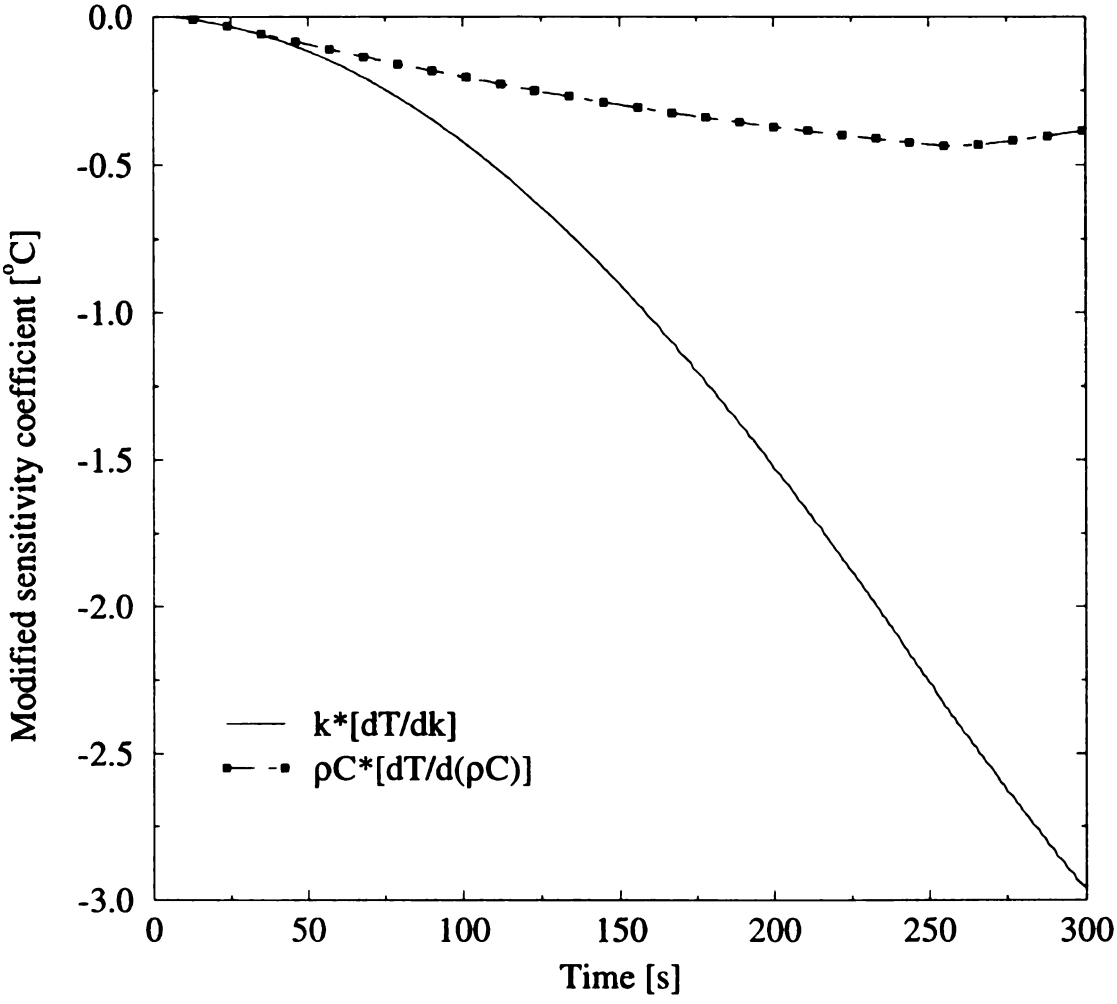

Figure 4.3: Plot of modified sensitivity coefficients

For this reason, only the thermal conductivity of the thermal barrier materials could be accurately established from the experimental methods described in chapter 3.

In order to determine the volumetric heat capacity of the materials the differential scanning calorimeter (DSC) was used. This equipment is widely used for such purposes and is highly specialized. It utilizes the difference in transient temperature readings between a reference empty aluminum pan and another aluminum pan containing a very small amount, usually between 10 to 20 mg, of the test material in order to compute the heat capacity of the test specimen. A discussion of the principles and the operational methods of this equipment is readily found in the literature.

4.4 Results and Discussion

The plots of the specific heat capacity of the thermal barrier materials as measured with the DSC method are shown in Figure 4.4. We can see from the plots that the specific heat capacities of all the materials rise with temperature. It is to be noted also that the addition of a polyester layer to the glass fiber mat (said to be aimed at preventing itching that may result from working with the bare glass fiber mat [58]) increases the specific heat capacity significantly. Finally, the results show that the heat capacity of the rubber and the glass fiber mat with both-side facing polyester layers are identical. Hence, the use of rubber in between two layers of glass fiber mat in the Cadillac sound barrier wall does not result in any significant changes in the specific heat capacity of the barrier provided both sides of the wall are covered with the polyester scrims.

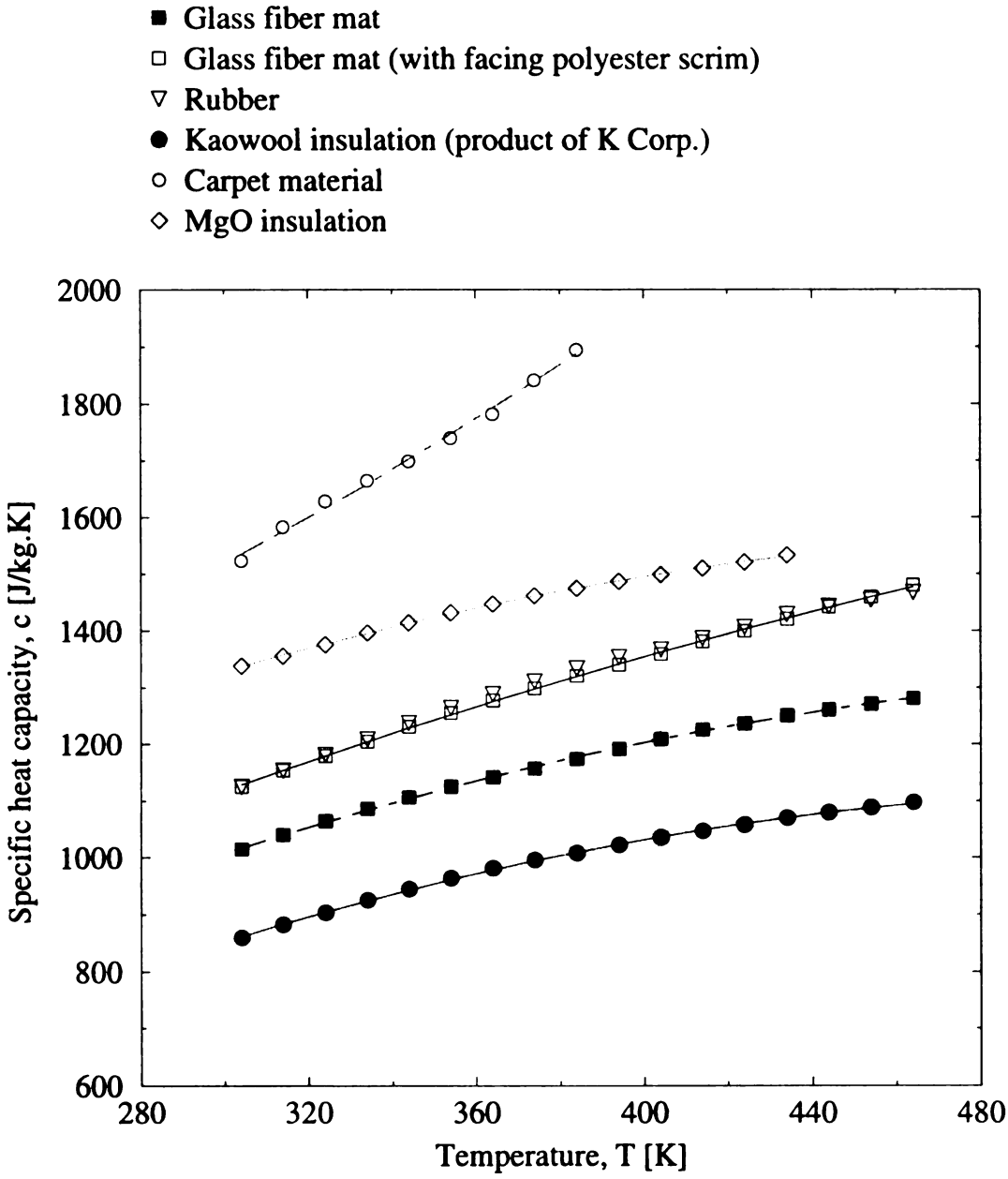

Figure 4.4: Specific heat capacity of various thermal barrier materials

The experimental data shown in Figure 4.4 correlate with temperature T (in Kelvin) via a quadratic fitting function: $C = \alpha T^2 + \beta T + \gamma$, where α, β, and γ are constants and C is specific heat capacity in J/kg K. The values of the constants for the various thermal barrier materials examined in this study are shown in Table 4.1.

With the specific heat capacity established, the densities of the various materials were determined, see Table 4.1, thus allowing the calculation of their volumetric heat capacities. The resulting data are then used in conjunction with the property determination experimental tests (described earlier) to estimate the thermal conductivity.

Table 4.1: Correlation coefficients for heat capacity and thermal conductivity data (valid for: C, $295\,\mathrm{K} \le T \le 470\,\mathrm{K}$; λ, $295\,\mathrm{K} \le T \le 345\,\mathrm{K}$)

Material ID	Density (kg/m^3)	C (J/kg K)			λ (W/m K)		
		α ($J/kg\,K^3$)	β ($J/kg\,K^2$)	γ (J/kg K)	α (W/mK^3)	β (W/mK^2)	γ (W/mK)
gf	39.5264	-0.0044	5.0564	-110.03	1.58E-5	-9.55E-3	1.5188
gffs	38.3096	-0.0027	4.2325	89.052	3.28E-5	-0.0197	3.0292
rb	1729.08	-0.0055	6.4031	-309.43	0	3.59E-4	0.3380
kaow	96.1108	-0.0049	5.2371	-276.79	0	1.16E-4	-8.67E-3
carp	93.2401	0.0061	0.1786	914.94			
ssins		-0.0047	4.9731	261.10			

The key to the material ID are as follows (material thickness appended in parenthesis):

gf Fiber glass mat, no facing scrim (1.96 cm)
gffs Fiber glass mat with polyester facing scrims (1.87 cm)
rb Rubber, used between two fiber glass layers in Cadillac sound blanket (0.14 cm)
kaow Kaowool ceramic fiber, product of K Corporation (2.0 cm)
carp Carpet material (0.6 cm)
ssins MgO insulation

pro

sh

pro

Th

est

su

are

sig

ba

fa

in

(b

th

m

re

te

te

co

i.

In order to confirm that this singular estimation of the thermal conductivity produces accurate results, the sequential estimates from two different tests are plotted as shown in Figure 4.5. It can be seen that the experiment is good since the estimates progressively leveled out and finally have constant values over the second half of the test. This means that by the time all the available transient temperature data are utilized, the estimates of the thermal properties have been fully established. The same conclusion is supported by the nature of the normalized residuals plotted in Figure 4.6. The residuals are small, less than 1.5% for most times, and appear to be nearly random in nature. This signifies that the estimated thermal properties are close to the unknown true values.

The variation of the thermal conductivity with temperature for the various thermal barrier materials are shown in Figure 4.7. As can be seen from the plots, the addition of facing polyester scrims to glass fiber mats not only increases the values of λ but also increases the rate at which λ varies with temperature. Whereas the value of λ for the (bare) glass fiber mat increases by about 25% only with a 50 degree rise in temperature, the corresponding increase for glass fiber mat with polyester scrims is about 90%. This means that thermal effectiveness of the two materials may differ quite significantly. The results also show that the conductivity of rubber is approximately independent of temperature while that of the ceramic fiber increases slightly and linearly with temperature. Of all the materials examined, the rubber layer has the highest values of λ.

In the temperature range $295\,\mathrm{K} \le T \le 345\,\mathrm{K}$ covered in the tests, the thermal conductivity data also correlates well with temperature through a quadratic function: $\lambda = \alpha T^2 + \beta T + \gamma$. The values of the constants α, β, and γ are as shown in Table 4.1.

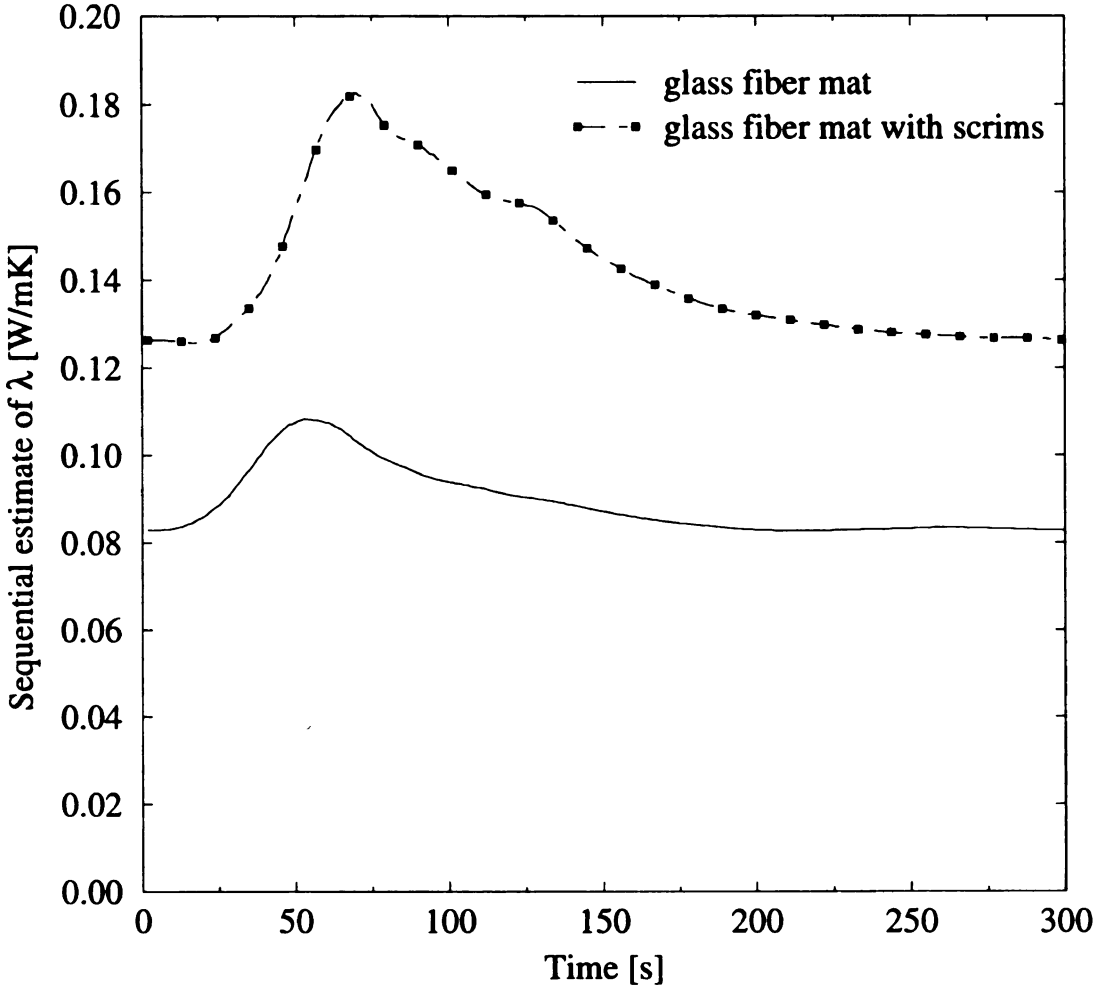

Figure 4.5: Sequential parameter estimates of λ for glass fiber mat and glass fiber mat with facing polyester scrims

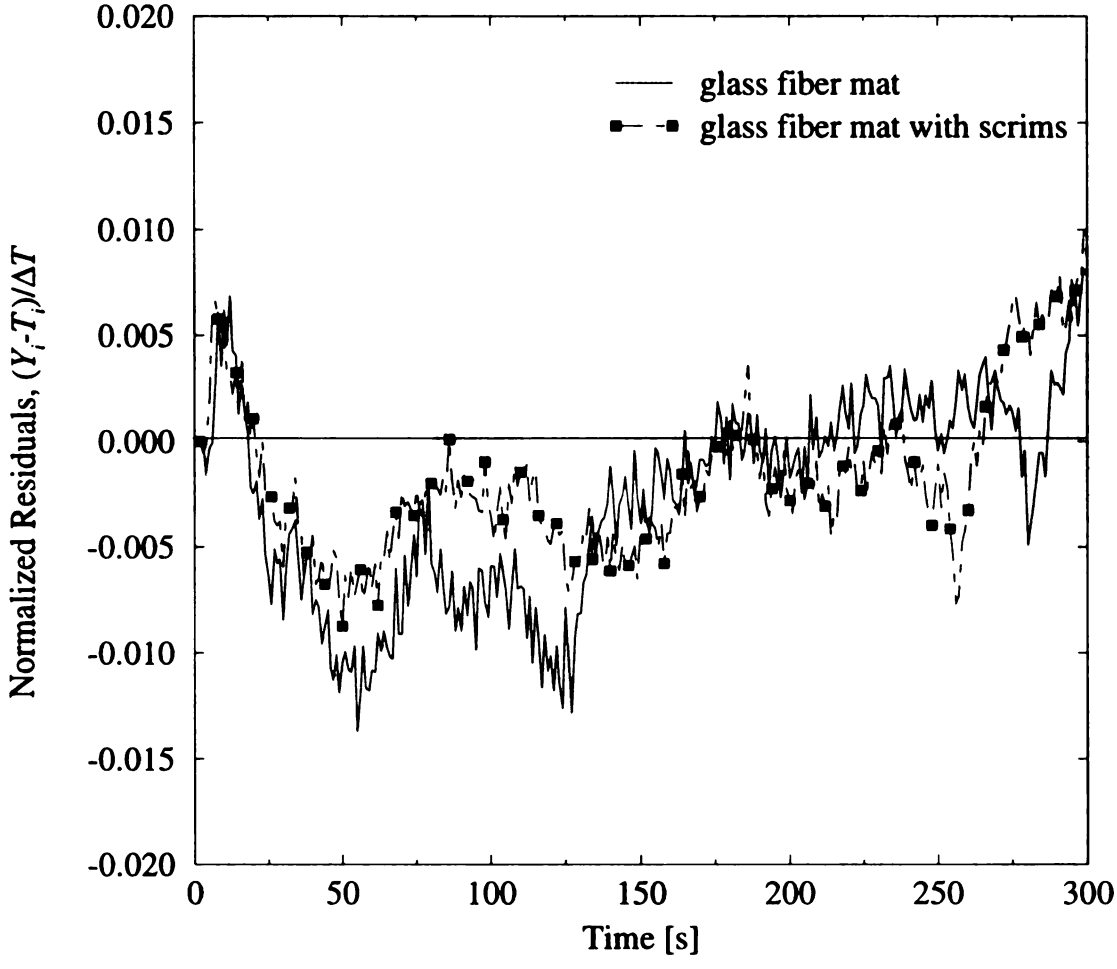

Figure 4.6: Trend of normalized residuals for tests on thermal barriers

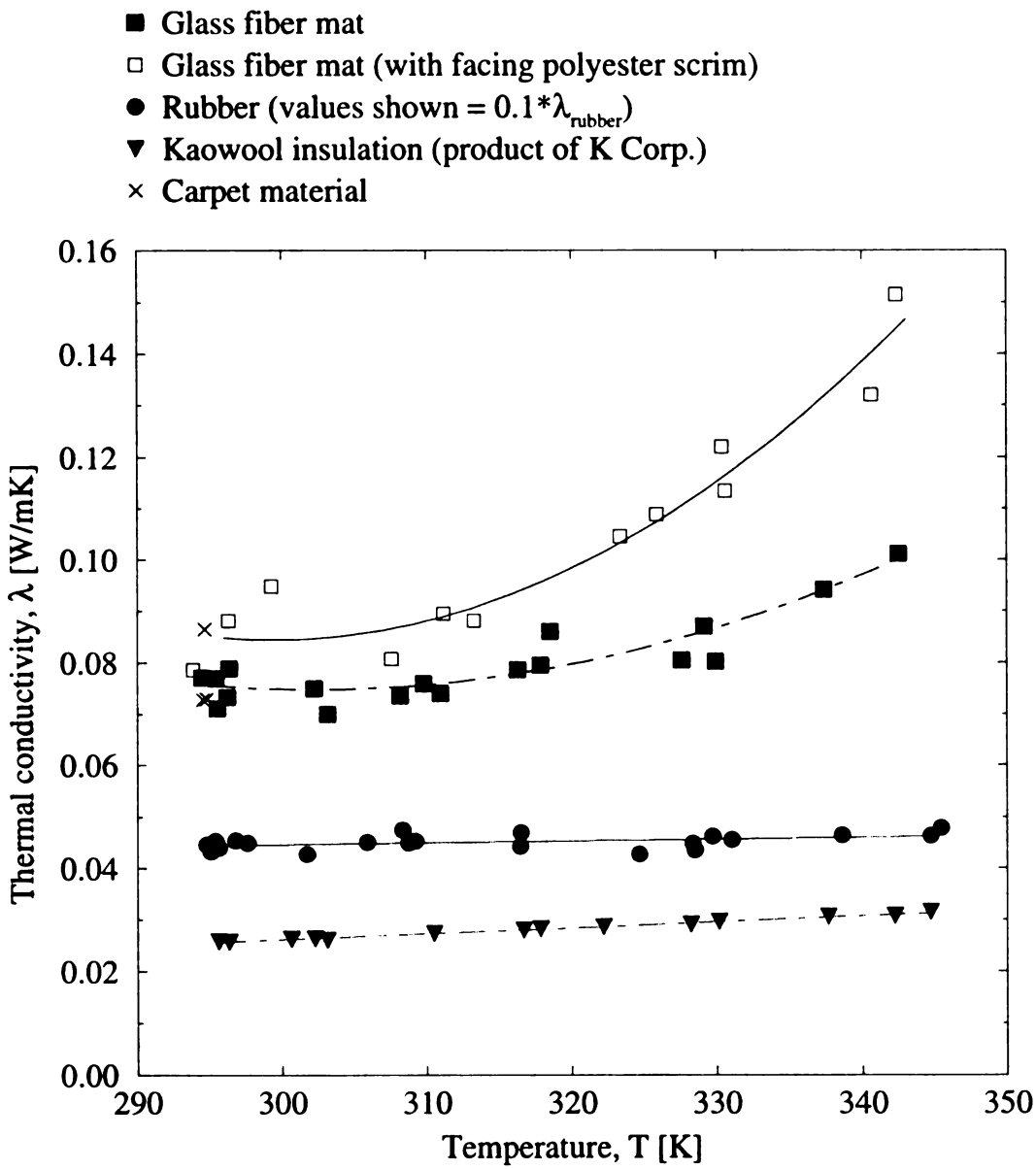

Figure 4.7: Thermal conductivity of some thermal barrier materials. (Note: To obtain the values of λ for rubber, multiply the values read on this graph by a factor of 10)

4.5 Numerical Simulation of Effectiveness of the Thermal Barrier

In this section of the work, the thermal properties measured in the previous sections and the experimental data from GM were to be utilized in numerical codes to investigate the influence of each material layer forming the thermal barrier. As shown in Figure 4.8, the bulkhead assembly is considered as a layered material of overall thickness L with known thermophysical properties. Given the heat flux, $q_A(t)$, and the temperature history, $T_A(t)$, on the engine side, the goal is to calculate the heat flux, $q_B(t)$, into the passenger side or the temperature, $T_B(t)$.

Comparing the arrangement in Figure 4.8 with Figure 4.1, material 1 is the sound blanket, 2 the steel bulkhead layer and 3 the dash blanket. Since the experiments at GM were conducted without the dash blanket and there was a lack of well-controlled measurements at the back of the steel wall to constitute suitable boundary conditions at that location, the heat conduction analysis for the sound blanket was conducted separately in this study with the interface conditions between materials 1 and 2 of Figure 4.8 used as the boundary conditions at $x = L$ where L is now L_1.

There were some questions regarding the accuracy of the experimental data from GM and hence, the extent to which they can be used in the numerical simulations of this section. Some of the problems can be associated with the difficulties of accurately measuring the heat flux through the glass fiber mats with heat flux gages, the problems of obtaining good contacts between the thermocouple beads and the insulation material, and the reliability of using halogen lamps as the source of heat. In spite of these problems, however, one of the better test results have been used as the basis for these simulations in

order to indicate the methodology and to make approximate deductions regarding the effectiveness of the various materials examined.

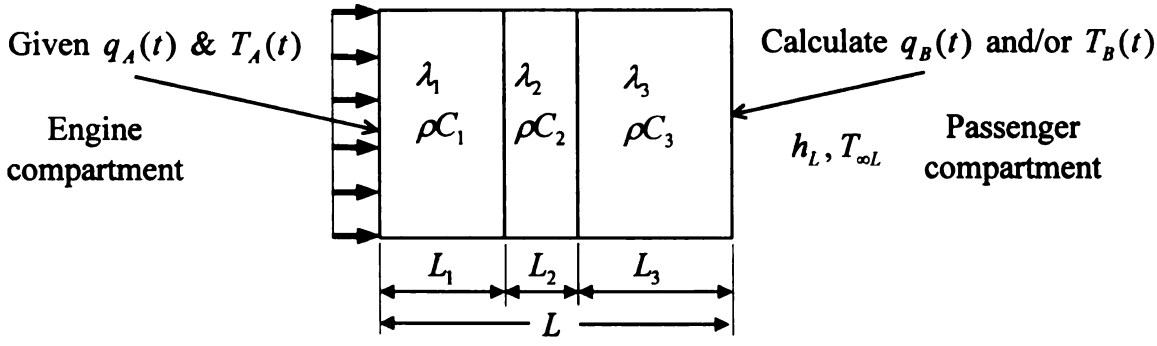

Figure 4.8: Problem description for the numerical model

The plot of the transient response of the glass fiber mat with facing scrims, as obtained from the GM experiments are shown in Figure 4.9. Thermocouples labeled as X, Y, and Z are located at the front, middle, and back surface of the insulation material, respectively. Those indicated as K1, K2, and K3 are intrinsic thermocouples on the front surface of the steel plate while K4 to K6 are also intrinsic and are on the back surface of the plate. The steady state value of the measured heat flux was about 85 kW/m^2. It was reported that the front scrim exposed to direct heat from the lamp rapidly burnt off. Since our interest should be the onset of ignition and subsequent burning of the material, only the transient part is needed here. We also see that the temperature at the front surface of the steel wall does not rise appreciably until after about 75s, hence a constant temperature boundary condition is imposed at the back of the insulation in numerical computations carried out over the first 90s.

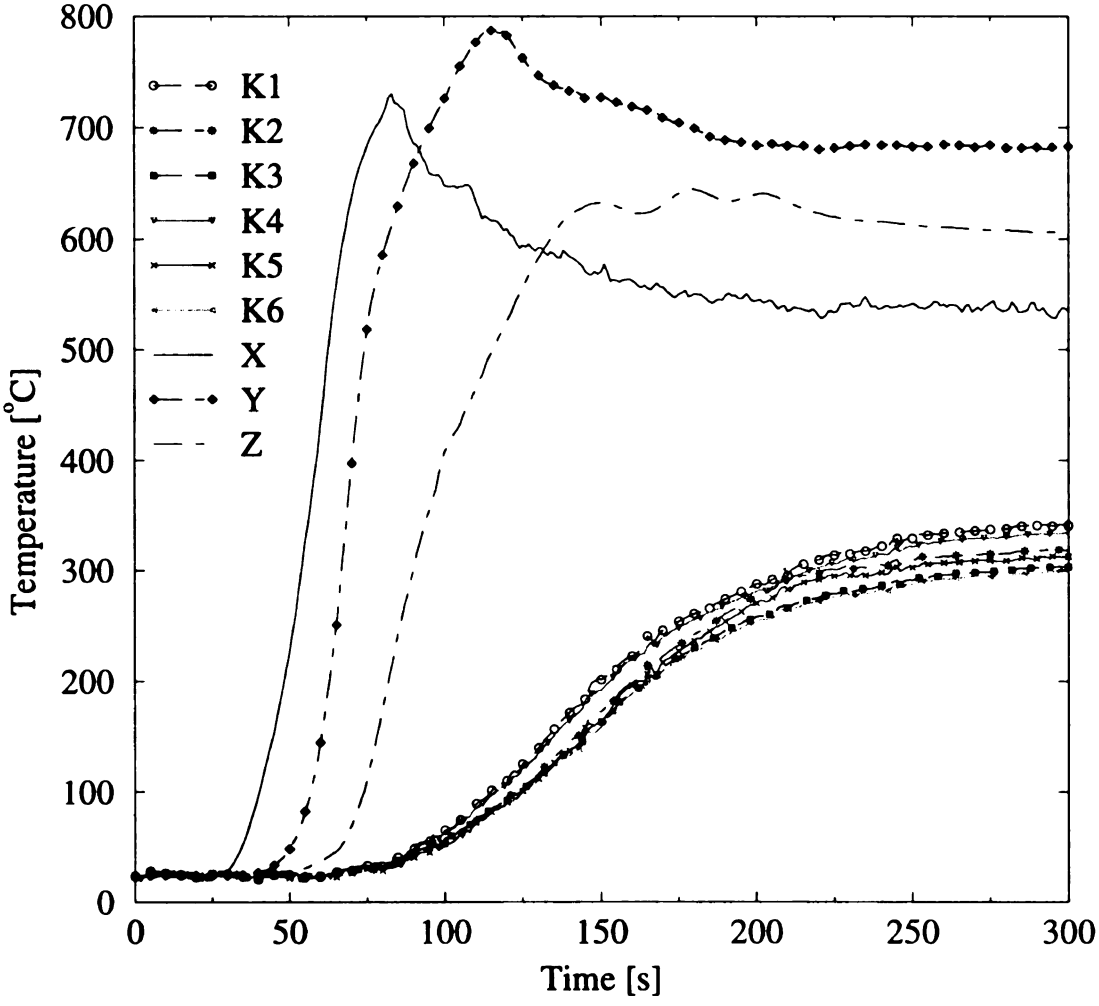

Figure 4.9: Temperature profiles from a GM test on glass fiber layer covered on both ends with polyester scrims

Using the transient heat flux data as inputs and taking the average readings of K1, K2, and K3 as $T_B(t)$, the temperature profiles at various locations inside the insulation material are calculated using the program "PROP1DR." The results, see Figure 4.10, show similar qualitative trends with the experimental data. It can be seen that half of the thickness of the insulation will be burning after a period of just one minute. It can be speculated that the differences between the numerical and the experimental results are due to the measurement problems stated earlier and to possible changes in the values of the thermal properties that may be associated with burning of the insulation.

Similar computations were done using the data for the other materials and the results are plotted in Figure 4.11. In the figure, the figure "0" refers to the front surface exposed to the external heat flux and "1/2" represents the surface half the thickness away. The results show that, at any given time, the largest reduction in temperature across the material occurs with the Kaowool ceramic fiber. The magnitude of the reduction suggests that while the front surface of the Kaowool may be exposed to a burning flame, the fire does not spread towards the passenger compartment. Its performance when used for insulation purposes in the flame spread experiments that are described in chapter 5 also confirm that the Kaowool material supports zero flame spread. Hence, where feasible, it may be a superior candidate for a thermal barrier material.

Finally, the case of a multi-layer thermal barrier wall, as is the case in the Cadillac sound blanket, was investigated. The computed temperature profiles at the interface between the materials are shown in Figure 4.12. The results show that while this

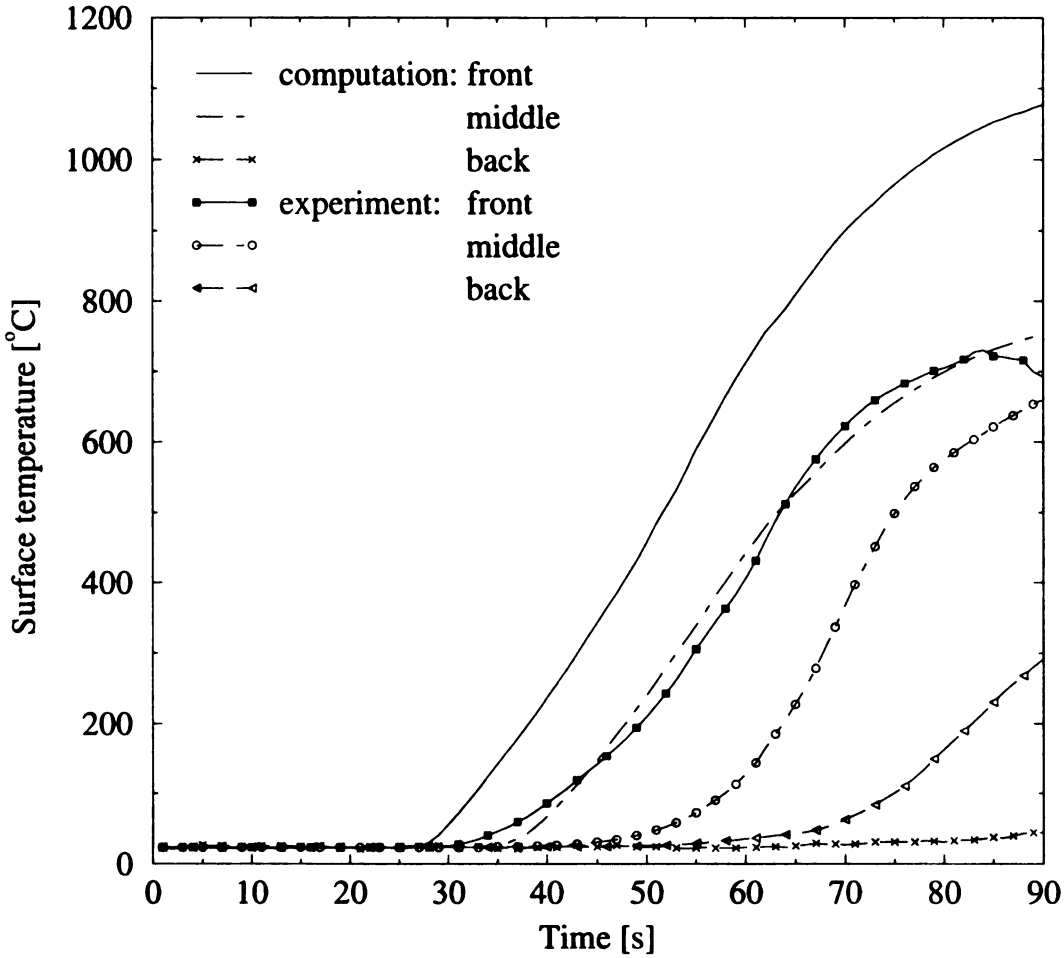

Figure 4.10: Thermal effectiveness of fiber glass with polyester scrims

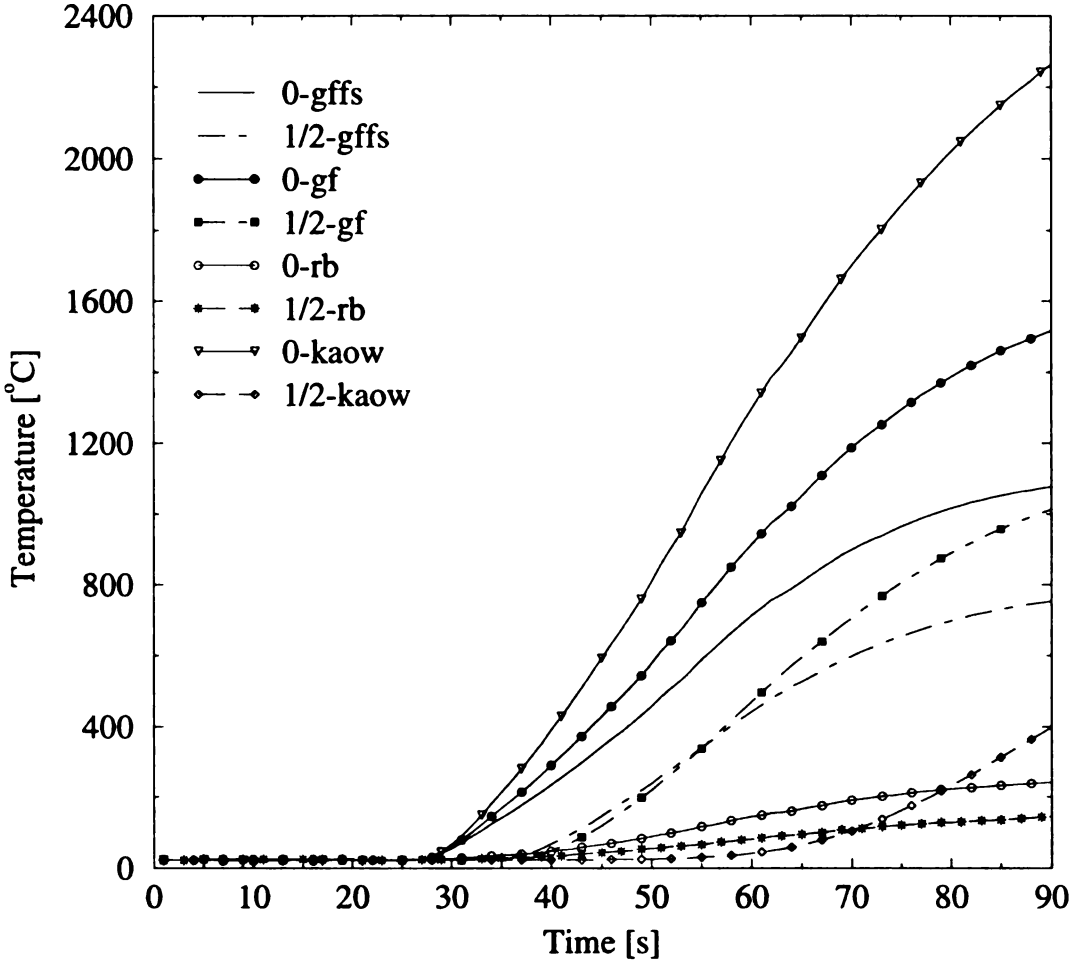

Figure 4.11: Effectiveness of various thermal barrier materials

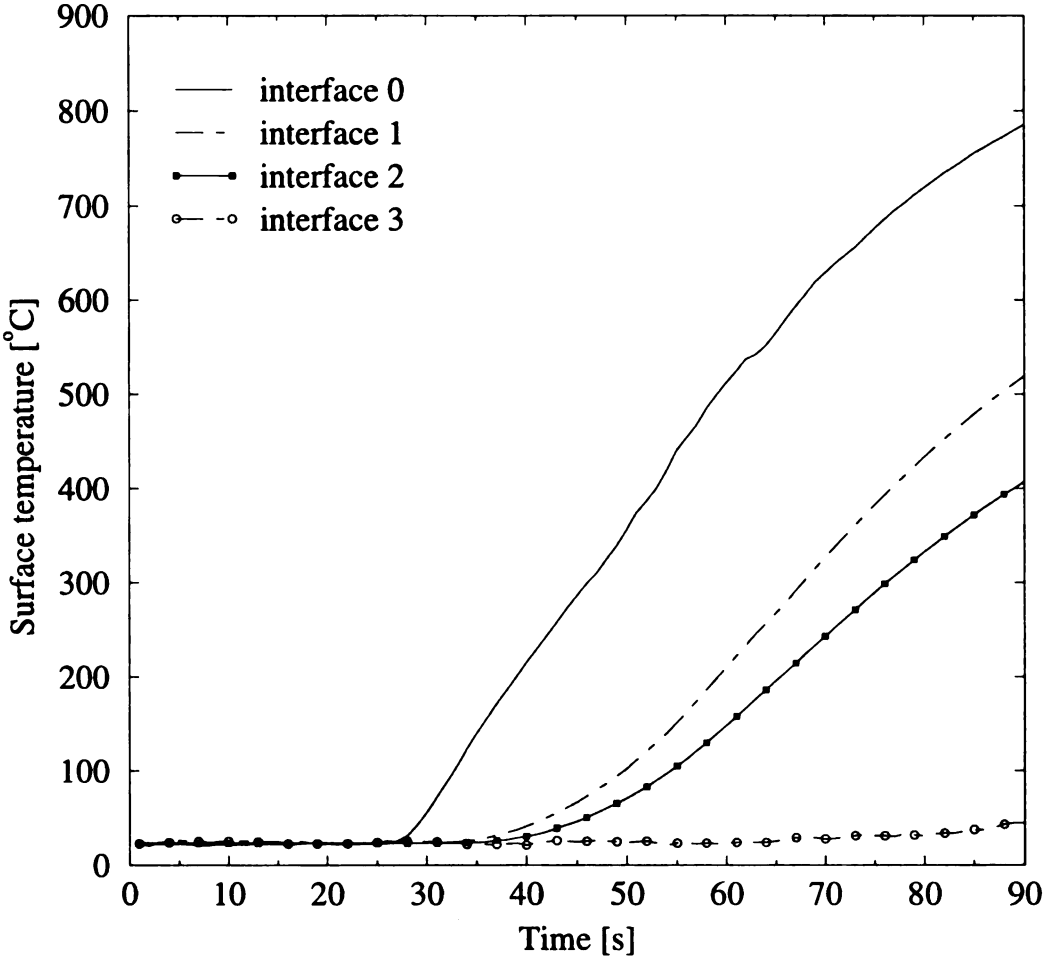

Figure 4.12: Thermal response of the Cadillac layered sound blanket

layered combination may be more effective than the individual glass fiber-based materials, it is still less effective than the Kaowool ceramic fiber.

4.6 Conclusions

The effectiveness of various proprietary sound blanket materials as thermal barriers were examined in this chapter. The thermal properties of the materials were determined using the DSC equipment and the experimental tests described in chapter 3. The results were correlated with temperature and the correlation coefficients established.

The results show that the addition of thin polyester scrims to the glass fiber layer increases the thermal properties slightly, but more importantly, increases the rate at which the thermal conductivity changes with temperature. The results of numerical calculations, using heat flux data from GM as inputs, suggest that the ceramic fiber may be the most effective as a thermal barrier in comparison to the other materials examined in this study or the layered glass fiber-rubber combination employed in the Cadillac sound blanket.

CHAPTER 5

EXPERIMENTAL STUDY AND MODELING OF OPPOSED FLOW FLAME SPREAD

5.1 General

In this chapter, the results of experimental investigation and modeling of opposed flow flame spread over the wood fiber/HDPE composite material are presented. As stated in chapter 1, the objective of this aspect of the study is to utilize the burning properties of the composites to assess their fire safety characteristics. Experimental tests and modeling efforts are combined to establish the influences of thermal property variation, gravity, and finite rate chemistry on the rate of flame spread over the composites.

5.2 Background and Approach

For downward flame spread in which the opposed flow is mainly buoyancy-induced, the rate of spread over thermally thick samples can be expressed as [42]:

$$u_f = \kappa \left[g_x \alpha_g \left(\frac{T_{f_d} - T_\infty}{T_\infty} \right) \right]^{1/3} \frac{\lambda_g \rho_g C_{p_g}}{\lambda_s \rho_s C_s} \left(\frac{T_f - T_v}{T_v - T_\infty} \right)^m \tag{5.1}$$

where, α_g is the thermal diffusivity of the gas, g_x, the component of gravity in the direction of spread, T_f, the flame temperature with sub-subscript d expressing conditions with dissociation effects, T_v, the constant gasification temperature, and T_∞, the ambient temperature. It can be taken that $\left[g_x \alpha_g \left(T_{f_d} - T_\infty \right) / T_\infty \right]^{1/3} \sim u_g$, where the constant of the proportionality is contained in the multiplicative factor κ. Hence, $\kappa = \kappa_\infty$

for the heat transfer model (infinite rate chemistry), and $\kappa = \kappa(\beta, D)$ for chemistry-dominated flame spread process. The symbols β and D respectively represent the activation energy and the Damköhler number.

There have been several suggestions for the index m of equation 5.1. A theoretical analysis, based on the heat transfer model, and employing the Oseen flow approximation, leads to $m = 2$ [5]. A recent numerical simulation by Wichman and Osman [59] which employed the shear flow approximation confirmed that $m = 2$ within 0.1% deviation even for non-Oseen flows. These results suggest that the value of m does not depend on the controlling physical mechanism of the spread process, whereby $m = 2$ for both the heat transfer and the finite rate chemistry dominated flame spread. This implies that in the case where finite rate chemistry dominates, its effect is contained solely in the multiplicative factor κ.

We have seen in the preceding chapters that the rate of flame spread over thermally thick fuels is influenced by several factors including, material property variation, gravity, and finite rate chemistry. The approach taken in this study is to use various experimental data to *extract* the contributions of gravity, material property, and finite rate chemistry one after the other. Consequent to this approach, the expression for flame spread rate can be written simply as a product of various functional effects in the form:

$$u_f = f_1(u_g) \cdot f_2(properties) \cdot f_3(enthalpy) \cdot f_4(finite\ chemistry) \cdots\cdots \qquad (5.2)$$

The correlation of u_f with u_g (for forced opposed flow) or u_f with g_x (for buoyancy-induced flow) can produce the form of f_1, for instance. An improved understanding of

f_2 can be achieved by correlating flame spread rates with fuel properties which in turn have been correlated with temperature. The other factors can be extracted following similar arguments. In this way, the form of the chemistry factor κ, which is identical to the function f_4, can be deduced.

5.3 EXPERIMENT

5.3.1 Combustion Chamber Design

The combustion chamber is designed to meet four major requirements as follows:

- The height of the chamber is to be adjustable so as to position the samples at sufficient depth from the top of the chamber to disallow any inflow through the open top from influencing the flame spread process.
- There must be means of observing the flame while in progress and of using optical devices to observe or record the flow field and the flame.
- Possibility to use the chamber to study both opposed-flow and wind-aided flame spreads although only opposed flow flame spread is studied at this time.
- Existence of minimal or no protruding objects, including thermocouples leads, that can disturb the flow field *seen* by the flame.

With these requirements in mind, the combustion chamber, whose component parts are shown in Figure 5.1, was designed and fabricated. The chamber consists of two parts, the base assembly and the combustor walls (sides). The base assemble has a base plate measuring 11.67" by 11.67" in cross section and four side walls that are 6" in height. The plates are welded together at the edges to form a open-top box that is 11.67" by 11.67" in

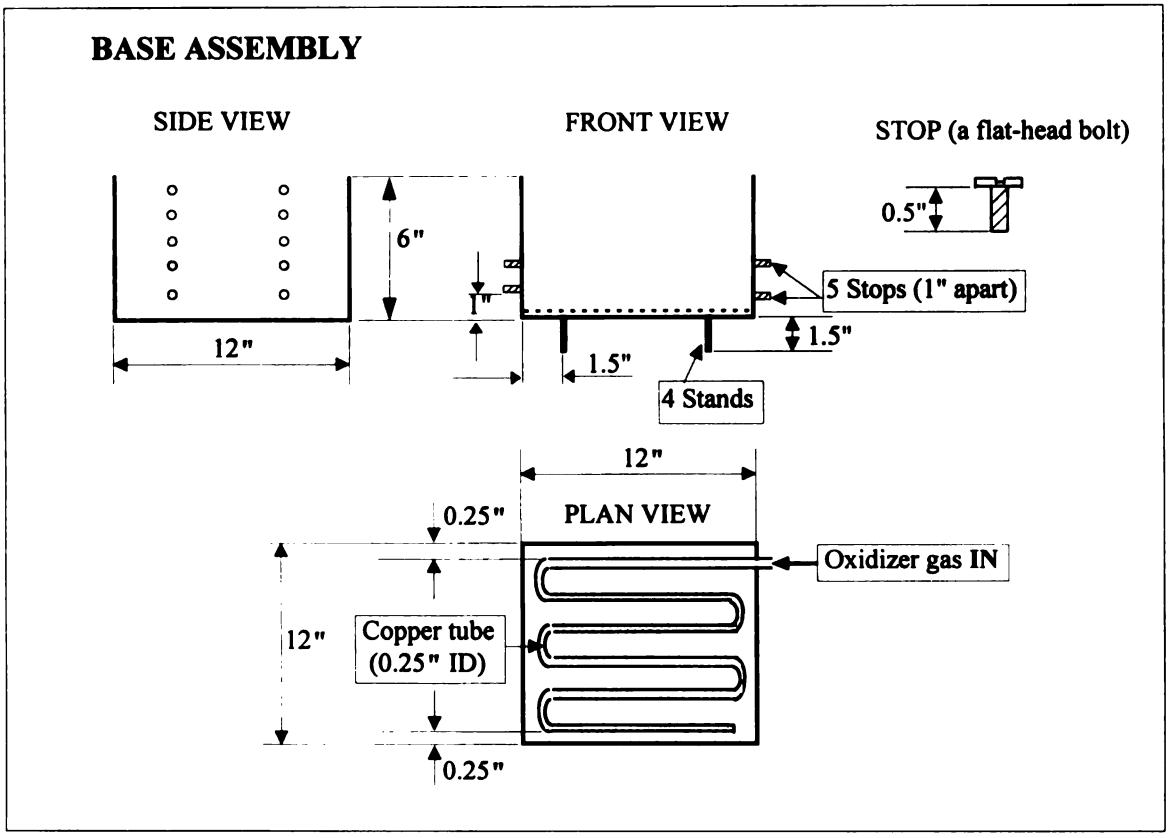

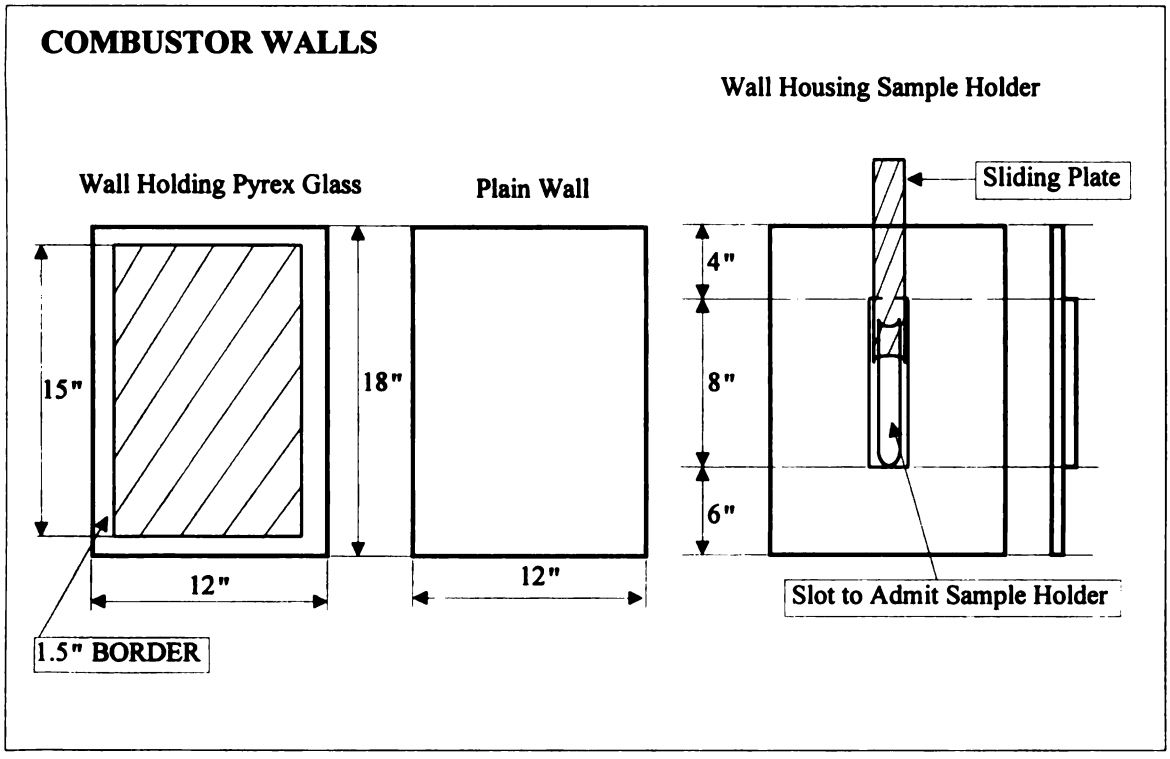

Not drawn to scale

Figure 5.1: Component Drawings of the Combustion Chamber

cross section at the base and 6" tall. The combustor walls are attached to the base assembly by sliding the side walls until the appropriate hole on the side wall is lined with the one on the same side of the base assembly. A stopper is then passed through the holes and tightened securely. By choosing holes at various heights on the base assembly to which those on the combustor walls are lined, the height of the resulting chamber can be adjusted to a maximum of 24".

5.3.2 Flame Spread Experimental Set-Up

A schematic of the full experimental set-up is shown in Figure 5.2. The walls of the chamber were fabricated from aluminum plates. Two of the side walls are made of pyrex glass to enable the observation of the flame spread while in progress and to allow the possible future use of a camera or laser diagnostic equipment to measure the rate of spread over the samples. The gas flow is introduced into the chamber through a copper tube positioned on the base and on which small holes are drilled at intervals (see Figure 5.1). The tube is placed such that the holes face down and the incoming gas thus flows onto the floor of the chamber and from there spread out. Two layers of iron mesh are positioned over the copper tube, followed by a 1" height layer of glass beads and, finally, another three layers of iron mesh on top of the glass beads to ensure that the gas flow is sufficiently straightened.

Two flow meters are used for metering the flow of oxygen and nitrogen in the desired concentration ratios. The flow is passed through a constant temperature bath prior to the flow meters to maintain the gas at approximately room temperature. The volumetric flow rate of the gas entering the chamber (O_2+N_2) was approximately 2.636 liters/s for all

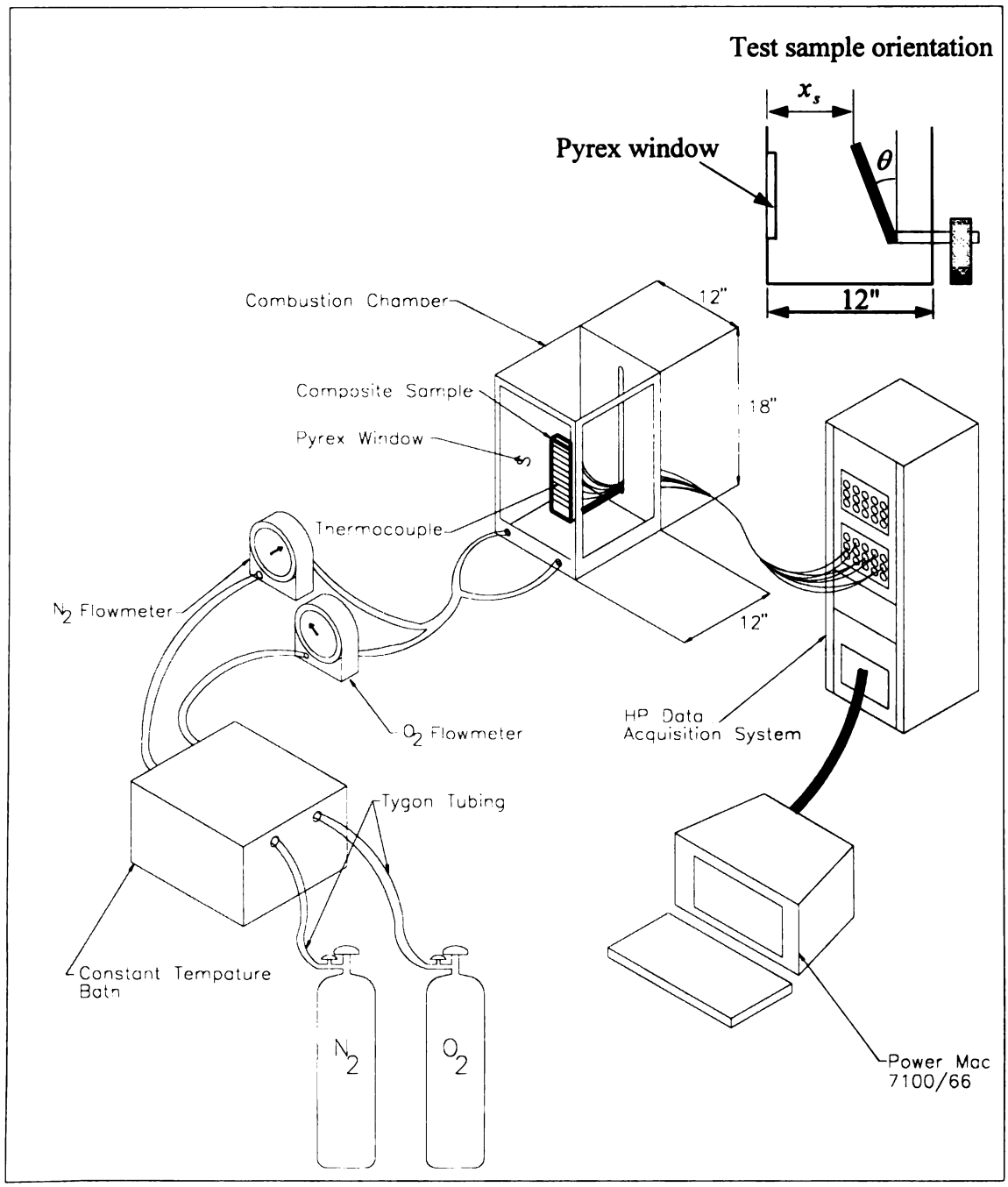

Figure 5.2: Schematic of the flame spread experimental set-up

tests which corresponds to a flow velocity, u_∞ of 3 cm/s. Since this is small compared to typical induced buoyant velocity, $u_b \sim 30$ cm/s, the flow field inside the chamber can be considered essentially buoyancy-driven.

The sample holder is designed such that it is capable of holding the sample at various vertical heights above the base of the chamber and at different angles of inclination, θ about the vertical axis. By changing the edge of the sample at which the flame is initiated, both opposed-flow and wind-aided flame spread can be studied in the apparatus, although, as mentioned earlier, only the opposed flow problem is investigated in this dissertation.

5.3.3 Measurement of Flame Spread Rate

The composite samples for flame spread test are 15 cm long, 5 cm wide, and 1.27 cm thick. In the analytical work of deRis [5] and West et al. [60], the expression for the minimum thickness, L_c above which the sample can be considered thermally thick was given as:

$$L_c = \frac{\lambda_{sy}}{\lambda_g}\frac{\alpha_g}{u_\infty}\left(\frac{T_v - T_\infty}{T_f - T_v}\right) \tag{5.3}$$

where, λ_{sy} is the component of thermal conductivity of the solid in the transverse direction, i.e. perpendicular to the direction of flame spread, as described in detail in chapter 3. All other symbols in equation 5.3 are as defined in chapter 2.

To obtain an estimate for L_c, the maximum measured value of the composite thermal conductivity as given in chapter 3 can be used leading to $\lambda_{sy} \cong 0.55$ W/mK. Also, since L_c is inversely proportional to $(T_f - T_v)$, and hence to T_f, the maximum value of L_c that

must be exceeded in order to have thermally thick samples will correspond to the minimum value of T_f. Assuming that flame spread over the composite can be supported at oxygen mass fraction as low as 10%, correlation of the T_f - Y_O data of reference 61 produces $T_f = 1382.9$ °C at $Y_O = 0.1$. A reasonable value of T_v, as will be shown later in section 5.4, is 543.5 °C. Evaluation of the relevant gas properties gives $\lambda_g = 87.1 \times 10^{-3}$ W/mK and $\alpha_g = 262 \times 10^{-6}$ m^2/s. Substitution of these values in equation 5.3 and taking $u_\infty = 30$ cm/s (the order of magnitude of the buoyancy-induced opposed flow velocity) leads to $L_c = 0.5816$ cm. Hence, it can be concluded that the thickness 1.27 cm ensures that the composite samples can be considered thermally thick for the duration of the test.

In order to measure the spread rate over the samples, the temperature history at successive lines marked perpendicular to the direction of spread and spaced 1.905 cm apart are obtained using thermocouples located on those lines. The thermocouples are held in place by first making a shallow, angular knife-cut through the sample, embedding the 0.0127 cm diameter, type K thermocouple wire in the crack and then pressing the crack closed. Kaowool insulation is attached to the back and side surfaces of the sample leaving only the front surface over which flame spread is to be tested. The thermocouples are connected to the Omega HP-3852A Data Acquisition system which is used to acquire the temperature-time data. The acquisition system is controlled by a Power Macintosh 7100/66 computer via the NB-DMA 2800 Data Acquisition board.

The transient temperature measurements are used to deduce the time of flame arrival at each thermocouple location. Typical transient readings of the thermocouples are shown in Figure 5.3. The sixth thermocouple was faulty and registered bad readings

which have been left out of the figure. Noting that the temperature at each location rises almost instantaneously due to the presence of the flame, the time of flame arrival can be taken to correspond to the point of maximum temperature gradient, obtained by plotting the derivative of the temperature response at each location with time.

However, one problem with this method of determining flame spread rates over the composites is that sometimes a thermocouple can detach from the fuel surface (or burn out entirely at the joint) after the flame has reached its location. In such cases, the thermocouple will record the gas temperature (or the default "open" instrument value of $\pm 1.0 \times 10^{38}$ to indicate discontinuity in the thermocouple circuit) rather than the solid surface temperature. Under such conditions, the time associated with the maximum temperature gradient may not represent the time of flame arrival.

To alleviate this problem, the flame arrival criterion described above was modified. The time associated with maximum temperature gradient in the interval $35°C \leq T \leq 250°C$ at a given thermocouple location is chosen as the flame arrival instant for that location. While the lower limit of $35°C$ was chosen so as to eliminate possible initial fluctuations prior to flame initiation, the use of $250°C$ as the upper limit was dictated by experimental observations of the surface temperature over a range of oxygen mass fraction, Y_O, using a hand-held thermocouple readout. This modification ensures that the results are insensitive to thermocouple detachment or breakage triggered at any location by the flame.

Other criteria for the flame arrival time, e.g., time of maximum temperature recorded, and time of maximum temperature gradient without any modification, were examined as well. Some initial tests, typifying both types of experiments planned, i.e. u_f - Y_O and u_f - θ

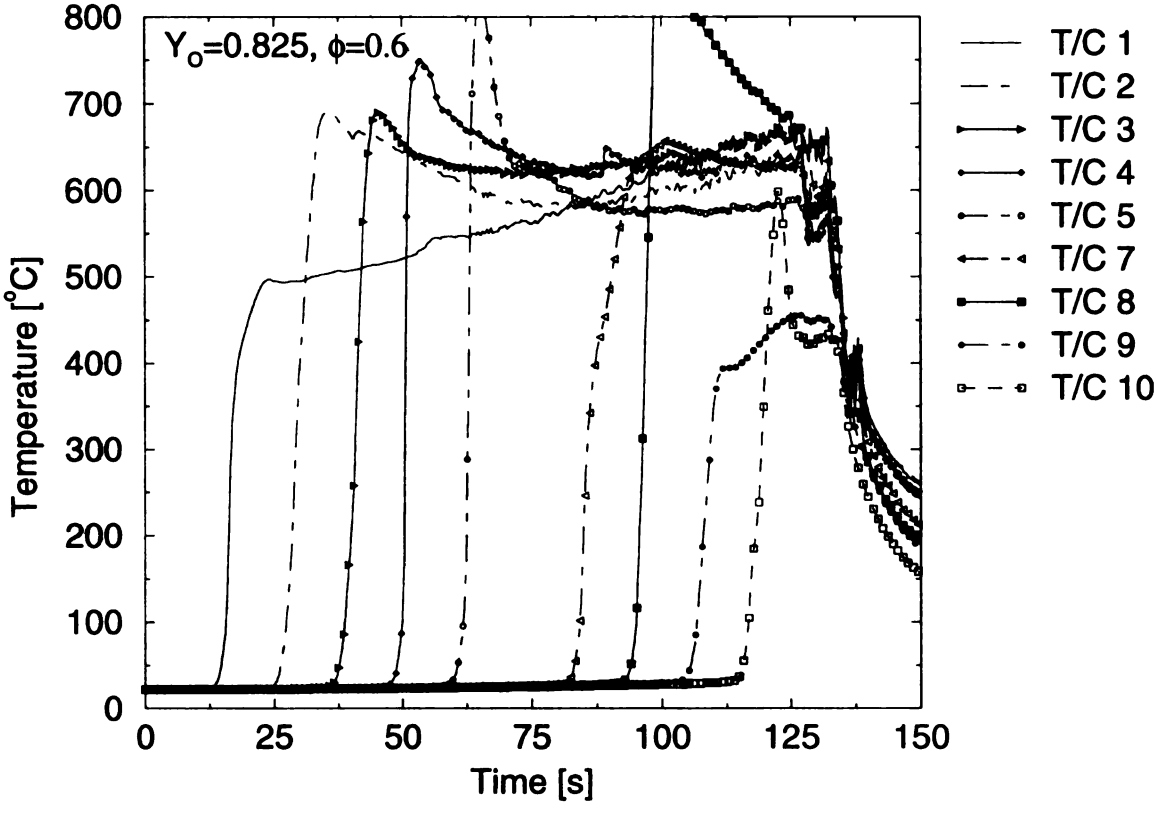

Figure 5.3: Typical temperature profiles recorded during flame spread test

measurements, were run. Flame spread rates obtained from these trial runs and using the various criteria were then compared to those obtained from visual timing of the flame travel using a stop watch. It was found that the criterion discussed above consistently produces the best results in terms of agreement with the stop-watch results.

To show the level of agreement between the thermocouple and the visual stop-watch method, a plot of flame spread rates obtained using both methods are shown in Figure 5.4. It can be seen from the figure that the results are practically identical for the variable Y_O tests and are within reasonable agreement for the gravity tests also. Quantitatively, the plots in Figure 5.5 show that the deviation of the thermocouple-based results from the stop-watch results, defined as $(u_{T/C} - u_{S/W}) / u_{S/W}$, are mostly within ±5 %.

The agreement between the visually-timed and the thermocouple-based results is very important since it establishes the reliability of the procedure adopted herein for measuring flame spread rates over the composites. It is well known that differentiation of experimental data can sometimes produce unsatisfactory results because of the propensity to magnify experimental errors. Fortunately, we see that such worry does not arise here as evidenced from the comparisons in Figures 5.4 and 5.5.

5.4 Results and Discussion

Previous studies on the wood fiber/HDPE composite suggest that the best mechanical properties are obtained when the wood fiber mass fraction is 40% [55]. This composition was thus selected as the starting point for the flame spread tests.

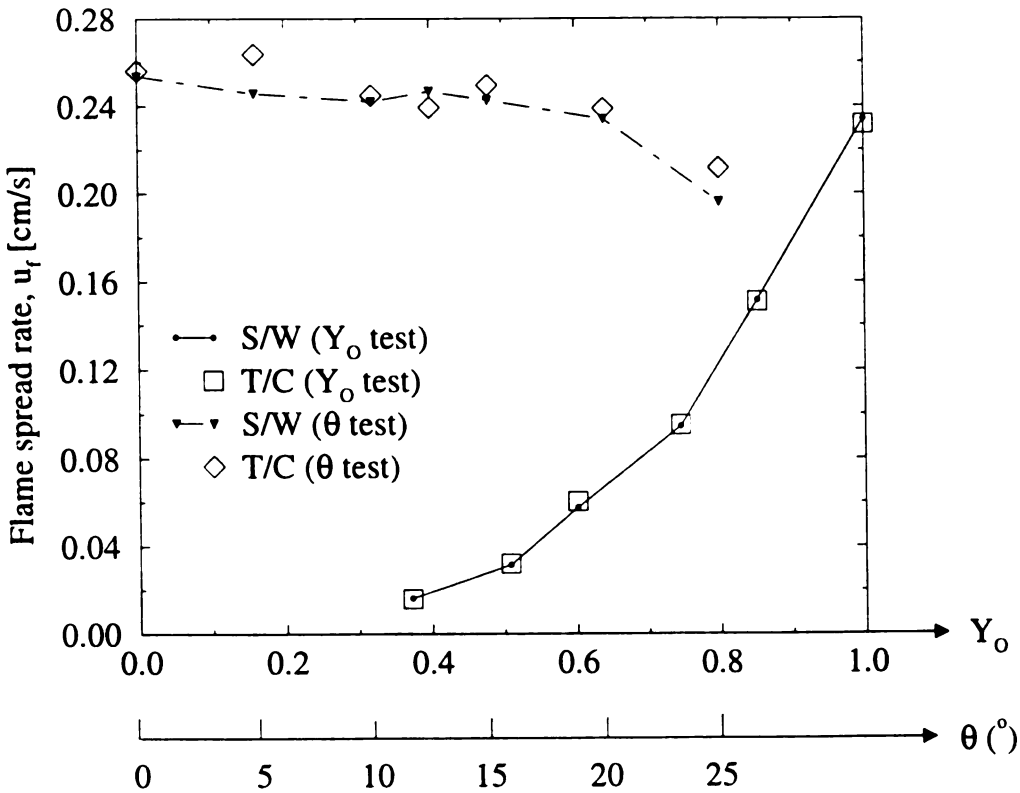

Figure 5.4: Comparison of flame spread rates obtained using thermocouples with those obtained by visually timing the flame with a stop-watch

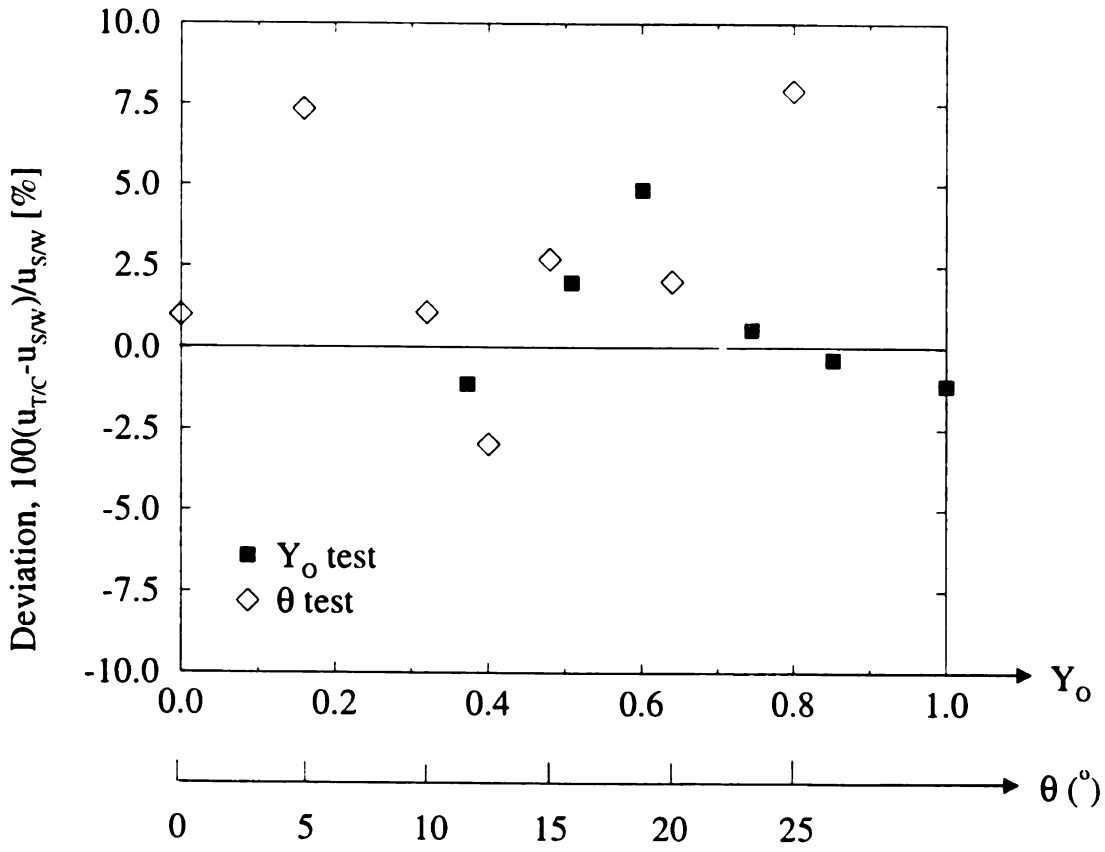

Figure 5.5: Deviation of thermocouple-based results from stop-watch results

The variation of the flame spread rate with inclination angle, θ, is shown in Figure 5.6. For the data at $Y_O = 1.0$, each point shown on the graph was established from an average of five or more measurements. A first look at the results shows a physically reasonable trend. The flame spread rate was highest when the sample is in the vertically upright position ($\theta = 0$) and decreases as the sample is tilted towards the horizontal position ($\theta = 90°$). However, a more discriminating choice of the graph scales, see the insert of Figure 5.6, reveals a somewhat local instability region around $\theta = 15°$ where the flame spread rate initially increases with θ, then reaches a local maximum, and subsequently decreases as θ is increased past this region. The variability of the spread rates, also plotted in Figure 5.6, were simply taken as the standard deviation of the data.

In trying to understand this local behavior, the experiments were repeated many times and the trend persisted. Simple flow visualization did not reveal any change of flow pattern about this inclination angle. The same experiments were then repeated for $Y_O = 0.9$ and, as seen in Figure 5.6, it was found that the variability with θ is greatest around 15° although not as pronounced as is the case of $Y_O = 1.0$.

One possible cause of this behavior is the formation of a separation bubble which may locate itself forward or behind the flame front at different inclination angles. A separation bubble which reattaches behind the flame front, for instance, will change the dynamics of the flame spread. It is possible to then locally produce "a wind-aided flame spread" as opposed to wind-opposed flame spread [12]. This is a speculation, however. Detailed, non-intrusive flow field measurements, which are beyond the means of this dissertation work, may be needed in order to explain this seemingly anomalous behavior.

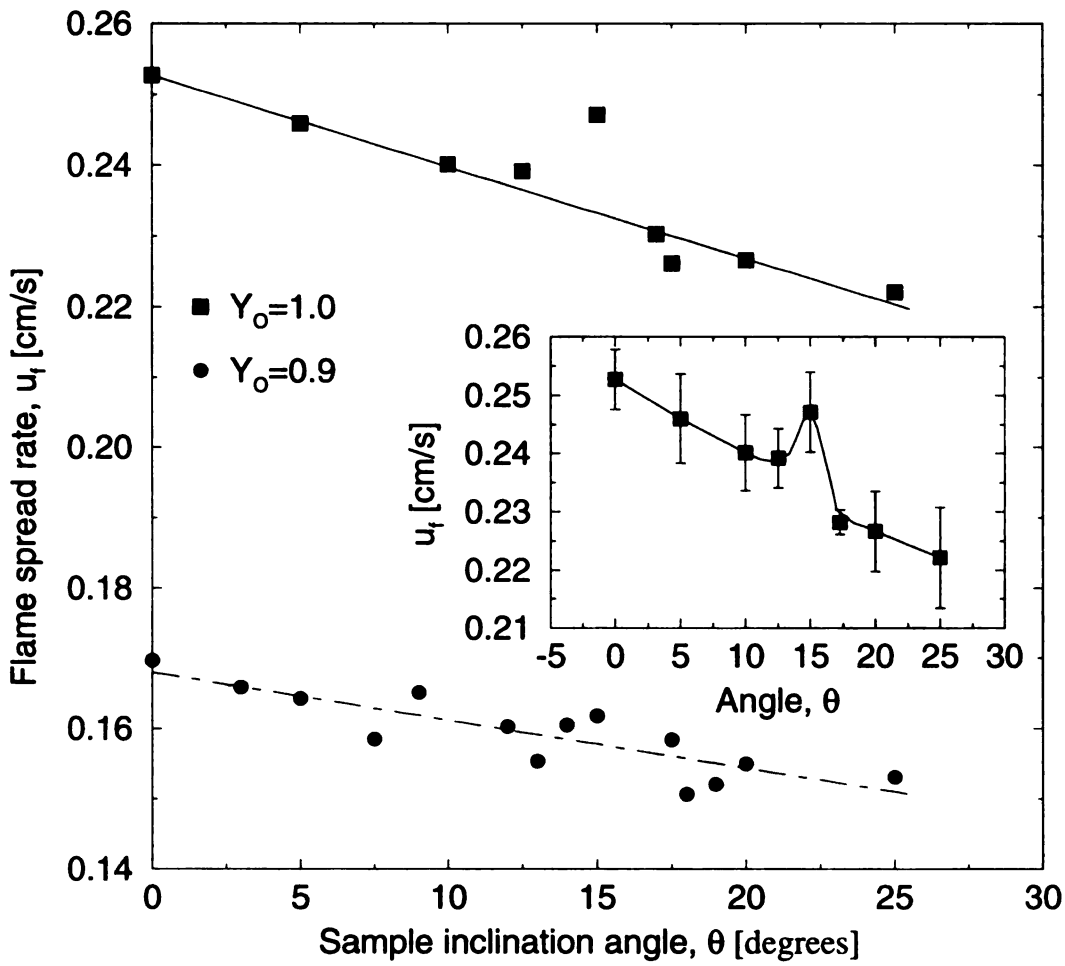

Figure 5.6: Plot of flame spread rate as a function of θ (insert shows variability of the spread rate data and the local instability region)

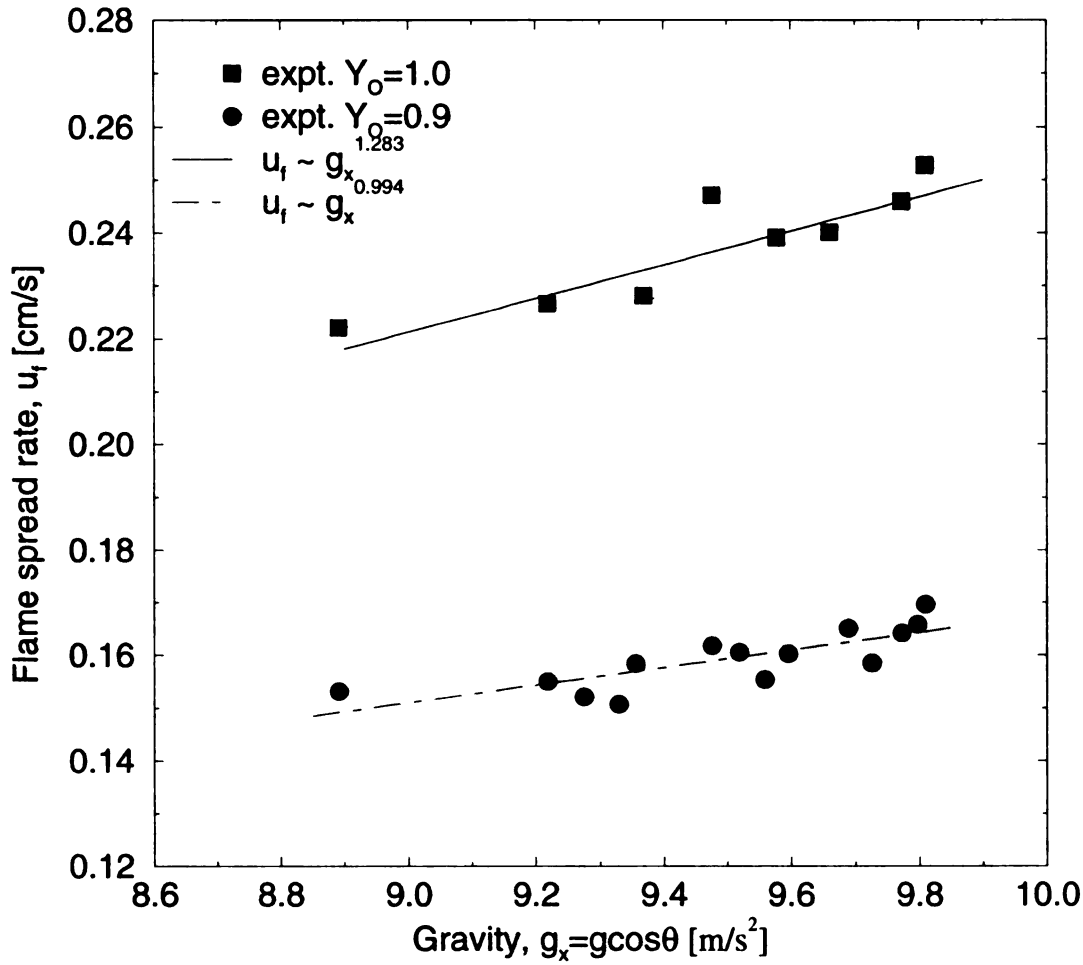

Figure 5.7: Influence of gravity on flame spread rate (note that $g_x = 9.81\cos\theta$)

5.4.1 Correlations Using Data for $\phi = 0.4$

The experimental data shown in Figure 5.7 can be correlated in the form $u_f \sim g_x^{\,c}$, where c is a constant. Excluding the data at 15° for reasons discussed earlier, the correlation leads to $c = 1.28$ for the data at $Y_O = 1.0$ and $c = 0.99$ for those at $Y_O = 0.9$. The curves representing these correlations are shown in Figure 5.7 as well. It has been suggested in the literature that the correlation at $Y_O = 1.0$ can be used to deduce the form of $f_1(u_g)$ [62]. It was explained that the rate of chemistry for the case $Y_O = 1.0$ is expected to be fast, and if ever infinite rate chemistry can be approached, this case should approximate it the best. It is understandable that the regime of finite rate chemistry dominance will depend on several factors, including u_g, Y_O, and material type. It was suggested in the study by Ray [36] that, for PMMA, heat transfer dominates the spread process in the u_g range where $\frac{du_f}{du_g} > 0$. The data published in [20] show that this condition is satisfied at u_g up to about 245 cm/s for the case $Y_O = 1.0$. Since the magnitude of the buoyancy-induced opposed velocity (which is about 30 cm/s) is within this range, it can be assumed that the measured spread rates at $Y_O = 1.0$ are governed primarily by heat transfer.

Examining the results of the correlation, it is noted that the dependency $u_f \sim g_x^{\,1.28}$ for the data at $Y_O = 1.0$ seems to be too strong compared to the theoretical prediction, $u_f \sim g_x^{\,1/3}$, at first glance. However, it is possible that the fuel surface temperature just ahead of the flame front may not be entirely independent of the sample inclination angle θ, hence of g_x. The interaction of the pyrolyzed mass flux and the induced opposed flow

may slow down the reaction, even though the reaction will still, in general, be fast. This may lower the flame temperature and, by extension, the solid fuel temperature in the vicinity of the flame front. Under such conditions, any variation of the solid thermal responsivity, $\lambda_s \rho_s C_s$ with temperature will influence the measured spread rates and must therefore be accounted for in the correlation.

To confirm whether there is any inter-relationship between composite temperature and sample orientation, the average sample surface temperatures associated with flame arrival at various locations are plotted as a function of sample inclination angle, θ as shown in Figure 5.8. It can be seen that the temperature does indeed decrease slightly (and linearly, too) with increase of θ. Again excluding the data around 15°, correlation of the data shows that $T_s \sim g_x^{0.79}$. This result is a manifestation that the flame front is located ahead of the pyrolysis front. As discussed in chapter 2, it is generally assumed that the solid fuel pyrolyzes at a constant temperature T_v which here will be expected to be invariant with inclination angle. In appendix A, where detailed decomposition study of the solid is undertaken, this assumption will be shown to be a reasonable one. Hence, such variation of solid temperature with sample inclination as in Figure 5.8 can only occur forward of the pyrolysis front.

In order to include this effect in the correlation of u_f with g_x, the variation of $\lambda_s \rho_s C_s$ with temperature is needed. For this purpose, we use the results of earlier experimental studies on the effective thermal properties of the composite. For the composite with $\phi = 0.4$ presently being considered, we see from Figure 3.8 of chapter 3 that $\lambda_s \rho_s C_s$ varies linearly with temperature.

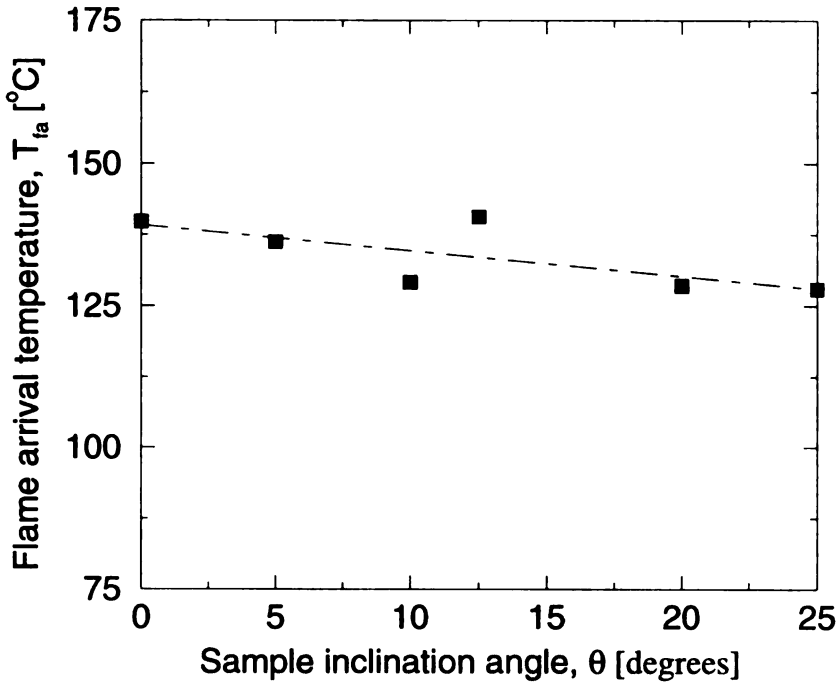

Figure 5.8: Variation of average flame arrival temperature with θ

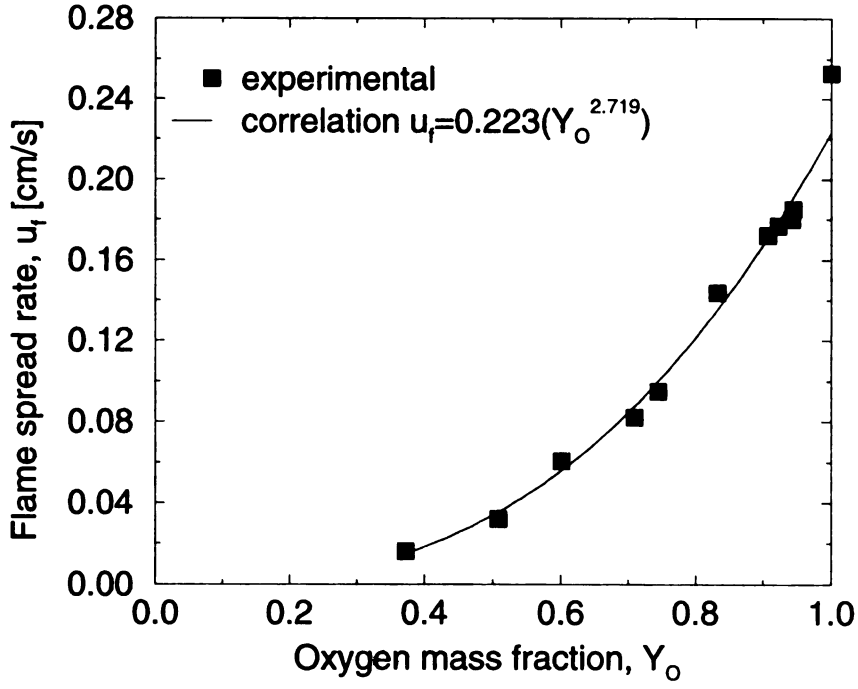

Figure 5.9: Variation of u_f with Y_O for $\phi = 0.4$

Assuming that $\lambda_s \rho_s C_s \sim T_s$, since $\lambda_s \rho_s C_s$ varies linearly with temperature (for $\phi = 0.4$), it follows that $\lambda_s \rho_s C_s \sim g_x^{0.79}$. We see from equation 5.1 that $u_f \sim (\lambda_s \rho_s C_s)^{-1}$. The overall u_f dependency on g_x is therefore, $u_f \sim g_x^{1.28} \cdot g_x^{-0.79}$, giving an overall index of 0.49 which is close to the theoretical prediction of 0.33. It can be concluded therefore that $f_1 \sim u_g \sim [g_x \alpha_g (T_c - T_\infty)/T_\infty]^{1/3}$, where T_c is a characteristic wall temperature taken in equation 5.1 as T_{f_d}, the flame temperature attained inclusive of dissociation effects [61].

Turning attention now to the influences of finite rate chemistry, the variation of flame spread rate with oxygen mass fraction, Y_O is plotted in Figure 5.9. The flame speed measurements were taken with the composite samples in the vertical position ($\theta = 0$). No external heat source to the flame was applied, so the flame spread process is purely self-sustaining.

One important qualitative result obtained is the fact that flame spread over the 40% wood fiber composite was not possible for $Y_O = 0.233$ (air). The flame quenched each time Y_O was lowered beyond a critical value following initial flame initiation at a higher value. This indicates that the composite behaves more like the wood content than the polymer matrix at this composition. It is well known that without background radiation or other external heat sources, downward or horizontal flame spread over wood in air is not possible; even upward flame spread requires background radiation in air [63].

The experimental data of Figure 5.9 correlate as $u_f \sim Y_O^{2.72}$. By using the earlier g_x-correlation and taking $m = 2$, these results can be substituted to predict the

dependency of the finite chemistry factor $\kappa(\beta, D)$ on Y_O. Starting with equation 5.1, it can be seen that $u_f \sim T_{f_d}^{1/3}$. Taking $T_{f_d} \sim T_f$, and since $T_f \sim Y_O$, it follows that $T_{f_d} \sim Y_O$. The overall Y_O-dependence thus becomes $u_f \sim Y_O^{1/3} \cdot Y_O^{2}$ giving a total index of 2.33. Comparing this with 2.72 obtained from the correlation of the experimental u_f - Y_O data, it can be concluded that $f_4 = \kappa(\beta, D) \sim Y_O^{0.39}$.

5.4.2 Graphical View of Material Property and Finite Rate Chemistry Effects

In order to obtain a graphical view of material property and finite rate chemistry effects, flame spread rates over composites with $\phi = 0$ (HDPE) and $\phi = 0.6$ were also measured at various Y_O. The results are plotted in Figure 5.10. For the HDPE, the spread rate could only be measured for Y_O equal to about 0.62 or higher. Below this value, the polymer dripped and ran and the flame front became disjointed and distorted.

The results shown in Figure 5.10 reveals that u_f decreases with Y_O for all composite compositions. It can be seen however, that u_f only changes with ϕ when Y_O is less than about 0.7, its value increasing as ϕ increases. Since u_f is inversely proportional to $\lambda_s \rho_s C_s$ (see equation 5.1), the fastest spread rates should be observed at the composite composition that results in the lowest $\lambda_s \rho_s C_s$, all other things being equal. From the property data of Figure 3.8, we see that the lowest values of $\lambda_s \rho_s C_s$ occur at $\phi = 0.6$. This, as seen in Figure 5.10, is also the composition at which the fastest spread rates were observed in the range where u_f depends on ϕ. Since $\lambda_s \rho_s C_s$ is a measure of the absorbed and transmitted heat through the solid which in turn will dictate the rate of

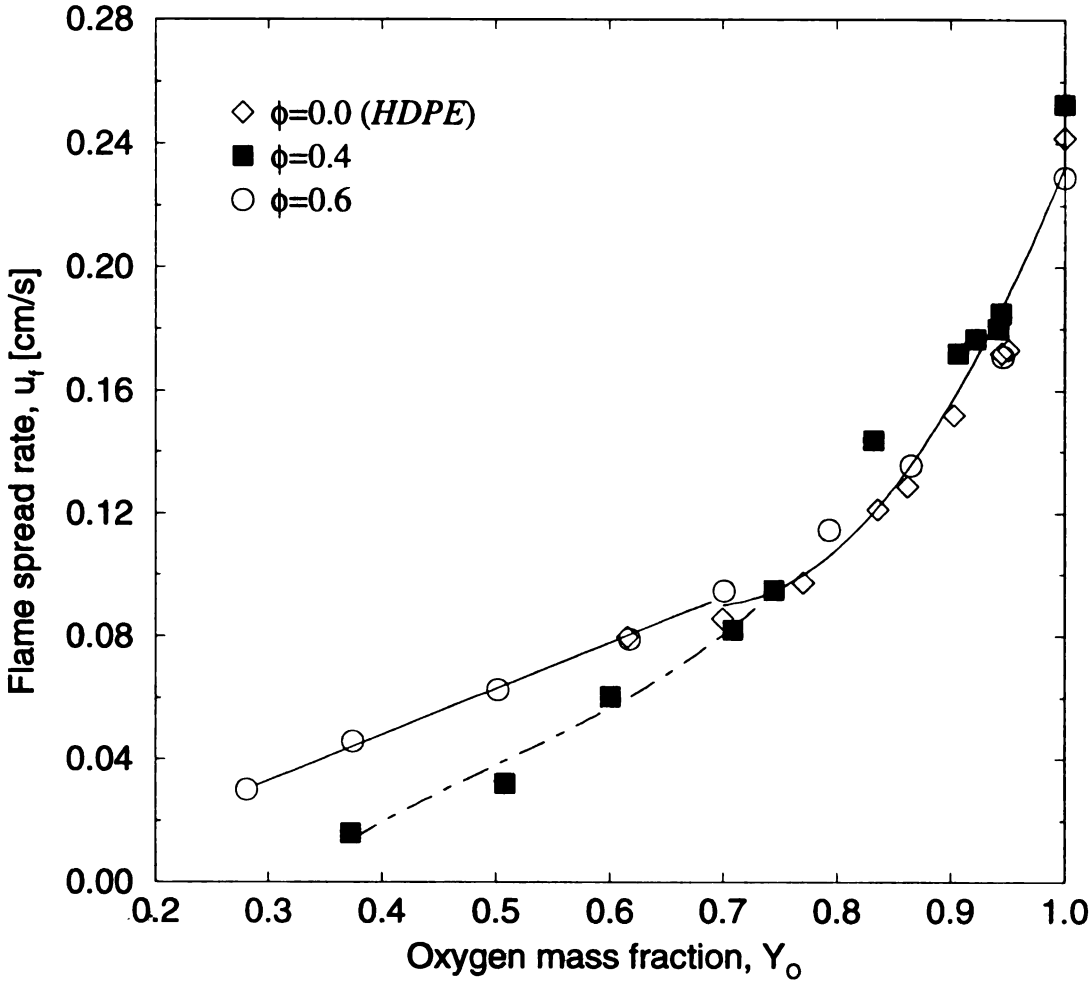

Figure 5.10: Variation of u_f with Y_O and ϕ

pyrolysis, and hence of reaction, we can conclude that finite rate chemistry dominates the spread process in the range $0 \le Y_O \le 0.7$.

In order to further explore the nature of the finite chemistry factor f_4, the values of κ as given in equation 5.1 are calculated. To obtain approximate values of the gasification temperature, T_v used in the calculation, the burnout temperatures recorded by the first five to six thermocouples on any given sample was averaged. Such average burnout temperature was obtained for five or more composite samples at the same composition and the results also averaged. This final value was then taken as an estimate of T_v for that particular composition. Following this procedure, the T_v values obtained are 700, 840, and 910 K for $\phi = 0$ (HDPE), 0.4, and 0.6 respectively. On the other hand, the values for T_f and T_{f_d} were taken from correlation of the data in [61] with Y_O. The values of the mean temperature, T_m were similarly calculated and in turn used to evaluate the gas properties, λ_g, and $\rho_g C_{p_g}$.

As discussed earlier, if the flame chemistry at $Y_O = 1.0$ is considered to be fast enough to approach the infinite chemistry rate, then κ $(=\kappa_\infty)$ can be thought of as representing the proportionality constant for the flow velocity so that $u_g = \kappa_\infty \left[g_x \alpha_g \left(T_{f_d} - T_\infty \right) / T_\infty \right]^{1/3}$. The expression for u_f will then be

$$u_f = \kappa_\infty \left[g_x \alpha_g \left(\frac{T_{f_d} - T_\infty}{T_\infty} \right) \right]^{1/3} \frac{\lambda_g \rho_g C_{p_g}}{\lambda_s \rho_s C_s} \left[\frac{T_f - T_v}{T_v - T_\infty} \right]^2 \tag{5.4}$$

Assuming that the finite rate chemistry influence is contained solely in the multiplicative factor, at other values of Y_O, we will have

$$u_f = \kappa_\infty \kappa_{ch} \left[g_x \alpha_g \left(\frac{T_{f_d} - T_\infty}{T_\infty} \right) \right]^{1/3} \frac{\lambda_g \rho_g C_{p_g}}{\lambda_s \rho_s C_s} \left[\frac{T_f - T_v}{T_v - T_\infty} \right]^2 \tag{5.5}$$

where κ_{ch} is the finite rate chemistry factor. It is therefore possible to calculate κ_{ch} by using equation 5.1 to calculate the value of the multiplicative factor κ and dividing the result at any value of Y_O by the value obtained at $Y_O = 1.0$.

The values of κ calculated using the u_f-θ data of Figure 5.6 are plotted in Figure 5.11. As expected, the values decrease slightly as θ increases indicating the effect of u_g. The near parallelity of the trendlines for Y_O = 0.9 and 1.0 however suggests that $\kappa_{Y_O} / \kappa_{Y_O=1}$ ($= \kappa_{ch}$, according to the definition above) may be independent of u_g below a critical opposed flow velocity which depends only on Y_O.

To check the validity of this possibility, the published data of Lastrina et al. [20] can be used. The reported flame spread rates over thermally thick PMMA samples in an opposed forced flow field are reproduced in Figure 5.12. The data have been plotted in the SI units rather than the units used in the original article.

The calculated values of κ_{ch} based on the reproduced data are shown in Figure 5.13. The relevant properties for PMMA, taken from reference 61, are: $T_v = 668\,\text{K}$; $\lambda_s = 0.2679\,\text{W/mK}$; and $\rho_s C_s = 2093\,\text{kJ/m}^3\text{K}$. The results show that κ_{ch} is initially constant as u_g is increased and start to decrease only when u_g exceeds a critical value. Based on these plots, the limiting flow velocity seems to be around 245 cm/s.

In order to compare the trend of κ_{ch} for various materials, the plots of the calculated κ ratio (κ_{ch}) for all u_f-Y_O data measured over the composites and over

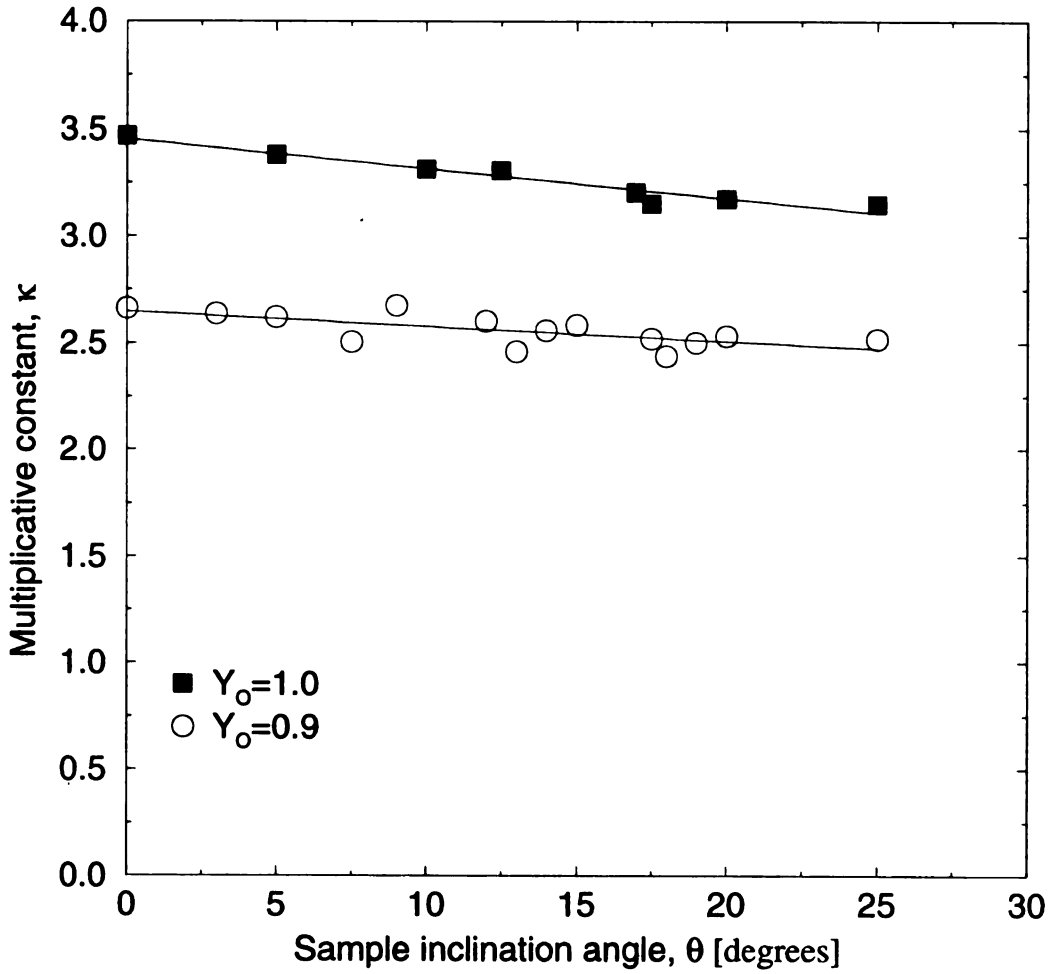

Figure 5.11: Plot of multiplicative factor κ with inclination angle θ

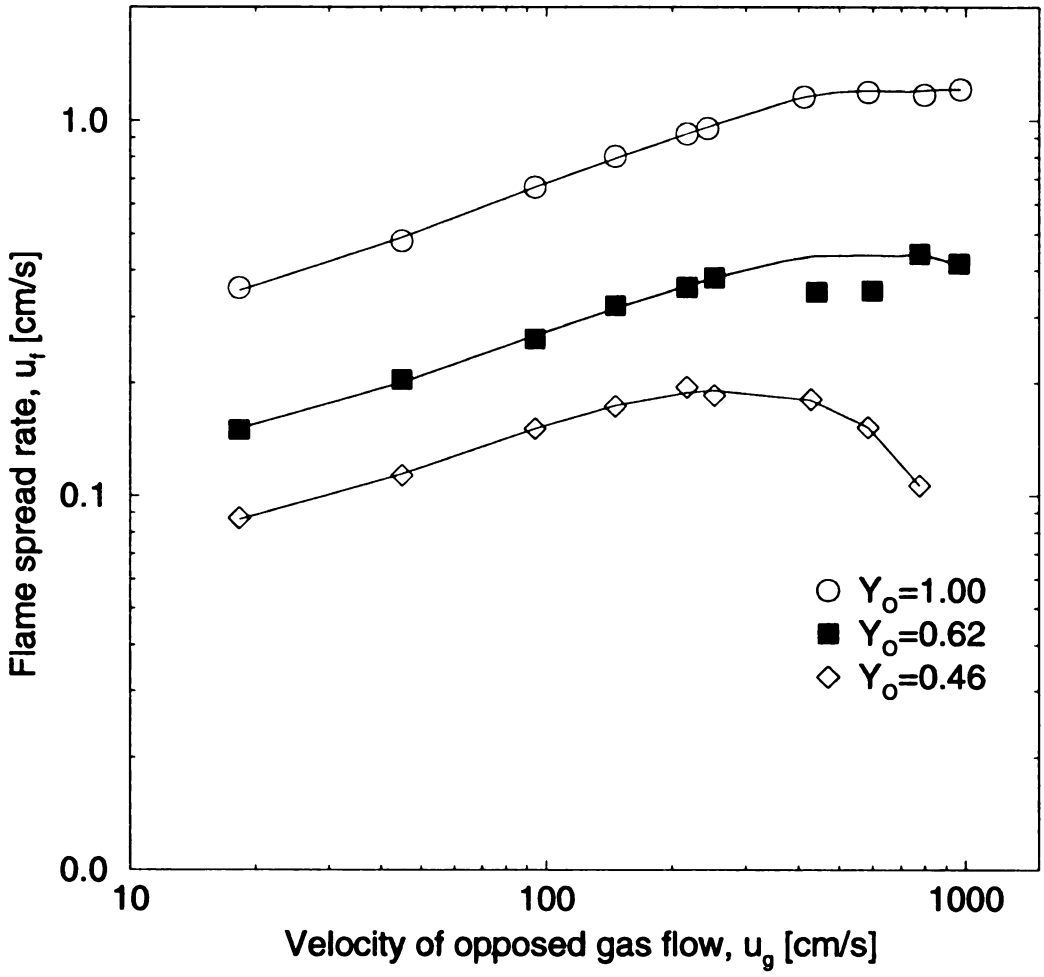

Figure 5.12: Data of Lastrina et al. [20]; plot of u_f versus u_g

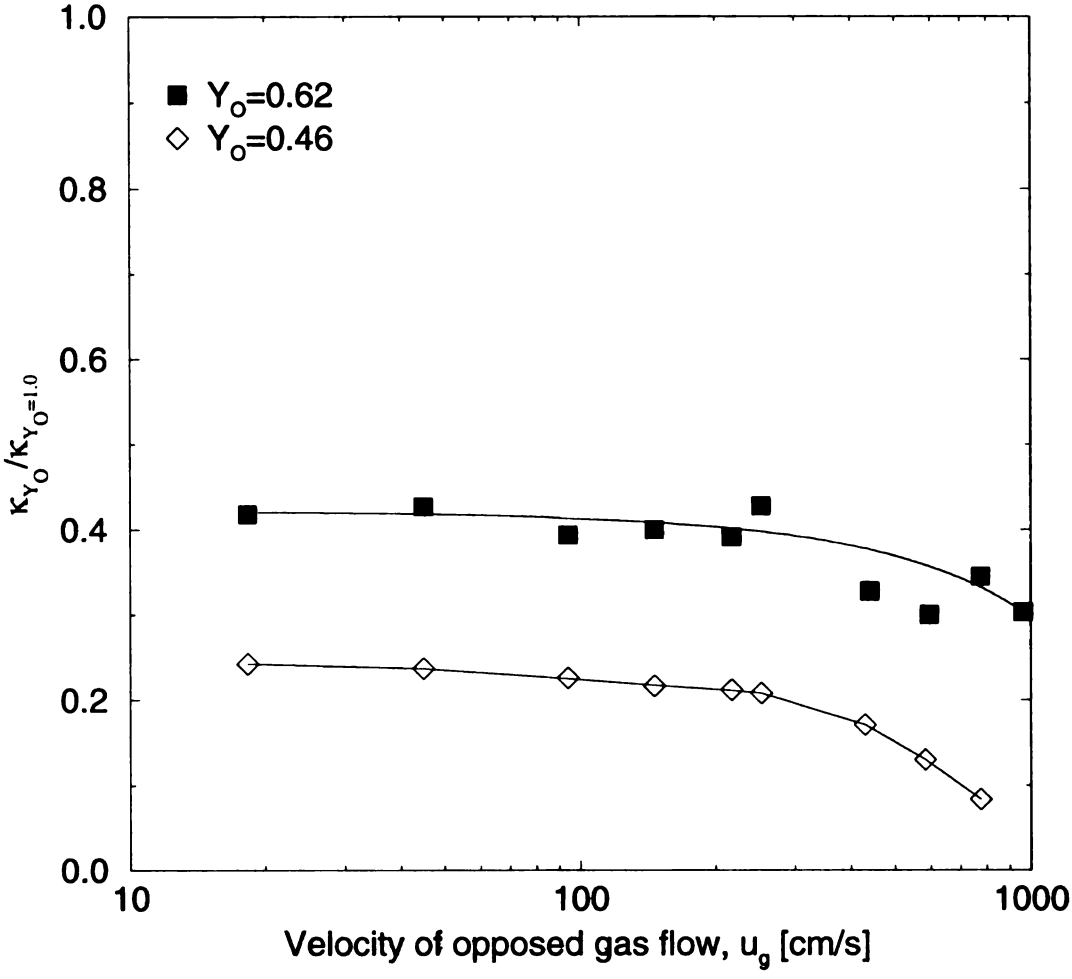

Figure 5.13: Variation of calculated κ_{ch} with u_g

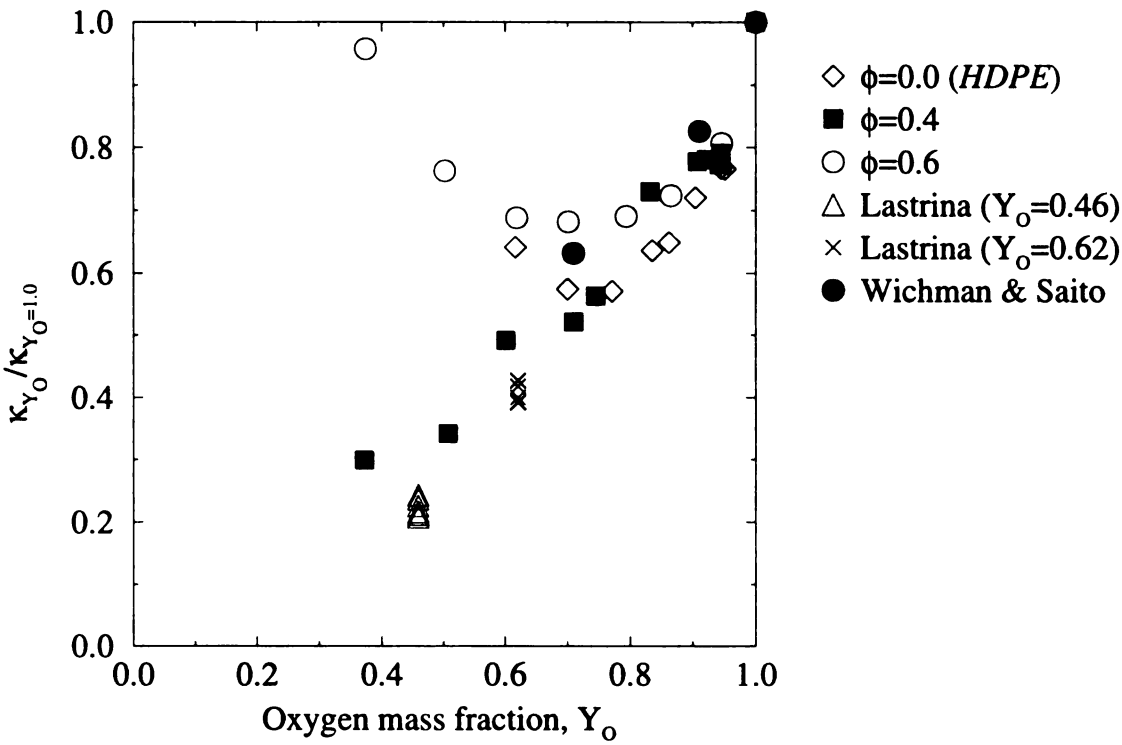

Figure 5.14: Plots of κ_{ch} with Y_O using various experimental data

PMMA samples (data of Lastrina et al. [20]) are shown in Figure 5.14. Also included are data from the experimental study by Wichman and Saito [37] in which gravity effects on flame spread rates over thermally thick PMMA samples were investigated.

As seen in Figure 5.14, the data approximately collapse into a single curve for $Y_O > 0.7$ and disperse when the oxygen fraction is below this limiting value. Since the pyrolysis rate, and hence the reaction rate, is expected to depend very much on material properties, these results further indicate that finite rate chemistry effects are not significant when Y_O is 0.7 or higher. Below this limiting value however, finite rate chemistry becomes the dominant flame spread controlling mechanism.

Another insight gained from Figure 5.13 is that chemistry factor, κ_{ch} may not always be less than κ_∞ in contrast to the intuitive expectation that the multiplicative chemistry factor will increase gradually with increase of Y_O and approaches κ_∞ asymptotically as the value of Y_O approaches unity.

5.5 Conclusions

The complex influence material properties can have on opposed flow flame spread over thermally thick samples has been examined in this chapter. The limits of the oxygen mass fraction below which finite rate chemistry effects become very significant have also been suggested based on the experimental data. The results seem to suggest that finite rate chemistry will dominate the flame spread process over any solid material when the oxygen mass fraction is about 70% or below. Above this limit, heat transfer from the flame to the unburned fuel ahead seems to be the dominant factor.

From the qualitative results of the chapter, it can also be concluded that the 40/60 HDPE/wood fiber composite exhibits wood-like behavior from the fire safety point of view. The composite is more fire-safe at this composition than the HDPE thermoplastic by itself under ordinary conditions.

The measured flame spread rates over the composites for different values of oxygen mass fraction produced correlations which agree very well with previous studies. The results also generate new insights useful for further development of flame spread theory such as the trend of the finite chemistry factor in relation to the infinite chemistry limit.

CHAPTER 6

CONCLUSIONS AND RECOMMENDATIONS FOR FUTURE WORK

The work presented in this dissertation has revealed the complex interplay of various processes in dictating the thermal and fire behavior of wood fiber/polymer composite materials. It has been shown, through series of experimental and numerical studies, that various factors including gravity, thermal property variation, material decomposition, and finite-rate chemistry all have significant influences on the rate of flame spread, but it is possible to study the influence of each factor in "quasi isolation" of the others.

Investigation of thermal properties of the composite material showed that variations of the effective properties with temperature diminish as the wood fiber mass fraction in the composite is increased. For composites containing 50% or more wood fibers by mass, the effective thermal responsivity was found to be essentially invariant with temperature while the effective thermal diffusivity changes only slightly. Also, the trend of the results indicated that composites containing 50% wood fibers and 50% polymer matrix will exhibit superior fire safety properties while still retaining the desired characteristics that originate in the polymer, e.g. ease of manufacture, toughness, etc.

As a means of predicting the effective thermal conductivity of the composite from those of its constituent materials, it was shown that the spherical inclusion model, which assumes that the material is isotropic, produced results that were in excellent agreement with the experimental values. This implies that the composite is close to being isotropic

and hence, a more complicated two-dimensional or three-dimensional thermal property determination procedure is not necessary. It was also pointed out that, based on the results of the investigation, the assumption of constant properties in numerical models for calculating the rate of flame spread over the composite will not lead to significant errors provided the wood fiber mass fraction is 40% or more and the initial temperature is between 290 and 340 K.

A similar study to determine the thermal properties of various proprietary sound blanket materials used in automobile bulkhead assembly separating the engine and the passenger compartments showed that the methods used for determining the thermal properties of the composites cannot be readily used for this low thermal property materials. It was necessary to determine the specific heat capacity using other methods, hence the DSC method was chosen. The numerical simulations of the effectiveness of the materials indicated that the addition of protective covering layer of polyester scrims to glass fiber mat increases its effectiveness as a thermal barrier slightly, but the superior material is the ceramic fiber.

The experimental studies of flame spread over thermally thick samples of the composite materials showed that material properties can have complex influence on the opposed flow flame spread rate. It was shown that, based on the experimental results, finite rate chemistry seems to dominate the flame spread process when the oxygen mass fraction is about 70% or below. Above this limit, it appears as if heat transfer from the flame to the unburned fuel ahead is the dominant factor.

From the qualitative flame spread results, it was concluded that when the composition is 40:60 wood fiber to HDPE by mass, the composite exhibits a wood-like

behavior from the fire safety point of view. The implies that the composite is more fire-safe at this composition than the HDPE thermoplastic by itself under ordinary conditions.

The measured flame spread rates over the composites were correlated over a range of oxygen mass fraction and the correlations were shown to be in good agreement with previous studies. The results of the correlations also revealed that the multiplicative finite chemistry factor, κ_{ch}, may not always be less than the infinite chemistry equivalent, κ_{∞}, in contrast to the commonly-held intuitive expectation that the multiplicative finite chemistry factor will increase gradually with increase of Y_O and approaches κ_{∞} asymptotically as the value of Y_O approaches unity.

As seen in chapter 5, the results on the variation of flame spread rate with sample inclination angle revealed an unusual trend around $\theta = 15°$, suggesting the possibility of local instability in that region. It will be important, therefore, to combine flame spread measurements with sophisticated flow field visualization experiments so as to establish, in detail, the flow pattern during flame spread. This will not only enable the apparent anomalous behavior to be resolved but will, in general, lead to a better understanding of fluid flow influences on opposed flow flame spread over the solid material.

Also, it is seen that the rates of flame spread were determined from transient temperature data measured by means of thermocouples embedded in the material close to the surface being tested. Although, their presence is expected to have minimal effect on the flame spread process, the use of the thermocouples nevertheless constitute an intrusive temperature measurement method. It will be interesting to utilize a non-intrusive technique, such as the infra-red radiation method, to measure the temperature history at

the surface of interest and compare the resulting flame spread rates with the results in this dissertation. Such a procedure will also reveal the variation of flame arrival surface temperature with sample inclination angle much better and thus allow a more precise correlation of the experimental data.

Finally, it will be valuable to conduct a detailed decomposition study of the composite material. Although such a study was done in Appendix A using cellulose and the conditions under which the results will be valid for the wood fiber/HDPE composite were prescribed, it is better to study the decomposition of the composite directly. To this end, future work that incorporates the identification of products of decomposition of the composite material can provide a more accurate picture of its pyrolysis. This in turn will aid further development of the flame spread theory and provide parameters that are necessary to undertake numerical flame spread research as well as calculating such variables as the Damköhler number used, for instance, for correlating the rates of flame spread over the material.

APPENDICES

APPENDIX A

EXAMINATION OF THE MECHANISMS FOR THERMAL DECOMPOSITION

A.1 Abstract

In this appendix, the decomposition mechanisms for cellulose, as a representative material for the composites, are studied. Three decomposition schemes, including the one-step engineering scheme, the three-step delinked scheme proposed by Shafizadeh and Chin, and the three-step coupled scheme of Broido, are examined. The one-step scheme, though simple, can describe many behaviors observed in real problems. These include pyrolysis temperature variation with heating rate, fixed change of pyrolysis temperature with successive doubling of heating rate, and the influences of variable char yield. In addition, kinetic constants may be chosen that fit the one-step model predictions of the three-step schemes. Among the three-step schemes, it can be argued that the Broido scheme is superior because it has coupled competition between the two main product pathways.

A.2 Introduction

Wood is an extremely difficult material to characterize, hence much previous research has focused instead on cellulose. The rationale is that pure cellulose is a good model for wood, which itself is approximately 75% cellulosic, the remainder being primarily lignin. To some extent, the same is true of high density polyethylene, hence the decomposition behavior of the wood fiber/HDPE composites can be inferred from the results obtained

for cellulose. Intuitively, one expects that if an accurate and useful description of a relatively simple substance like cellulose cannot be found, the prospects for describing complex materials like wood or wood/HDPE composites are slim indeed. In reality, the importance of studying cellulose extends far beyond its use as a simplified substitute wood. Cellulose is in fact a major constituent material of most households and therefore represents an important fraction of the domestic fuel load threatened by fire.

In spite of the relative simplicity of cellulose, however, the models of its decomposition, or pyrolysis, have many forms, see Table A.1. The simplest model is the one-step global or engineering model [64-66]. Many such one-step models are in fact used to calculate wood pyrolysis rates. Extensions of the simple thermal degradation model have recently been made [67] to include global oxidation of the cellulose plus global oxidation of the final char. Nevertheless, the fundamental form of the resultant model is qualitatively the same. Each reaction makes products in fixed ratios which must be determined experimentally. Clearly there is competition between the separate thermal and oxidative degradation steps as discussed in detail in reference 67.

A more complex family of decomposition models than the one-step model has been developed by chemists. Their interest is primarily in describing the separate steps of the process [68-70], much as in gas-phase chemical kinetics. The simplest model is the three-step *delinked* model proposed by Shafizadeh and Chin [68] and used thereafter by numerous authors, some extending it to describe wood [71]. In this model the virgin cellulose decomposes directly into three different compounds, char, tar, and inert gases (see Table A.1). Competition occurs between the separate steps, which are delinked. The only linking between char, tar, gases, and cellulose occurs through the mass conservation

constraint, $\sum_{i=1}^{N} y_i = 1$, where y_i is the mass fraction of specie i, defined as mass of specie i divided by initial sample mass of the cellulose. A similar model was proposed by Lipska and Parker [72], although theirs, for which they never wrote model equations, is zeroth order in the initial cellulose unzipping step. However, a zeroth order decomposition step poses severe modeling difficulties, especially if the remaining steps are not zeroth order. Nevertheless, there is much valuable insight in reference 72 concerning the separate rates for the crystalline and amorphous regions, and the hypothesis that char and tar are formed after the cellulose has unzipped essentially to levoglucosan. However, without any model equations or kinetic constants it is difficult to proceed with an analysis based on their observations.

A three-step model that is at least qualitatively similar to the Lipska-Parker model is the mechanism of Broido [70,73]. This model, developed after many years of experimental research, is different from the delinked scheme in that the decomposition of cellulose into products occurs through processes which are coupled. Hence, a change in the rate of production of one component, say char, through increased k_c, is accompanied by a change in the rate of production of y_A, the *active* cellulose, which in turn changes the rate of production of tar and gases. It is this powerful statement of mass or atom conservation at the molecular level and its simplicity of expression, generality, and capability for refinement that make the Broido scheme an attractive model. Interestingly, Shafizadeh, who originally postulated the delinked three-step scheme [68], later abandoned it (reference 69) in favor of one resembling Broido's even to the point of measuring the kinetic constants that are used in this study.

There are some drawbacks of the Broido scheme. For instance, there has apparently been no direct proof of the existence of active cellulose [73]. Hence there is room here for refinement. However, from the viewpoint of modeling, the lack of proof of active cellulose existence is really not a serious drawback. It is certain that the decomposition process does not occur through a single step like cellulose → active cellulose. In other words, the cellulose does break down through a complex sequence of individual steps involving depolymerization, abstraction of various molecules and compounds, etc. But even if the individual decomposition pathways are all known, it will still be desirable to represent all of them with a single step. Hence, the use of an *active* intermediate completely fulfills the modeling requirements.

The most complex family of cellulose degradation models are the various fundamental chemical models that attempt to isolate actual single steps. Although these basic studies may eventually provide insight into detailed cellulose oxidation mechanisms or the influences of various catalysts and impurities, they have not yet made a significant impact on the modeling problem and hence, will not be discussed further in this work.

The focus in this study is on the decomposition mechanisms only. Hence, the cellulose sample is assumed infinitesimally thin thereby eliminating heat transfer and species transport effects [74]. Also, the complicating influences of moisture are ignored.

A.3 Decomposition Models

In this section, the solutions of the three models shown in Table A.1 for constant-temperature heating are examined. The values of the kinetic constants appearing in the

schemes, reproduced from [73] are shown in Figure A.2. Noting that a sample that is heated to a certain test temperature must pass through fleeting intermediate temperatures, it is clear that the constant-temperature heating is, at best, a limiting case of the variable-temperature heating covered in section A.4. Interpretations of the symbols and variables used in Table A.1 are explained in detail in the nomenclature section of this appendix.

For the one-step model, the solution for the *normalized residual mass*, $z = (y - y_c(\infty)) / (1 - y_c(\infty))$, is $z = e^{-\tau}$, where τ is the normalized time. As noted in [75], it is impossible to discriminate between the remaining separate components of the residual mass during decomposition unless additional formulae describing their relative proportions are given. Hence, as far as the solid residue problem is concerned, the one-step model is incomplete.

In order to solve the decomposition equations of the three-step delinked model efficiently, a non-dimensional ratios of the kinetic rate constants is defined as $\alpha_i = k_i / k_{CELL}$. Then $y_{CELL} = \exp(-k_{CELL}t)$, $y_i = \alpha_i(1 - y_{CELL})$, $i = c, T, g$. If at time t_* the heating temperature was to be changed stepwise from T_{test1} to T_{test2}, this would lead to $y_{CELL} = y_{CELL}(t_*)\exp[-k_{CELL2}(t - t_*)]$, $y_c = y_c(t_*) + \alpha_{c2} y_{CELL}(t_*)[1 - y_{CELL} / y_{CELL}(t_*)]$, etc. Here, the parameters k_{CELL2}, α_{c2}, ... are evaluated at T_{test2}. The ultimate char yield for this two-stage heating is $y_c(\infty) = y_c(t_*) + \alpha_{c2} y_{CELL}(t_*) = \alpha_{c1} + (\alpha_{c2} - \alpha_{c1}) y_{CELL}(t_*)$. The first term is the value that would be obtained if heating continued indefinitely at T_{test1}. The second term represents the increment produced by changing T_{test}. It is negative when $T_{test2} < T_{test1}$ and positive when $T_{test2} > T_{test1}$.

Table A.1: The three reaction schemes examined and their corresponding parameters
(see the nomenclature section at the end of this appendix for notation)

Model	Constant Temperature Heating		Variable-Rate Heating
	Kinetic Mechanism	Parameters	
One-step	$\dot{y} = -k(y - \delta)$	$\delta = y_c(\infty)$ $k = A\exp(-E / RT)$	$\dot{z} = -zf(\theta)$
Shafizadez-Chin	$\dot{y}_{CELL} = -k_{CELL} y_{CELL}$ $\dot{y}_c = k_c y_{CELL}$ $\dot{y}_T = k_T y_{CELL}$ $\dot{y}_g = k_g y_{CELL}$	$k_i = A_i \exp(-E_i / RT)$, $i = CELL, c, T, g$ $k_{CELL} = k_c + k_T + k_g$	$\dot{y}_{CELL} = -y_{CELL} f_{CELL}(\theta)$; $\dot{y}_i = \alpha_i y_{CELL} f_i(\theta)$, $i = c, T$ $y_g = 1 - (y_{CELL} + y_c + y_T)$
Broido	$\dot{y}_{CELL} = -k_{CELL} y_{CELL}$ $\dot{y}_A = k_{CELL} y_{CELL} - (k_c + k_T) y_A$ $\dot{y}_c = \mu k_c y_A$ $\dot{y}_T = k_T y_A$ $\dot{y}_g = k_c y_A (1 - \mu) / \mu$	$k_i = A_i \exp(-E_i / RT)$ $i = CELL, c, T$ μ = maximum char yield	$\dot{y}_{CELL} = -y_{CELL} f_{CELL}(\theta)$ $\dot{y}_A = y_{CELL} f_{CELL}(\theta)$ $-(\alpha_T f_T(\theta) + \alpha_c f_c(\theta)) y_A$ $\dot{y}_c = \mu \alpha_c y_A f_c(\theta)$ $y_T = (\alpha_v / \mu \alpha_c) y_c$

Table A.2: Kinetic constants for the decomposition schemes
(Adapted from reference 73)

Specie	Pre-exponential Factor (min^{-1})	Activation Energy (kcal/mol)
Cellulose	1.7×10^{21}	58.0
Tar	1.9×10^{16}	47.3
Char	7.9×10^{11}	36.0
1-step scheme	1.03×10^{16}	46.2

If the char yield varies, the tar and gas yields must also be modified. The yields of these products of decomposition depend strongly on the temperature. A useful measure is the crossover temperature, T_{cr}, for the char and tar reaction rates, given as the value of T at which $k_T = k_c$, viz.,

$$T_{cr} = \frac{(E_T - E_c)/R}{\ln(A_T / A_c)} \tag{A.1}$$

When $T > T_{cr}$ we have $k_T > k_c$. Tar production dominates charring. When $T < T_{cr}$ the reverse is true. Normally, $T_{cr} \sim 300\ ^{\circ}C$ [73].

For the three-step Broido model, the equations of Table A.1 are easily solved for the constant test temperature case. The solutions are:

$$y_{CELL}(t) = \exp(-k_{CELL}t), \quad y_A(t) = \frac{1}{1-(\alpha_T+\alpha_c)}\left[e^{-(\alpha_T+\alpha_c)k_{CELL}t} - e^{-k_{CELL}t}\right],$$
$$y_c(t) = \frac{\mu\alpha_c}{1-(\alpha_T+\alpha_c)}\left[\left(1-\frac{e^{-(\alpha_T+\alpha_c)k_{CELL}t}}{\alpha_T+\alpha_c}\right)-\left(1-e^{-k_{CELL}t}\right)\right], \quad y_T(t) = \frac{\alpha_T}{\mu\alpha_c}y_c(t) \tag{A.2}$$

It should be noted that $y_{CELL} + y_A + y_c + y_g = 1$ by mass conservation. Also, we have $y_c(\infty) = \mu / (1 + \alpha_T / \alpha_c)$, where μ is the maximum char yield, which is attained in the limit $\alpha_T / \alpha_c \to 0$. This occurs when T_{test} is significantly lower than T_{cr}, where T_{cr} is given by Equation A.1. Using the typical value, $\mu = 0.35$ the variation of the residual mass of the various species with time are as shown in Figure A.1. The deductions for the case of stepwise change in test temperature are the same as with the three-step delinked model. The residual mass of the various species for the case where the test temperature is 290 °C for the first 15 minutes and 330 °C thereafter are shown in Figure A.2. It can be seen that the increase in test temperature is accompanied by a significant increase in the rates of decomposition and shortening of the total pyrolysis time.

In this paragraph and the next, it will be demonstrated that it is possible to derive reasonable kinetic constants for the one-step scheme from the three-step schemes. For this purpose, attention is focused momentarily on the Broido scheme. As a principal measure, the *normalized residual mass* will be employed. For the one-step scheme this is simply z, as defined in the paragraph on the one-step model. For the Broido scheme the remaining mass is $y_{CELL} + y_A + y_c$ if we count tars as *volatiles* that no longer belong to the solid. The normalized residual mass is $z = [(y_{CELL} + y_A + y_c) - y_c(\infty)] / [1 - y_c(\infty)]$. Substitution of Equations (A.2) into this formula leads to $z = [e^{-\alpha s} - \alpha e^{-s}] / (1 - \alpha)$, where $\alpha = \alpha_T + \alpha_c$ and $s = k_{CELL} t$.

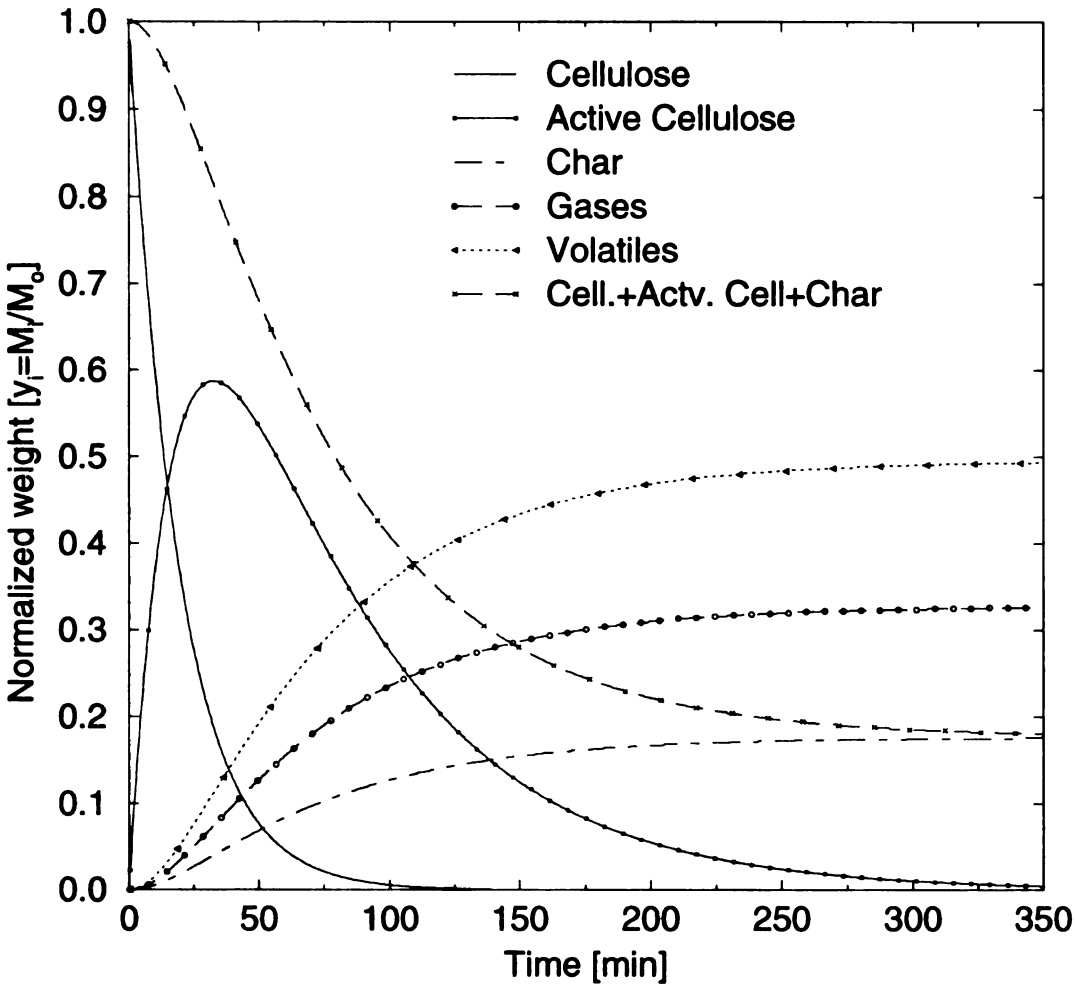

Figure A.1: Numerical solution of Broido Model, T_{test}=290 °C

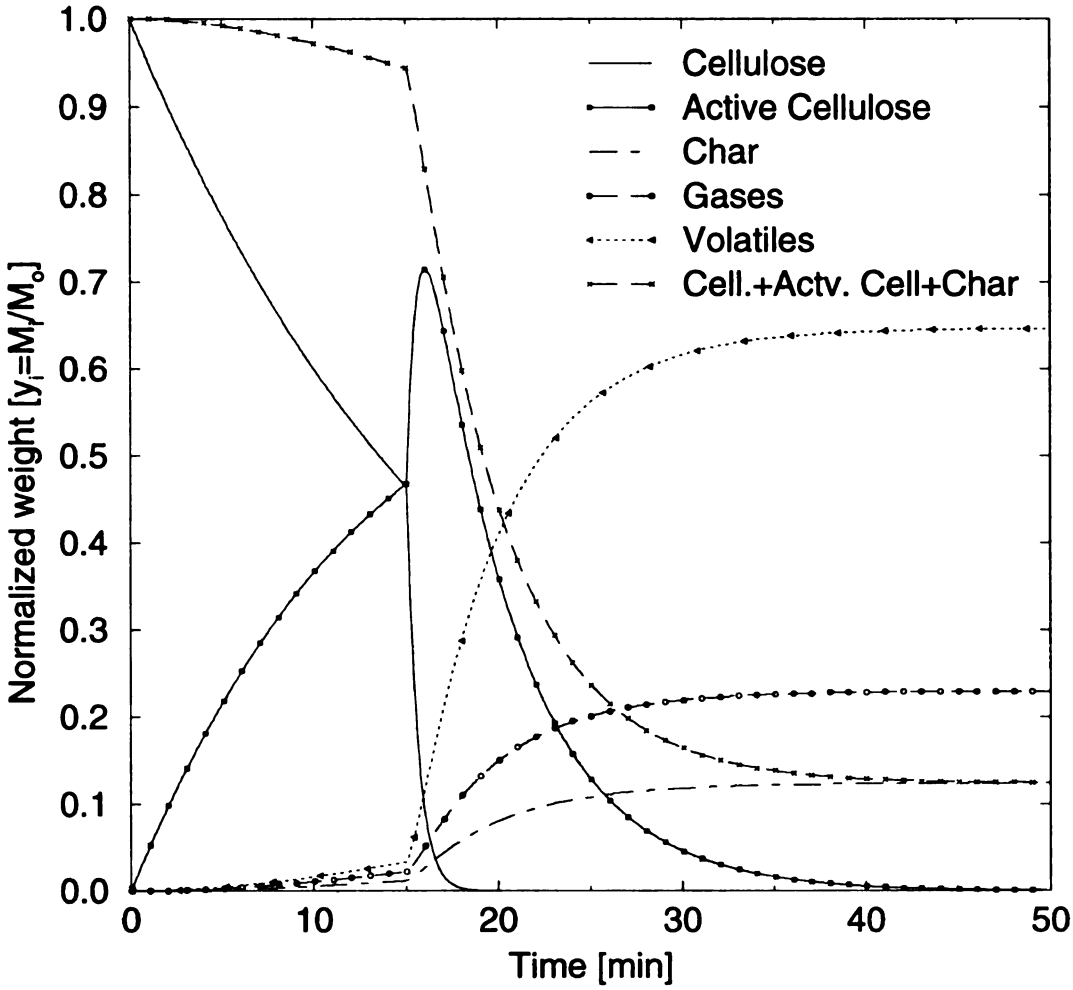

Figure A.2: Broido Model, T_{test}=290 °C up to 15 min; 330 °C thereafter

The following procedure can then be followed in order to derive rate constants for the one-step scheme. First, two test temperatures, $T_{test\,1}$ and $T_{test\,2}$, are fixed. Next, the values of heating times $t_{test\,1}$ and $t_{test\,2}$ needed to reduce z to e^{-1} are calculated from the Broido z-equation for these test temperatures. For the one-step scheme, $z = e^{-1}$ when $\tau = 1$. Hence, $t_{test} = [A\exp(-E / RT_{test})]^{-1}$. The rate constants A and E can thus be calculated from the two sets of T_{test} and t_{test} from the Broido scheme using

$$E = RT_{test\,1} \ln X / (1-\gamma) \qquad A = t_{test\,1}^{-1} X^{1/(1-\gamma)} \tag{A.3}$$

where $X = t_{test\,1} / t_{test\,2}$ and $\gamma = T_{test\,1} / T_{test\,2}$. Using the values for A_{CELL}, A_c, A_T, E_{CELL}, E_c, and E_T shown in Table A.2 and utilizing test temperatures $T_{test\,1} = 550$ K and $T_{test\,2} = 850$ K gives $t_{test\,1} = 15064$ sec and $t_{test\,2} = 0.0272$ sec. Substitution of these values in Equations (A.3) yields $E = 40.9$ kcal/mole and $A = 1.24 \times 10^{12}$ sec^{-1} as reasonable one-step parameters derived from the three step Broido scheme parameters. A test time comparison shows that near 500 K and 850 K the one-step formula is accurate. In between it may differ by up to 30%.

Ideally, one should like to minimize the normalized residual mass difference $z_{\text{BROIDO}} - z_{\text{1-STEP}} = [e^{-\alpha k_{CELL} t} - \alpha e^{-k_{CELL} t}] / (1-\alpha) - e^{-\tau}$ for each T_{test}. To this end, α and k_{CELL} can be fixed for a given T_{test} and a choice of k for the one-step expression that minimizes the difference for all t then sought. It should be noted that for small α, which occurs when $T_{test} \geq 600\ K = 300\ ^{\circ}C$, $z_{\text{BROIDO}} - z_{\text{1-STEP}} \approx e^{-(k_c + k_T)t} - e^{-kt}$ when $t >> k_{CELL}^{-1}$. The latter condition is easily satisfied in practice because k_{CELL} becomes very large as

T_{test} increases. The difference is zero when $k = k_c + k_T$. This reduces to $k \approx k_T$, when $T_{test} > T_{cr}$. Hence, for large T_{test}, the choice of parameters for the one-step model is largely determined by the volatilization step. It is thus reasonable to write $A \approx A_T$, $E \approx E_T$ in the one-step expression.

A.4 Variable-Rate Heating

Here the decomposition equations must be augmented with an energy equation like $dT / dt = g(t)$, $T(0) = T_o$. This equation simply dictates the heating rate imposed on the sample. As a tool, a characteristic heat-up time is defined as $t_{HEAT} = (T_{MAX} - T_o) / g(0)$, where T_{MAX} is the maximum sample temperature. With $\tau = t / t_{KIN}$ and defining a reduced temperature θ, which varies between zero and one, the energy equation,

$$\frac{d\theta}{d\tau} = D^{-1}G(\tau); \qquad \theta(0) = 0 \tag{A.4}$$

and the species equations shown in the rightmost column of Table A.1 are obtained. The initial conditions are $z(0) = 1$, $y_{CELL}(0) = 1$, and $y_i(0) = 0$ for all the other species.

These equations are in standard form for a high-activation-energy-asymptotic (AEA) calculation. Because of the relative largeness of E and the relative smallness of T_{MAX}, the β_i will be at least twice as large as for usual gas-phase AEA calculations. Hence, AEA methods should be quite accurate. The β_i are fairly insensitive to T_{MAX} in the approximate range $300\ ^\circ C \le T_{max} \le 600\ ^\circ C$.

For large β_i the chemical reaction is frozen until θ is close to unity where T is near T_{MAX}. This justifies the definition of a rescaled non-dimensional temperature

$\theta = 1 - \Theta / \beta$. For the one-step scheme the choice of β is obvious, but for the three-step schemes we use $\beta = \beta_{CELL}$, from the initiation step. A one-to-one relationship between temperature and time is now postulated so that Equation A.4 can be written as $d\theta / d\tau = D^{-1}G(\tau) = D^{-1}H(\theta)$, $\theta(0) = 0$. Note that $\theta = 1$ at $\tau = \infty$ and $\theta = 0$ at $\tau = 0$. Hence, $H(0) = 1$ and $H(1) = 0$. The lowest-order equation for Θ is $d\Theta / d\tau = -\Omega\Theta + \cdots$, where $\Omega = |-dH(1) / d\theta| D^{-1}$. When $\Omega >> 1$ the heat-up time is so short that the temperature rise is nearly instantaneous, i.e., $H(\theta) \rightarrow$ step function. One then essentially ignores the energy equation and puts $\theta = 1$ in the species equations to recover the constant -temperature solutions. When $\Omega << 1$ the heat-up time is much larger than the chemical time; not much cellulose is left once the test condition $T = T_{MAX}$ is attained. This limit is experimentally undesirable. The third limit, $\Omega \sim$ O(1), contains features of the other two and therefore is the most interesting. To examine it we substitute $\theta = 1 - \Theta / \beta$ into the species equations and let $\beta \rightarrow \infty$ to obtain $f_i(\theta) = \exp(-\varepsilon_i \Theta)$. The left-hand sides of the equations are also transformed as $dy_i / d\tau = -\Omega\Theta dy_i / d\Theta$. The resulting systems of equations can then be solved, although the solution for the three-step models is quite complicated. A considerable mathematical simplification is obtained by putting $\varepsilon_c = \varepsilon_T = 1$. This, in essence, reduces the analysis to one of the mathematical character of the solution. The results are:

One step: $y = y_c(\infty) + (1 - y_c(\infty))e^{-\nu}; \quad z_{1\text{-}STEP} = e^{-\nu}$

3-step delinked: $y_{CELL} = e^{-\nu}; \quad y_i = \alpha_i(1 - y_{CELL}),\ i = c, T, g$

$$z_{3D.L} \equiv [(y_{CELL} + y_c) - y_c(\infty)] / [1 - y_c(\infty)] = e^{-\nu}$$

3-step Broido: $y_{CELL} = e^{-\nu}; \quad y_A = \frac{1}{\alpha - 1}[e^{-\nu} - e^{-\alpha\nu}]; \quad y_T = \frac{\alpha_\nu}{\mu\alpha_c} y_c;$ (A.5)

$$y_c = \frac{\mu\alpha_c}{\alpha - 1}\left[1 - e^{-\nu} - \frac{1 - e^{-\alpha\nu}}{\alpha}\right]$$

$$z_{BROIDO} = [(y_{CELL} + y_A + y_c) - y_c(\infty)] / [1 - y_c(\infty)]$$
$$= e^{-\nu} + (e^{-\alpha\nu} - e^{-\nu}) / (1 - a)$$

where $\nu = \Omega^{-1}\int_{\Theta}^{\infty} x^{-1}\exp(-x)dx = \Omega^{-1}E_1(\Theta)$.

Some observations can be made from equations (A.5). First, the residual mass decays at the same rate for the one-step and three-step delinked schemes, but for the Broido scheme decays more slowly, by the amount $(e^{-\alpha\nu} - e^{-\nu}) / (1 - \alpha)$. Hence, the ratios $z_{1\text{-}STEP} / z_{BROIDO}$ and $z_{3D.L} / z_{BROIDO}$ are always ≤ 1. At $T = T_{MAX}$, $\nu \to \infty$ so that $z_{1\text{-}STEP} / z_{BROIDO} \to 0$ when $0 < \alpha < 1$. In other words, *more residual mass remains to be pyrolyzed in the Broido mechanism.* Second, it can be seen that for z, the only scheme that shows sensitivity to the various decomposition steps is the Broido scheme. This occurs through the parameter α. The qualitative nature of the dependence does not change when α varies between zero and one. Finally, there are two independent parameters in the three-step delinked model, since $\alpha_c + \alpha_T + \alpha_g = 1$, whereas in the Broido scheme there are three. This implies a greater variety of behaviors for the Broido scheme.

A.5 Constant Heating Rate, $T = T_o + g_o t$

Many experiments are conducted at constant heating rate. Although the upper limit temperature is unbounded, in practice it suffices to discontinue heating once there is no further weight loss. Though the meaning of T_{MAX} is slightly obscured here, the notion of a T_{MAX} remains relevant. Hence, the non-dimensionalization of the previous section is still employed.

The *one-step reaction* is considered first. Putting $G(\tau) = 1$ into Equation A.4 gives $\theta = D^{-1}\tau$ for the temperature distribution. Substitution of this expression into the one-step species equation gives $dz / z = -Df(\theta)d\theta$ subject to $z = 1$ at $\theta = 0$. Upon integration, one obtains $z = \exp[-(D/\beta)I(\Theta,\beta,\sigma)]$, where $I(\Theta,\beta,\sigma) = \int_{\Theta}^{\beta} e^{\frac{-u}{1-\sigma u/\beta}} du$; $\Theta = \beta(1-\theta)$. When β is large we have $I(\Theta,\beta,\sigma) \cong I(\Theta,\infty,\sigma) = e^{-\Theta}$. Consequently the approximate result

$$z = \exp[-(D/\beta)e^{-\Theta}] \tag{A.6}$$

is obtained.

It can be shown, after a rather lengthy analysis, that for successive values of the heating rate, $g_{o_{i+1}} / g_{o_i} = 2$, the change in temperature, $\Delta T_i = T_{i+1} - T_i$, at an identical stage of decomposition is given by

$$\Delta T_i \cong \frac{T_{MAX_i}}{E / RT_{MAX_i}} \frac{\ln 2}{1 + 2(1-\gamma_i)} \tag{A.7}$$

where $\gamma_i \equiv T_i / T_{MAX_i}$ is a number smaller than 1. If $\gamma_i \approx$ constant we see immediately that $\partial(\Delta T_i) / \partial T_{MAX_i} > 0$, indicating that the temperature difference increases with the heating rate. Note that T_{MAX_i} is the value of T at which no more mass loss occurs. It increases monotonically with g_o. Equation (A.7) shows that as $E / RT_{MAX_i} \to \infty$, $\Delta T_i \to 0$, and *the ignition-temperature concept is recovered.* An estimate for ΔT_i can be made from Figure 1. We use the results for the normalized residual solid mass, z, versus T for various heating rates for the Broido mechanism. The numerical solution of the equations are shown in Figure A.3. The curves are very similar to those obtained from the one-step scheme, in that they appear to be displaced by nearly fixed amounts and that at the higher heating rates the gaps seem to widen slightly. For the comparison, we employ the last two curves in Figure A.3 with $g_o = 80\ ^\circ C / \min$ and $g_o = 160\ ^\circ C / \min$. Also, we take $E \sim 40$ kcal / mole and choose the decomposition level as $z = 0.5$. It can be seen that T_i, the value of T when $g_o = 80\ ^\circ C / \min$ and $z = 0.5$, is approximately $465\ ^\circ C$. We estimate that $T_{MAX} \cong 525\ ^\circ C$. Hence $\gamma_i = 0.8$, $E / RT_{MAX} \cong 25$ and $\Delta T \cong 15\ ^\circ C$, which is very close to the ΔT shown in Figure A.3.

Through these results, the general absence of a characteristic pyrolysis temperature T_v has been amply demonstrated. Assumption of a pyrolysis temperature is common in fire propagation models. However, considering the fact that the bulk of the decomposition occurs within a temperature interval of about 25 degrees (see Figure A.3), it can be said that the assumption of an average constant pyrolysis temperature will be reasonable if the variation of such with heating rate is taken into consideration. It is now recognized that

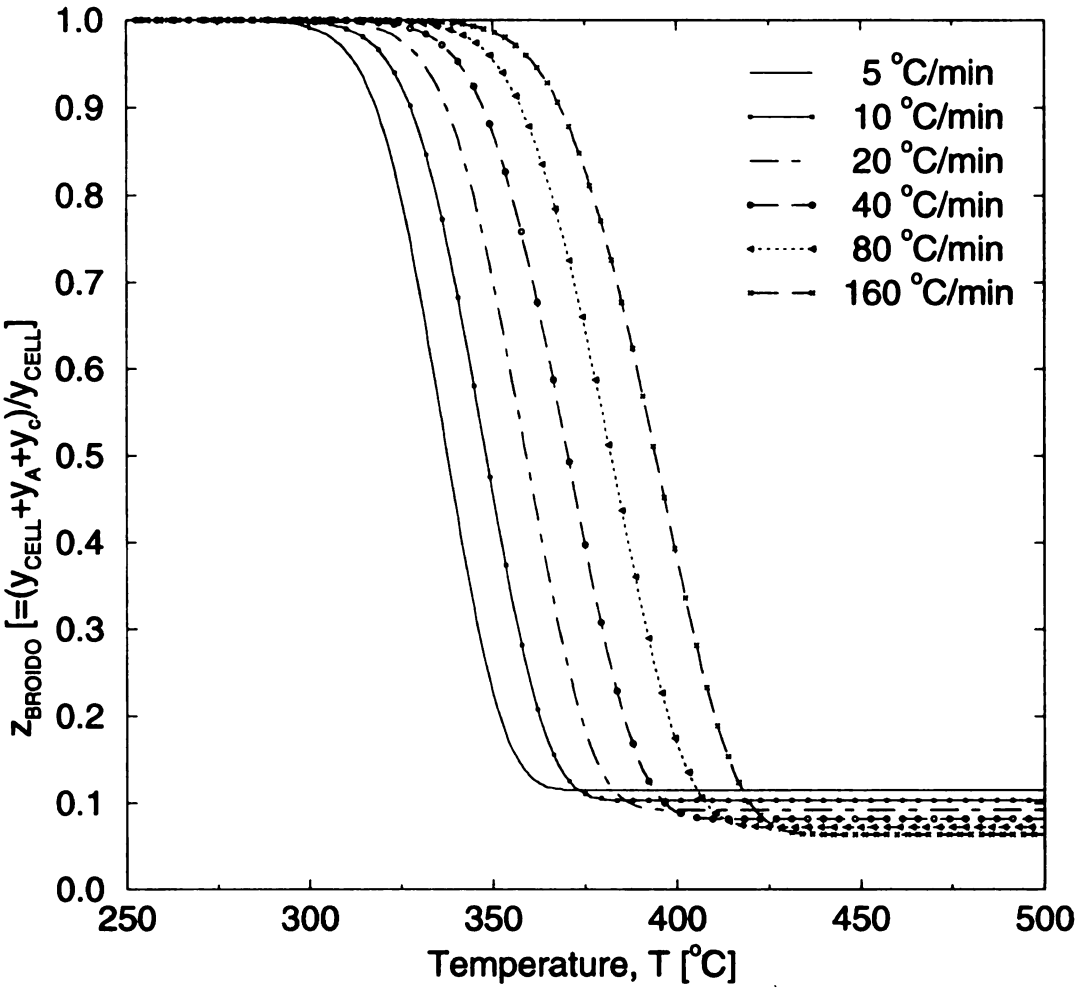

Figure A.3: Numerical solution of the Broido model for various g_o

for flame spread application, T_v will vary with the oxygen mass fraction, Y_O. A further implication of the results of this section is that the T_v- concept appears to be accurate when $E / RT_{MAX} >> O(1)$.

As already mentioned, the fixed heating rate curves for the Broido and one-step mechanisms are qualitatively similar. In fact, plots of dy_s / dt versus T, where y_s is the residual mass which is equivalent to $y_{CELL} + y_c + y_A$ for the Broido scheme and simply y for the one-step scheme, produce only a single peak (see Figure A.4) and are practically identical for both models. This indicates -- according to reference 4 -- a global one-step mechanism. But the Broido mechanism is not a one-step process, it is a three-step process. Hence, we are led to question the generality of deductions made from weight loss rate measurements.

A.6 Discussion

There has been, and continues to be, much interest in the pyrolysis and combustion of wood and other cellulosic materials. Typical technological areas of interest are wood gasifiers, waste incinerators, and fire safety of wood and wood products. A recent issue of importance is the fire safety of composites consisting of wood fiber and a polymeric binder such as wood fiber/HDPE composites which are the subjects of this dissertation. In the realm of modeling, there are few useful and reliable models for standard problems like flame spread over cellulosics, or the flame/smolder transition. The crucial, indeed central, missing link in these models is a robust, accurate description of the solid phase decomposition and pyrolysis.

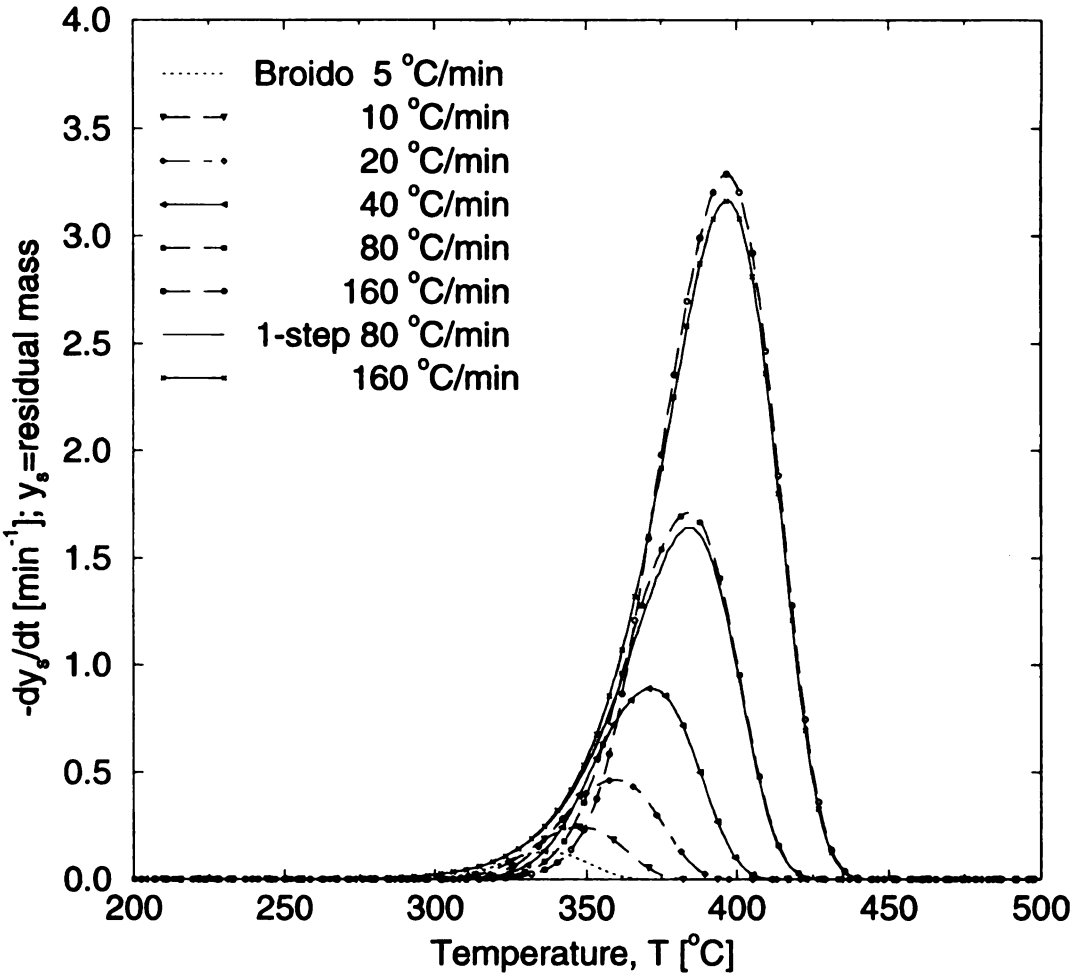

Figure A.4: Plots of dy_s / dt versus T for 1-step and Broido models

Engineers have for many decades employed a relatively simple global one-step decomposition reaction, see the first row of Table A.1. It has been demonstrated herein that this model has positive features, among them being the capability of reproducing several global features of more complicated schemes, as shown in Figures A.3 and A.4. Hence, processes like weight-loss rate can be reasonably effectively modeled, and the basic physics of the constant heating rate can be explained. Nevertheless the global scheme suffers from a serious built-in flaw. The decomposition products are formed in fixed ratios. That is, if we consider char and volatiles as the products, for example, we can generally say only that their ratios are fixed. The only remedy is to painstakingly develop experimentally measured correlations that produce product ratios which vary with temperature and the gas-phase environment. But in this case, it would seem to be more advantageous to simply develop a more realistic model.

The three-step models present a viable solution to this problem. Two strong candidates have emerged, the delinked Shafizadeh-Chin scheme, which is computationally attractive, and the Broido scheme, which is physically attractive. The results of this study have shown that the delinked scheme suffers a (mitigated) form of the one-step-scheme flaw. This is seen by comparing the normalized residual mass for the one-step and the delinked schemes. For the one-step scheme under fixed-temperature heating we have $z = e^{-r}$, and under variable-rate heating $z = e^{-v}$. It is easily shown that the delinked scheme gives exactly the same results. The Broido scheme, however, is completely different. In fact, it is a built-in feature of the Broido scheme that the char and volatile yields vary with the local temperature. Why is this important? Because it can be

employed in models where a transition phenomenon is occurring. An excellent example is the smolder/spread transition phenomenon. Under some conditions, like low temperature, the charring pathway is more active than the volatile pathway. In this case smoldering is observed. Under different conditions the volatile pathway is preferred, in which case a gas-phase spreading flame will be observed. Hence, this competition is in fact necessary to decide the transition event.

Other examples where the char/volatile competition are important are ordinary wind-aided and wind-opposed flame spread models (as in chapter 5) and the generation of volatiles in biomass gasification devices.

There is another feature of the Broido scheme that makes it attractive from the modeling standpoint. For a model to be useful it must be: (1) simple (understandable) and physically consistent with the available evidence, (2) complex and variegated enough to produce interesting, multi-faceted behaviors. In these respects the Broido model is quite satisfactory. We have used Activation-Energy-Asymptotics (AEA) in our analysis of these schemes because the methods suit, not because we have sought schemes for analysis by AEA. Interestingly, for the temperature range of ordinary pyrolysis, $500\ K \leq T \leq 850\ K$, the most important parameter of AEA, the non-dimensional activation energy β, is in a nearly optimum range of values for maximum accuracy of the method. For larger and smaller T, β decreases making the AEA procedure less accurate.

A.7 Conclusions

In this appendix, three reaction schemes used to describe the pyrolysis and degradation of cellulosic materials have been examined. The Broido scheme is shown to be clearly the most versatile. This fact is sometimes misunderstood in the literature, particularly with respect to μ, the maximum char yield. Some investigators have taken μ to represent a fixed char yield. Actually, μ is the maximum char obtainable for experiments performed at temperatures lower than T_{cr} and giving $\alpha_T / \alpha_c << O(1)$. The actual char yield will always be smaller than μ. Support for the Broido model is provided by Lewellen et al. [76], who performed experiments on cellulose at high heating rates. They reviewed the previous models, finding them unsatisfactory, then deduced a new one from their data. Ironically, their predictions can easily be reproduced by the Broido model for high heating rates although their model does *not* reduce to the Broido model for low heating rates. We conclude that the Lewellen-Peters-Howard model is not a new model but a limiting case of the more general Broido model.

One difficulty with the Broido model that has been mentioned in [4] occurs in variable oxygen-concentration environments. Though the Broido and delinked models can probably be recast to exhibit oxidation influences, it is not clear how this can be done for high or low oxygen-concentration environments. We recall that Ref. 4 added separate global cellulose and char oxidation reactions to the existing [1-3] global decomposition reaction.

Concerning the one-step reaction, it has been shown here that it is *useful when qualitative predictions are sought*. Reasonable chemical parameters can be chosen based

on the three-step models. It is a useful tool for understanding the variable-temperature heating rate curves, providing insight into the pyrolysis temperature question. In many respects, then, it describes some features of the more complex three-step mechanisms well. It is possible to generalize the one-step model by introducing a variable char yield instead of the fixed value. For such purpose, one can use the value suggested by Broido,

$$\begin{aligned} y_c(\infty) &= \mu / \{1 + \alpha_T / \alpha_c\} \\ &= \mu / \{1 + (A_T / A_c)\exp[-(E_T - E_c) / RT]\} \\ &= \mu / \{1 + \kappa \exp[-(\varepsilon_T - \varepsilon_c)\beta(1-\theta) / [1 - \sigma(1-\theta)]\}, \end{aligned}$$

where $\kappa = (A_T / A_c)\exp[-(E_T - E_c) / RT_{MAX}]$ and $\varepsilon_i = E_i / E$ where E is the activation energy for the overall decomposition reaction. Obviously, if $(\varepsilon_T - \varepsilon_c)\beta$ is small then $y_c(\infty) = \mu / (1 + \kappa)$, and we shall return to the case of constant char yield.

The results of the analysis have shown that the concept of a single pyrolysis temperature, T_v is at best an approximation. A unique value of T_v exists only in the limit $E / RT_{MAX} >> O(1)$. However, it has also been demonstrated that the parameters of cellulose pyrolysis [6] produce non-dimensional activation energies β_i that are quite large. Hence, one expects that the condition of large E / RT_{MAX} will be fulfilled, and that most wood-based and cellulosic materials will appear to possess a characteristic T_v. This is the basis for utilizing this concept in the flame spread computation and modeling of chapter 5. Furthermore, the most relevant issue for thermally thick materials, as already mentioned, is not whether we have certain fixed value of T_v, but what the status is of the instantaneous competition between the rates of formation of volatiles and char. This mostly determines whether we have flame spread or smolder spread.

Nomenclature

A_i Pre-exponential factor for i^{th} reaction

D $D = t_{HEAT} / t_{KIN}$, a Damköhler number

E_i Activation energy for i^{th} reaction

$E_1(x)$ Exponential integral

$f_i(\theta)$ $f_i(\theta) = \exp[-\beta_i(1-\theta) / \{1-\sigma(1-\theta)\}]$, reaction-rate function

$g(t)$ Heating rate function

G Normalized heating rate, $G(\tau) = g(t) / g(0)$

k_i Kinetic rate constants

R Universal gas constant

t_{KIN} $t_{KIN} = t_{CELL} = [A_{CELL} \exp(-E_{CELL} / RT_{MAX})]$

t Time

T Temperature

X $X = t_{test\,1} / t_{test\,2}$

y_i Species mass fraction, mass of specie i divided by initial sample mass (pure cellulose)

γ $\gamma = T_{test\,1} / T_{test\,2}$

z Normalized residual mass

Greek

α	$\alpha = \alpha_T + \alpha_c$, sum of α s for char and tar steps
α_i	$\alpha_i = k_i(T_{MAX}) / k_{CELL}(T_{MAX}) = t_{KIN} / t_i(T_{MAX})$
β_i	$\beta_i = \sigma(E_i / RT_{MAX})$
γ_i	$\gamma_i = T_i / T_{MAX_i}$
ε_i	$\varepsilon_i = E_i / E_{CELL}$
θ	$\theta = (T - T_o) / (T_{MAX} - T_o)$, normalized temperature
Θ	$\Theta = \beta(1 - \theta)$, normalized stretched temperature
μ	Char yield
σ	$\sigma = 1 - T_o / T_{MAX}$
ν	Function defined in equations (A.5)
τ	Non-dimensional time, $\tau = t / t_{KIN}$
Ω	$\Omega = \lvert -H'(1) \rvert D^{-1}$

Subscripts

A	Active cellulose
c	Char
$CELL$	Cellulose
cr	Crossover value
g	Gas
$HEAT$	Pertaining to heating

KIN	Pertaining to kinetics
MAX	Maximum value
o	Ambient value
p	Pyrolysis value
test	Test condition or result
T	Tar
3*D.L*	Three-step delinked

APPENDIX B

THE INFLUENCE OF WOOD MOISTURE AND WOOD-TYPE ON MECHANICAL/THERMAL BEHAVIOR OF THE WOOD FIBER/HDPE COMPOSITE

B.1 Abstract

In this appendix, the influence of moisture on fiber/matrix adhesion for the wood fiber/HDPE-composites was studied. The main objective is to understand the influences of moisture on the final properties of such materials since moisture is an important constituent of wood and drying, if necessary, is an expensive step in the manufacturing process. It is also desired to establish the extent to which these influences depend on wood-type.

The experiments were conducted using pine fibers, a representative softwood. The wet wood fiber to HDPE weight ratio was kept fixed while the moisture level was varied. Mechanical properties, including tensile, flexure, and impact properties were examined and the results were compared to the results of earlier studies on aspen fibers to deduce the dependence on wood-type. The nature of the results were also used to predict the possible effect of wood moisture on the thermal properties of the composite materials.

The trends of the results suggest that fiber/matrix bonding is best at initially low and initially high moisture contents. Near the FSP (fiber saturation point), where the moisture content is between 20 and 30%, the bonding seems weakest and most of the mechanical properties are relatively low. Scanning Electron Microscopic (SEM) photographs revealed micro-structure details that are consistent with the measured strength properties.

B.2 Introduction

In spite of the numerous advantages of wood fiber-polymer composites, the problem with wood is its hygroscopicity through which it loses or gains moisture, even when in use, depending on the local environmental conditions. This can greatly influence the mechanical and thermal properties of the wood, thus affecting the resulting HDPE-Wood composite quite significantly. In an earlier study by Wichman and Hermann [56,57], the influence of wood moisture on the fiber/matrix adhesion was studied using aspen (a typical hardwood) in attempts to understand how moisture affects the properties of the final composite. The investigation in this appendix is aimed at establishing similar effects using pine, a representative softwood, so that any dependence on wood-type can be fully understood.

The importance of this study is the possibility of revealing the range of moisture levels where adequate mechanical and thermal properties are obtained and any dependence of such on wood-type. This in turn will suggest the possible areas of application of the composite material and the dependence, if any, of its thermal and fire behavior on the environmental conditions in which it is being used. The results may also prove very useful in modeling the fiber/matrix interaction at different moisture levels.

B.3 Experiments

The moisture content, MC, is defined as:

$$MC = \frac{\text{Weight of Water}}{\text{Weight of Dry Wood Fibers}}$$

A known weight of the fibers is oven-dried under vacuum and 105 ℃ and weighed at intervals. The dry weight is reached after four to six hours. The precise MC is accomplished by adding the desired amount of water (by spraying) and/or exposing the fibers to controlled conditions in a humidity chamber pre-calibrated for wood fiber humidification. Equilibrium, established when no further weight change occurs in the fiber, is usually reached in two to three days.

The conditions of the experiments are clearly defined. Various mechanical properties are measured as functions of moisture level which is variable. The composition of the composite matrix is fixed at 40% wood fiber (plus moisture) and 60% HDPE by weight. Hence, as the moisture content is increased by adding water, the overall wood fiber mass fraction in the composite decreases.

The composite is manufactured in the same manner as described previously in chapter 3. Specimens are cut from the final composite slabs for tensile, three-point bending, and impact tests, all according to ASTM standards.

For the tensile and flexural tests, a United "SFM"-Test System was used. In accordance with the specifications in ASTM D 638-86, the dumbbell shape tensile specimens were tested at a speed of 0.127 cm/min. As the test progressed, the load-extension curve was displayed. Various tensile properties like the Young's modulus, tensile strength, peak and break load, extension at tensile strength, and elongation at break were obtained from this curve.

The three-point flexural tests were carried out following the specifications in ASTM D 790-86. The samples were placed on two supports and loaded by means of a loading nose

midway between the supports. The employed span to depth ratio was 16:1 at a span of 5.1 centimeters. The test speed employed was 0.127 cm/min. The specimens deflected under the load and a load-deflection curve was recorded. From this curve the flexural properties like the modulus of elasticity (MOE), peak load, break load, extension at peak, and elongation at break were read or calculated.

The impact specimens were notched to a depth of 0.25 cm as recommended in ASTM D 256-84. Thus a concentrated stress of fixed and controlled dimensions was developed within the samples. A 5-lb Izod pendulum was used to break the test piece. The impact strength is a measure of the work done in breaking the test piece and it expresses the resistance of the material to stress concentration.

B.4 Results

The trend of the various mechanical properties as a function of MC and a comparison with earlier results on aspen fibers [56,57] are presented in what follows. The comparison is aimed more at observing any similarity in behavior between pine and aspen fibers rather than in absolute terms since the various mechanical properties of the two kinds of wood are known to be markedly different [6].

In order to lend support to the interpretation of the data, a one-way analysis of variance test (ONEWAY ANOVA) was carried out. The probability of the observed differences in means of a given property at different MC being real was calculated and used to generate a set of statistical values. Results are shown only for lengthwise fiber orientations, i.e. fibers aligned in the direction of the loading forces.

To generate the statistical results, the experimental results at different moisture levels were compared in pairs. If the test revealed that a given pair of results are not statistically different from each other, the statistical values for that pair were taken to be the mean of their experimental values. For a statistically different pair, the difference in the statistical values for the pair was assumed to be the same as the difference in their experimental values.

TENSILE TEST: For pine fibers, the curve for the Young's modulus, shown in Figure B.1, exhibits a peak at 30% MC while the value for E is almost independent of the moisture content at lower moisture levels. A similar curve for aspen fibers shows a dip at 20% to 30% MC while the value rises for lower and higher moisture levels.

As shown in Figures B.2 and B.3, the tensile strength and the corresponding extension reach their lowest values at 30% MC for pine and rise with lower or higher MC. The peak and break loads, and the elongation at break also show similar trends. For aspen fibers however, the tensile strength is highest at 30% MC and retains this level as the moisture content rises further. The extension at peak and the elongation at break are also influenced significantly by changes in the moisture level of the aspen fibers.

FLEXURAL TEST: For pine fibers, the modulus of elasticity, shown in Figure B.4, rises sharply with increase of MC up to 20% and decreases thereafter, while for aspen, a dip occurs at 20 to 30% MC.

However, some caution must be exercised in using this property as a basis for interpreting the strength of the material since it is very sensitive to the conditions of the test and the smoothness of the curve. Some of the variables needed to compute the MOE have

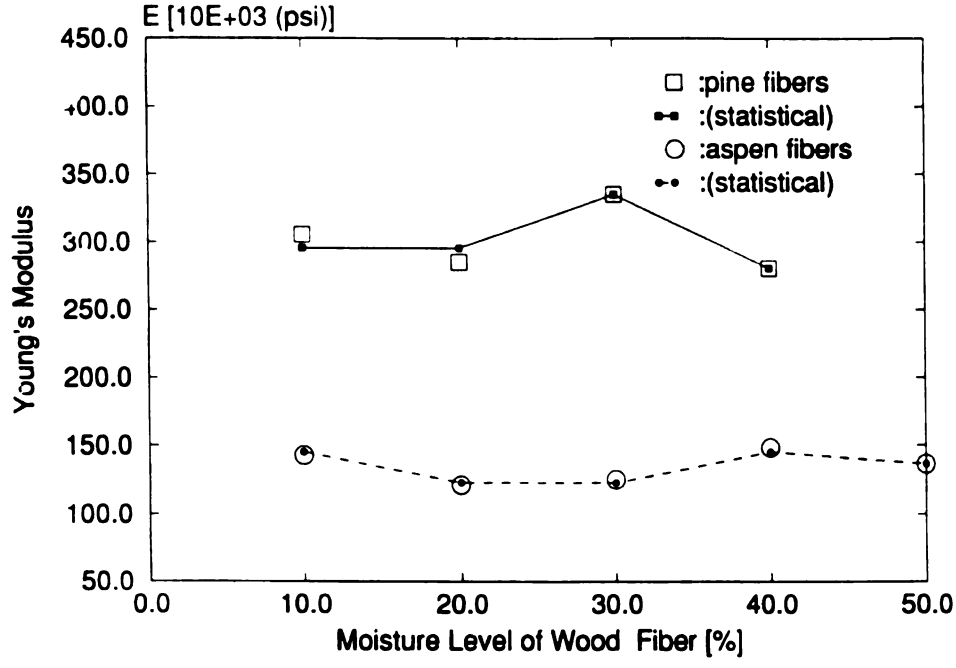

Figure B.1: Plot of the Young's Modulus for the tensile test

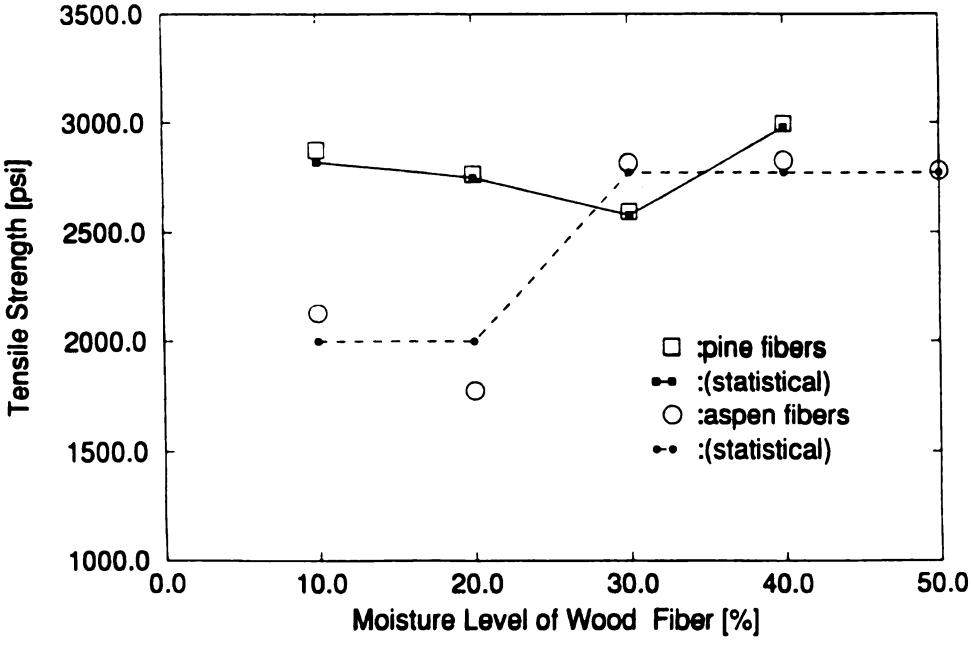

Figure B.2: Variation of the tensile strength with moisture content

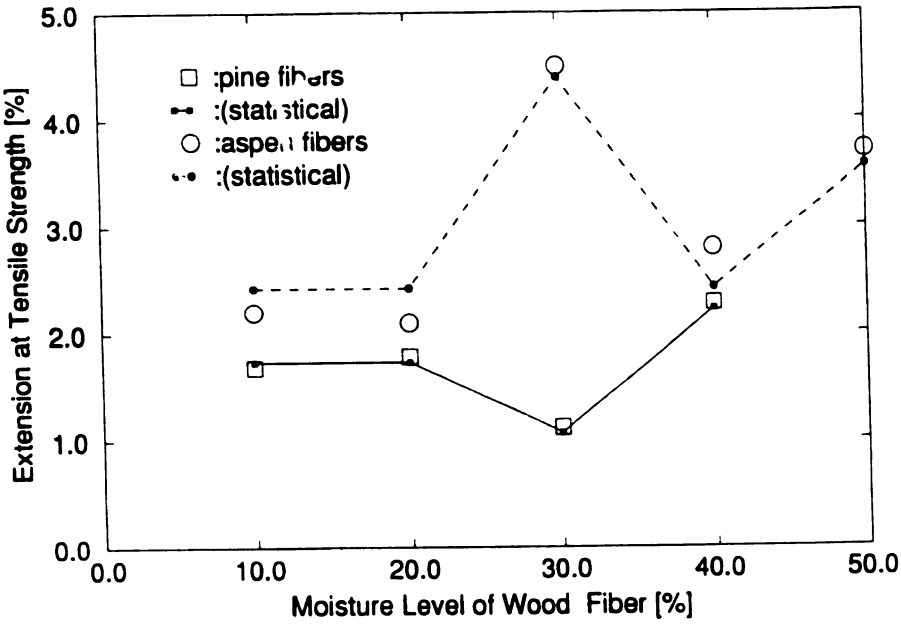

Figure B.3: Extension at the tensile strength

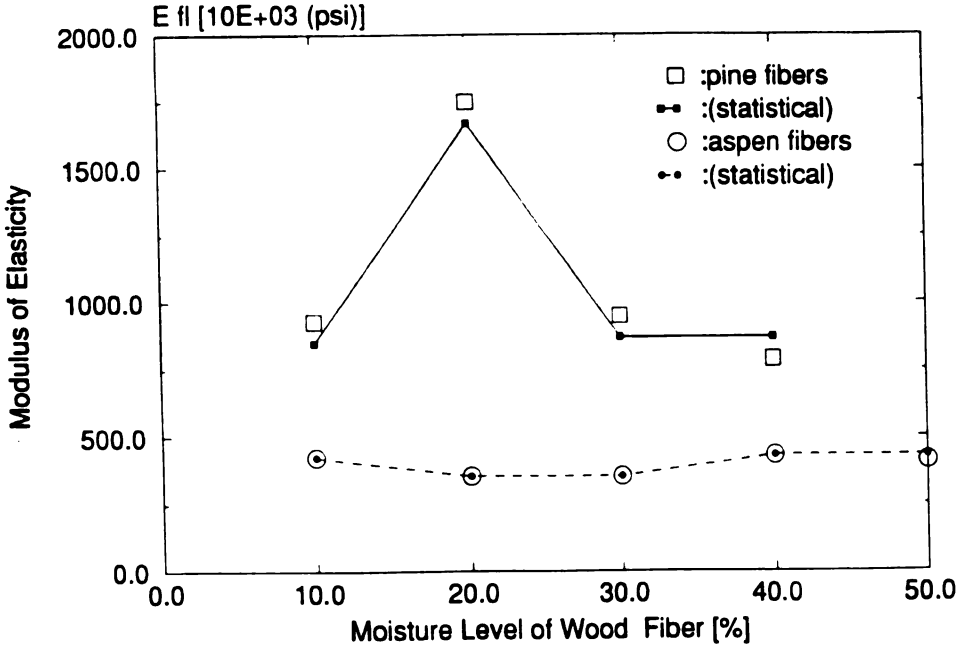

Figure B.4: Modulus of elasticity for flexural test

to be traced from the load-deflection curve and a slight error in these variables can lead to large deviations in the values for MOE. For these reasons, other properties like the break load, flexural strength, yield strength, and the extension at break, which are directly measured, will be used here to interpret the flexural strength of the composite.

The break load, extension at flexural strength, and elongation at break, shown in Figures B.5 and B.6, are affected quite significantly by the moisture level. With pine fibers the break load decreases steadily with rising moisture level reaching a minimum at 30% MC and then increases very markedly. For aspen, the curve shows a minimum at 20% while the values for the break load increases steadily thereafter.

IMPACT TEST: The values for the impact strength of the composites containing pine fibers are significantly higher than the corresponding values for the aspen-based composites. Examining the influence of wood moisture, it can be seen in Figure B.7 that the curve for pine exhibits a dip at 30% MC while the values for lower moisture levels are almost independent of MC. Beyond 30%, the impact strength increases to slightly above the level attained in the low moisture region.

Similar results for aspen show that the impact strength is more sensitive to changes in wood moisture. The maximum value is reached at 20% and a subsequent decrease is observed at higher MC.

B.5 Discussion

The observed differences in the resulting mechanical properties suggest that variation in water content and water loss affects the composite microstructure significantly.

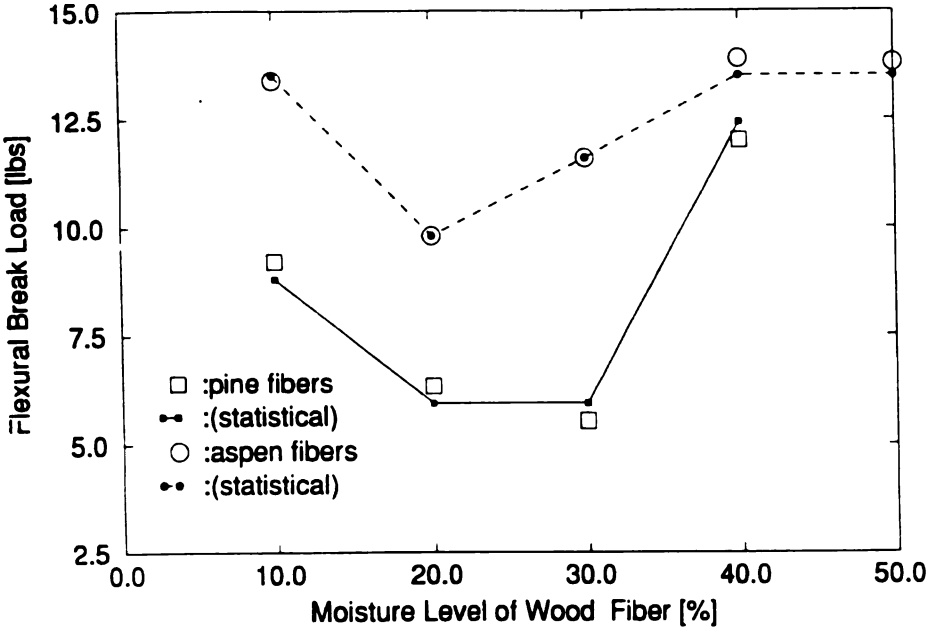

Figure B.5: Break load for the flexural test

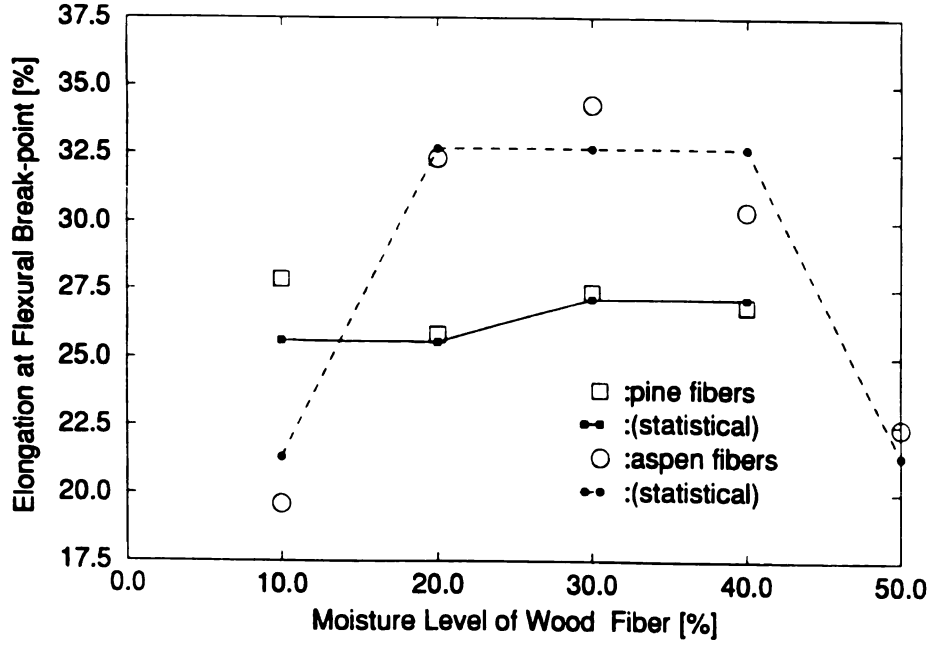

Figure B.6: Elongation at break for the flexural test

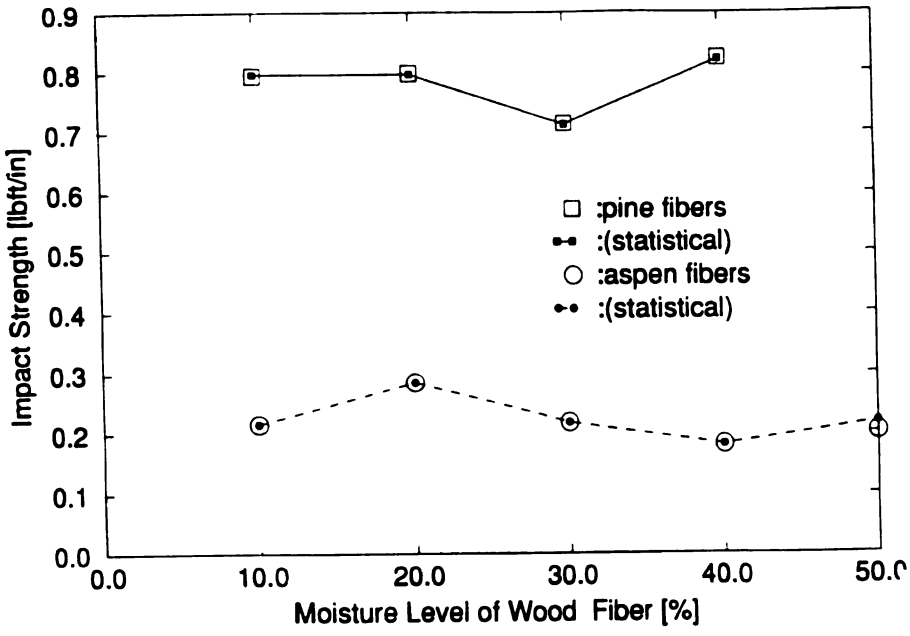

Figure B.7: Impact strength of the wood fiber-HDPE composite

It was reported in an earlier study that TGA (Thermo-Gravimetric Analysis) tests revealed that there is almost no water left in the samples [57]. All specimens tested were said to indicate a final MC of about 1%. This would mean that most of the wood moisture has been driven out during processing.

Shrinking of the fibers as the water is lost is very important to the ensuing mechanical properties of the composite. Perhaps the differences observed in trends between the pine and the aspen composites, especially in the range of MC up to 30%, arise from the significant differences in their shrinkage factors with loss of moisture [7].

Also, the relatively wider variations in mechanical properties observed with aspen fibers could have resulted from the processing technique. In the present experiments with pine fibers, the introduction of the fibers to the HDPE "stream" was done in a more systematic manner, ensuring a more uniform fiber/HDPE ratio in the final composite.

As noted earlier, by keeping the ratio 40% fiber (including moisture) to 60% HDPE, the fiber content (FC) is decreased as MC is increased. However, such changes in the fiber content are not likely to affect the mechanical properties greatly. For instance, increasing MC from 10 to 40% only results in a decrease of FC from 36.4 to 28.6%. In the work of Gogoi [4], no significant changes in most of the mechanical properties occurred with changes in FC between 20 and 40%.

The observation that most of the mechanical properties of pine/HDPE composite are lowest at 30% is somehow expected. A typical value for the fiber saturation point (FSP) for pine is 29% [7]. Most of the mechanical properties of wood are known to increase as the wood moisture content is reduced below the FSP.

In the study reported in reference 55, scanning electron microscopic (SEM) pictures of the composite were taken in attempts to shed some light on its microstructure. It was reported that at 10% MC, the pine fibers are uniformly distributed within the HDPE matrix and are embedded very well within the matrix. That indicates good adhesion between the fibers and the matrix which is very important for strength properties.

In contrast, the distribution of the pine fibers was found not to be uniform at 30% moisture content. Occasional clusters of fibers and HDPE were found at different locations within the composite resulting in relatively wider variations in the measured mechanical properties for samples cut from the same composite slab. The adhesion becomes generally poor and this leads to poor mechanical strength.

For aspen, large voids were seen to surround the undamaged fibers at 20% MC and the void fraction seems to be larger than at other moisture levels. This could explain why some of the mechanical properties are poor at this level.

In the 50% samples, the aspen fibers seem torn and cracked with plenty of space within the fibers. The fiber surface is very rough with different parts projecting in different directions. They seem to be bonded well to the matrix. It is worth noting that the voids at this MC occur more within the fibers, and are not so relevant for strength properties.

B.6 Conclusions

The preceding discussions show that the fiber/matrix adhesion and changes in fiber microstructure at different moisture levels are two critical factors that determine the mechanical properties of the resulting composite. It is therefore reasonable to conclude that processing is a predominant factor in determining the formation of the microstructure with change of MC. Shear and compression forces as well as cutting take place during extrusion. This may lead to fiber distortion and damage.

The level of adhesion between the wood fibers and the thermoplastic will no doubt have significant influence on the thermal behavior of the resulting composites. The presence of excessive voids and imperfections may result in a reduced thermal conductivity, which may be of advantage depending on the objectives for which the composite material is being used. Lack of uniformity in terms of wood fiber distribution within the composite can lead to the presence of localized HDPE clusters as observed at some moisture levels. This will be disadvantageous since, in case of fire, dripping and running may occur from such locations resulting in poor overall fire-safety characteristics.

Obviously, the results of this appendix have shown that it is very important that the subjects of wood moisture influence on the composite mechanical and thermal properties be studied in greater detail. This will enable a better understanding of the fiber/matrix

interaction and, possibly, the factors responsible for some of the differences in trends observed with the two kinds of wood. It is noteworthy to observe that such studies have been conducted to some extent with aspen fibers in [57].

BIBLIOGRAPHY

BIBLIOGRAPHY

[1] Yam, K., Gogoi, B., Lai, C., and Selke, S., "Composites from Compounding Wood Fibers with Recycled High Density Polyethylene," *Polymer Engineering Science*, 30:693-699, 1990.

[2] Selke, S., "Recycled Post-Consumer HDPE: Properties and Use as a Matrix for Wood Fiber Composites," *Design and Manufacturing of Advanced Composites, ASM International*, Metals Park, Ohio, 255-258, 1989.

[3] Youngquist, J. A., "Unlikely Partners? The Marriage of Wood and Nonwood Materials," *Forest Products Journal*, 45(10):25-30, 1995.

[4] Pattanakul, C., Grulke, E., Selke, S., Lai, C., and Miltz, J., "Properties of Recycled High Density Polyethylene Milk Bottles," *Antec 88 Conference Proceedings*, Society of Plastic Engineers, Atlanta, 1802-1804, 1988.

[5] DeRis, J. N., "Spread of a Laminar Diffusion Flame," *Twelfth Symposium (International) on Combustion*, The Combustion Institute, Pittsburgh, 241-252, 1969.

[6] U.S. Department of Agriculture, *Wood Handbook: Wood as an Engineering Material*, Forest Products Laboratory, Forest Service, Washington D.C., 4.41-4.48, 1974.

[7] Haygreen, J. G., and Bowyer J. L., *Forest Products and Wood Science: An Introduction*, Second Edition, Iowa State University Press, Ames, Iowa, 162-172.

[8] Selke, S., Yam, K., and Nieman, K., "Effects of Additives on Mechanical Properties of Wood Fiber/High Density Polyethylene Composites," *Antec 89 Conference Proceedings*, Society of Plastic Engineers, New York, 1813-1815, 1989.

[9] Jenness, R., and Patton, S., *Principles of Dairy Chemistry*, R. E. Krieger Publishing Co., Huntington, New York, 1976.

[10] Haraguchi, K., "The Effect of Surface Sulfonation of High Density Polyethylene (HDPE) on the Mechanical Properties of HDPE/Wood Fiber Composites," *MS Thesis*, Michigan State University, MI, 1993.

[11] Hernandez, C., Selke, S., and Kirloskar, M., "Butyric Acid Retention of Post-Consumer Milk Bottles," *Antec 88 Conference Proceedings*, Society of Plastic Engineers, Atlanta, 1805-1808, 1988.

[12] Wichman, I. S., "Theory of Opposed-Flow Flame Spread," *Progress in Energy and Combustion Science*, 18:553-593, 1992.

[13] Friedman, R. A., "A Survey of Knowledge About Idealized Fire Spread Over Surfaces," *Fire Research Absracts*, 10:1-8, 1968.

[14] Tarifa, C. S., and Torralbo, A. M., "Flame Propagation Along the Interface Between a Gas and a Reacting Medium," *Eleventh Symposium (International) on Combustion*, The Combustion Institute, Pittsburgh, 533-544, 1967.

[15] DeRis, J. N., "The Spread of a Diffusion Flame Over a Combustible Surface," *Ph.D Thesis*, Harvard University, Boston, MA, 1968.

[16] McAlevy, R. F., and Magee, R. S., "The Mechanisms of Flame Spreading Over the Surface of Igniting Condensed-Phase Materials," *Twelfth Symposium (International) on Combustion*, The Combustion Institute, Pittsburgh, 215-227, 1969.

[17] Sirignano, W. A., "A Critical Discussion of Theories of Flame Spread Across Solid and Liquid Fuels," *Combustion Science and Technology*, 6:95-105, 1972.

[18] Sirignano, W. A., "Theory of Flame Spread Above Solids," *Acta Astronaut.* 1:1285-1299, 1974.

[19] Wichman I. S., and William, F. A., "A Simplified Model for Flame Spread in an Opposed Flow Along a Flat Plate of a Semi-Infinite Solid," *Combustion Science and Technology*, 32:91-123, 1983.

[20] Lastrina, F.A., Magee, R. S., and McAlevy III, R.F., "Flame Spread Over Fuel Beds: Solid-Phase Energy Considerations," *Thirteenth Symposium (International) on Combustion*, The Combustion Institute, Pittsburgh, 935-948, 1971.

[21] Magee, R. S., and McAlevy, R. F., "The Mechanism of Flame Spread," *Journal of Flammability*, 2:271-297, 1971.

[22] Ohki, Y., and Tsugé, S., "On Flame Spreading Over a Polymer Surface," *Combustion Science and Technology*, 9:1-12, 1974.

[23] Fernandez-Pello, A. C., and Williams, F. A., "Laminar Flame Spread Over PMMA Surfaces," *Fifteenth Symposium (International) on Combustion*, The Combustion Institute, Pittsburgh, 217-231, 1975.

[24] Fernandez-Pello, A. C., and Williams, F. A., "A Theory of Laminar Flame Spread Over Flat Surfaces of Solid Combustibles," *Combustion and Flame*, 28:251-277, 1977.

[25] Wichman, I, S., Williams, F. A., and Glassman, I., "Theoretical Aspects of Flame Spread in an Opposed Flow over Flat Surfaces of Solid Fuels," *Nineteenth Symposium (International) on Combustion*, The Combustion Institute, Pittsburgh, 835-845, 1983.

[26] Ito, A., and Kashiwagi, T., "Temperature Measurements in PMMA During Downward Flame Spread in Air Using Holographic Interferometry," *Twenty-First Symposium (International) on Combustion*, The Combustion Institute, Pittsburgh, 65-74, 1987.

[27] Feng, C. C., and Sirignano, W. A., "Further Calculations Based Upon a Theory of Flame Spread Across Solid Fuels," *Combustion and Flame*, 29:247-263, 1977.

[28] Wichman, I. S., "Flame Spread in an Opposed Flow With a Linear Velocity Gradient," *Combustion and Flame* 50:287-304, 1983.

[29] Crescitelli, S., Pota, F., Santo, G., and Tufana, V., "Influence of Solid Phase Thermal Properties on Flame Spread Over Polymers," *Combustion Science and Technology* 27:75-78, 1981.

[30] Di Blasi, C., and Wichman, I. S., "Effects of Solid-Phase Properties on Flames Spreading over Composite Materials," *Combustion and Flame*, 102:229-240, 1995.

[31] Oladipo, A. B., Wichman, I. S., and Beck, J. V., "Experimental Investigation of the Thermal Properties of Wood Fiber/Thermoplastic Composites," to appear in *Journal of Composite Materials*, 14, 1998.

[32] Zhang, J., Shields, T. J., and Silcock, G. W., "Effect of Melting Behavior on Upward Flame Spread of Thermoplastics," *Fire and Materials*, 21:1-6, 1997.

[33] Parker, W., "Flame Spread Model for Cellulosic Materials," *Journal of Fire and Flammability*, 3:259-269, 1972.

[34] Di Blasi, C., "Predictions of Wind-Opposed Flame Spread Rates and Energy Feedback Analysis for Charring Solids in a Microgravity Environment," *Twenty-Fifth Symposium (International) on Combustion*, The Combustion Institute, Pittsburgh, 332-340, 1994.

[35] Weber, R. O., and De Mestre, N. J., "Flame Spread Measurements on Sample Ponderosa Pine Needles: Effect of Sample Orientation and Concurrent External Flow," *Combustion Science and Technology*, 70:17-32, 1990.

[36] Ray, S. R., "Flame Spread Over Solid Fuels," *Ph.D Thesis*, Princeton University, Princeton, NJ, 1981.

[37] Wichman, I. S., and Saito, "An Experimental Study of the Effects of Gravity on Flame Spread in High Oxygen Concentration Environments," *Combustion and Flame*, 52:291-297, 1983.

[38] Chen, C., and Yang, M., "Downward Flame Spread as a Function of Angle of Inclination," *Transport Phenomena in Combustion*, 1:668-677, 1995.

[39] Hirano, T, Norcikis, S. E., and Waterman, T. E., "Measured Velocity and Temperature Profiles Near Flames Spreading Over a Thin Combustible Solid," *Combustion and Flame*, 23:83-96, 1974.

[40] Hirano, T, Norcikis, S. E., and Waterman, T. E., "Postulations of Flame Spread Mechanisms," *Combustion and Flame*, 22:353-363, 1974.

[41] Frey, A. E., and T'ien, J. S., "A Theory of Flame Spread Over a Solid Fuel Indicating Finite-Rate Chemical Kinetics," *Combustion and Flame*, 36:263-289, 1979.

[42] Wichman, I. S., "A Model Describing the Influences of Finite-Rate Gas-Phase Chemistry on Rates of Flame Spread Over Solid Combustibles," *Combustion Science and Technology*, 40:233-255, 1984.

[43] Fernandez-Pello, A. C., Ray, S. R., and Glassman, I., "Flame Spread in an Opposed Flow: The Effect of Ambient Oxygen Concentration," *Eighteenth Symposium (International) on Combustion*, The Combustion Institute, Pittsburgh, 579-587, 1981.

[44] Rizvi, A. R., "An Experimental Study of the Effects of Buoyancy on the Flame Spread Rate Over Thermally Thick Fuels," *M.S. Thesis*, University of Kentucky, Lexington, KY, 1980.

[45] Rybanin, S., "The Dependence of the Flame Spread Rate Over Solid Fuel on Damköhler Number and Heat Loss," *Twenty-Sixth Symposium (International) on Combustion*, The Combustion Institute Pittsburgh, 1487-1493, 1996.

[46] Christensen, R. M., *Mechanics of Composite Materials*, John Wiley & Sons, New York, 316-319, 1991.

[47] Ziebland, H., "The Thermal and Electrical Transmission Properties of Polymer Composites," in *Polymer Engineering Composites*, Applied Science Publishers Ltd., London, 1974.

[48] Dowding, K. J., Beck, J. V. and Eilens, L., "Method for Measuring the Orthotropic Thermal Conductivity and Volumetric Heat Capacity in a Carbon-Carbon Composite," in *Thermal Conductivity*, 23:107-118 (K. E. Wilkes, R. B. Dinwiddle, R. S. Graves eds.) Technometric, Lancaster, PA, 1996.

[49] Scott, E. P. and Beck, J. V., "Estimation of Thermal Properties in Carbon/Epoxy Composite Materials During Curing," *Journal of Composite Materials*, 26(1):20-36, 1992.

[50] Beck, J. V. and Dhanak, A. M., "Simultaneous Determinations of Thermal Conductivity and Specific Heat," *ASME-AIChE Heat Transfer Conference and Exhibit*, Los Angeles, CA, 1965.

[51] Beck, J. V. and Osman, A. M., "Sequential Estimation of Temperature -Dependent Thermal Properties," *High Temperature-High Pressures*, 23:255-266, 1981.

[52] Beck, J. V. and Arnold, K. J., *Parameter Estimation in Engineering and Science*, Wiley, 1987.

[53] Beck, J. V., Blackwell, B. and St. Clair, C. R., *Inverse Heat Conduction: Ill-Posed Problems*, Wiley-Interscience, 1985.

[54] Perepechko, I. I., *An Introduction to Polymer Physics*, English Translation, Mir Publishers, Moscow, 1981.

[55] Wichman, I. S., Oladipo, A. B., Hermann, I, and Selke, S., "The Influence of Moisture on Fiber/Matrix Adhesion for Wood/HDPE Composites," *Proceedings of the 9th Annual ASM/ESD Advanced Composites Conference*, Published by ESD, The Engineering Society, Ann Arbor, Michigan, 265-276, 1993.

[56] Wichman, I. S. and Hermann, I., "The Influence of Moisture on Fiber/Matrix Adhesion of Aspen/HDPE-Composites: Mechanical Properties," Mineral and Organic Fillers in Polymers, *International Symposium, Proceedings MOFFIS 93*, Namur - Belgique, 123-130, 1993.

[57] Hermann, I., "The Influence of Moisture on Fiber/Matrix Adhesion of aspen/HDPE-Composites: Mechanical Properties," *Studienarbeit (MS Thesis)*, Michigan State University, USA/RWTH, Germany, 1992.

[58] Santrock, J., Personal Communication, GM Research Center, 1997.

[59] Wichman, I. S. and Osman, M. O., "Flame Spread Over a Flat Combustible Thermally Thick Solid in an Opposed Oxidizer Shear Flow," *Combustion and Flame* 112:623-634, 1998

[60] West, J. and Bhattacharjee, S., "Investigation of Controlling Parameters in Transition Between Thermally Thin and Thermally Thick Flame Spread Over Solid Fuels in an Opposing Flow," Fall Technical Meeting, The Combustion Institute, Western States Section, Berkeley, CA, 1992.

[61] Wichman, I. S., "Studies of Flame Spread in an Opposed Flow Over Surface of Solid Fuels," *Ph.D Dissertation*, Princeton University, Princeton, NJ, 1983.

[62] Oladipo, A. B., and Wichman, I. S., "Experimental Study of Opposed Flow Flame Spread Over Wood Fiber/Thermoplastic Composite Materials," submitted for publication in *Combustion and Flame*, 1998.

[63] Saito, K., Williams, F. A., Wichman, I. S., and Quintiere, J. G., *Journal of Heat Transfer*, 111: 438-445, 1989.

[64] Wichman, I. S., and Atreya, A., "A Simplified Model for the Pyrolysis of Charring Materials," *Combustion and Flame*, 68:231-247, 1987.

[65] Villermaux, J., Antoine, B., Lede, J., and Soulignac, F., "A New Model for Thermal Volatilization of Solid Particles Undergoing Fast Pyrolysis," *Chemical_Engineering Science*, 41(1):151-157, 1986.

[66] Fredlund, B., "Modelling of Heat and Mass Transfer in Wood Structures During Fire," *Fire and Safety Journal*, 20:39-70, 1993.

[67] Kashiwagi, T., and Nambu, H., "Global Kinetic Constants for Thermal Oxidative Degradation of a Cellulosic Paper," *Combustion and Flame*, 88:345-368, 1992.

[68] Shafizadeh, F., and Chin, P. P. S., *ACS Symposium Series* 43:57, 1977.

[69] Shafizadeh, F., "The Chemistry of Pyrolysis and Combustion," in *The Chemistry of Solid Wood*, R. Rowell (ed.), ACS, Washington, D. C., 1984.

[70] Broido, A., and Nelson, M.A., "Char Yield on Pyrolysis of Cellulose," *Combustion and Flame*, 24:263-268, 1975.

[71] DiBlasi, C., "Modeling and Simulation of Combustion Processes of Charring and Non-Charring Solid Fuels," *Progress in Energy and Combustion Science*, 19:71-104, 1993.

[72] Lipska, A. E., and Parker, W. J., "Kinetics of the Pyrolysis of Cellulose in the Temperature Range 250-300°C," *Journal of Applied Polymer Science*, 10:1439-1453, 1966.

[73] Wichman, I. S., and Melaaen, M., "Modeling the Pyrolysis of Cellulosic Materials," in *Advances in Thermochemical Biomass Conversion*, T. Bridgewater (ed.), Chapman and Hall, London, 1993.

[74] Diblasi, C., "Analysis of Convection and Secondary Reaction Effects within Porous Solid Fuels Undergoing Pyrolysis," *Combustion Science and Technology* 90:315-340, 1993.

[75] Wichman, I. S. and Oladipo, A. B., "Examination of Three Pyrolytic Reaction Schemes for Cellulosic Materials," *Fire Safety Science - Proceedings of the Fourth International Symposium*, ed. Takashi Kashiwagi, International Association for Fire Safety Science, 313-323, 1995.

[76] Lewellen, P. C., Peters, W. A., and Howard, J. B., "Cellulose Pyrolysis Kinetics and Char Formation Mechanism," Sixteenth Symposium (International) on Combustion, The Combustion Institute, Pittsburgh, 1471-1480, 1976.